

UCLA

UCLA Electronic Theses and Dissertations

Title

Clumped Isotopes as Tracers from Enzymes to Global Biogeochemical Cycles

Permalink

<https://escholarship.org/uc/item/4g0431p1>

Author

Ash, Jeanine L.

Publication Date

2017

Peer reviewed|Thesis/dissertation

UNIVERSITY OF CALIFORNIA

Los Angeles

Clumped Isotopes as Tracers from Enzymes
to Global Biogeochemical Cycles

A dissertation submitted in partial satisfaction of the
requirements for the degree Doctor of Philosophy
in Geochemistry

by

Jeanine L. Ash

2017

© Copyright by

Jeanine L. Ash

2017

ABSTRACT OF THE DISSERTATION

Clumped Isotopes as Tracers from Enzymes to Global Biogeochemical Cycles

by

Jeanine L. Ash

Doctor in Philosophy in Geochemistry

University of California, Los Angeles, 2017

Professor Edward D. Young, Chair

Reactions occurring at enzymes drive all of Earth's biogeochemical cycles from the oxygen in the atmosphere to methane below the seafloor. Although these gases are critical for life on our planet, they have a multitude of sources and sinks that can be difficult to distinguish from one another, complicating our ability to understand their budgets both in the present and the past. Here, I explore new tracers of the oxygen and methane cycles with a focus on the biologic production and consumption of these gases: photosynthesis/respiration and methanogenesis/methanotrophy, respectively. Isotopes have been used as tracers of these processes since the inception of the field of stable isotope geochemistry, but only the measurement of singly-substituted molecules (i.e., $^{18}\text{O}^{16}\text{O}$ and $^{13}\text{CH}_4$) has been possible. Within, I report measurements of the relative abundances of $^{18}\text{O}^{18}\text{O}$ and $^{18}\text{O}^{17}\text{O}$ for oxygen that has been biologically cycled in a terrarium experiment and respired in lake water as well as $^{13}\text{CH}_3\text{D}$ and $^{12}\text{CH}_2\text{D}_2$ of biologically produced and consumed seafloor methane. These multiply-

substituted isotopologues provide a new dimension of information by illuminating the enzyme level chemistry in making and breaking bonds. I find that photosynthesis and methanogenesis produce oxygen and methane respectively that is out of equilibrium with environmental temperatures and the resulting gases have fewer multiply-substituted isotopologues than predicted by chance alone. Respiration of oxygen leaves behind a residue enriched in these rare isotopologues; this unexpected result merits further exploration. However, anaerobic methanotrophy seems to be capable of reordering isotopes by enzymatic back reaction, driving a pool of methane to intra-species equilibrium at low temperature. These findings have consequences both for ongoing work in measuring marine primary productivity as well as exploring the extent of life in the deep biosphere and throughout the solar system.

The dissertation of Jeanine Louise Ash is approved.

Kevin D. McKeegan

Maria Prokopenko

Edwin Arthur Schauble

Tina Irene Treude

Edward Donald Young, Committee Chair

University of California, Los Angeles

2017

For my mother, Kathleen Mary Ash

Table of Contents

Abstract of the Dissertation.....	<i>ii</i>
Committee Page.....	<i>iv</i>
Dedication.....	<i>v</i>
Table of Contents.....	<i>vi</i>
List of Figures.....	<i>vii</i>
List of Tables.....	<i>ix</i>
Acknowledgements.....	<i>x</i>
Vita.....	<i>xiii</i>
Chapter 1: Introduction.....	1
Chapter 2: Clumped isotope measurements of respired O ₂ in Lake Houston.....	5
Chapter 3: Biological signatures in clumped isotopes of O ₂	38
Chapter 4: Exchange catalysis during anaerobic methanotrophy revealed by ¹² CH ₂ D ₂ and ¹³ CH ₃ D in methane gas.....	76
Appendix 1: Measurements of ¹² CH ₂ D ₂ and ¹³ CH ₃ D from Landsort Deep, Baltic Sea.....	107

List of Figures

2.1.....	8
2.2.....	17
2.3.....	19
2.4.....	20
2.5.....	20
2.6.....	23
2.7.....	25
2.8.....	27
2.9.....	28
2.10.....	28
2.11.....	30
3.1.....	40
3.2.....	42
S3.1.....	50
S3.2.....	56
S3.3.....	59
S3.4.....	64
S3.5.....	65
4.1.....	80
4.2.....	85
4.3.....	87
S4.1.....	95

S4.2.....	96
S4.3.....	99
S4.4.....	100
A1.....	107

List of Tables

2.1.....	16
2.2.....	27
2.3.....	27
2.4.....	31
S3.1.....	68
S3.2.....	69
S3.3.....	70
S4.1.....	99
S4.2.....	101
S4.3.....	101
A1.....	108

Acknowledgements

Thank you to my advisor Ed Young. You probably never imagined that a plant and microbe-loving person like me would start growing muddy things in your spotlessly clean lab, but I hope you enjoyed it. I showed up in your office with no idea what kind of scientist I would be, but you helped me forge a path that I am immensely proud of. Thank you for being rigorous but kind and always having time to listen to new ideas. I will always remember your group as being an amazing place where people work on things ranging from Photosystem II to meteorites, and I am better for it. I'm going to clean out that terrarium tomorrow.

Thank you to my committee members Kevin McKeegan, Maria Prokopenko, Edwin Schauble and Tina Treude. I cannot imagine doing this without your feedback and support. Thank you to Jean-Luc Margot, Rick Fort, Jim Nakatsuka and Lauri Holbrook who eased all things administrative. Thank you especially to Shauna McManus, Amelia Shevenell, Ellen Martin and Peggy Delaney who listened and helped.

Thank you to my co-scientists during the Integrated Ocean Drilling Program's Expedition 347 to the Baltic Sea. Dalton Hardisty, you were a great container-mate and Sophie Green, thank you for being a fantastic friend who was also an excellent safety officer during the Lake Houston Expedition.

Issaku Kohl, you were a constant friend and mentor during this process. We worked in the lab, we talked about science and life, we walked our dogs and then we did it all over again the next day. Thank you so much for always being there.

I sincerely thank the Department of Earth, Environmental and Planetary Sciences at Rice University for a home away from home. In the same vein, I think Benjamin Passey and Naomi Levin for their hospitality and mentorship.

Thank you to my friends Chris Culbertson, Melissa McMillan, Sarah Treube and Deborah Saunders. I could not have done this without you.

This work would not have been possible without the love and support provided by my family. Thank you to my mother, Kathy Ash, for showing me the natural world around me and in books, driving me to countless science fairs and music camps, and giving me everything I needed to be who I am today. I am inspired by late father, Donald Ash, whose geology PhD thesis sat ignored on my bookshelf for many years until it suddenly became rather relevant to my life path. Thank you endlessly to my sister, brother-in-law and niece, Danielle, Lewie and Ella Zimmerman. You kept me grounded, you kept me going, you fed me a lot of delicious meals, and you helped me laugh through it all. And thank you especially Cosmo Ash, the world's greatest dog, who helped me finish associate, bachelor, master and candidacy degrees. You were the most educated dog I have ever known, and the one who loved me the best.

Finally, thank you to Laurence Yeung, my partner in the laboratory and in life. You taught me everything I know about vacuum lines and gas-source mass spectrometry, but most importantly, coffee. You believed in me especially when I did not, and for this I will always be grateful.

I was supported by a National Science Foundation Graduate Fellowship from 2013-2017.

Chapter 2 is in preparation for publication with co-authors Edward D. Young and Laurence Y. Yeung. E.D. Young contributed to the discussion of this paper, L.Y. Yeung contributed to the experimental design and is the Principle Investigator. I designed the experiment, collected the samples, measured them, analyzed the data and wrote the paper.

A version of Chapter 3 was previously published as “Yeung, L.Y.,* & Ash, J.L.,* and Young, E.D. ‘Biological signatures in clumped isotopes of O₂,’ *Science*, 348 (6233) 431-434 *denotes equal contributions.” L.Y. Yeung contributed to the experimental design, measurements, data analysis and co-wrote the paper. E.D. Young contributed to the discussion and was the Principle Investigator. I designed the experiment, measured the samples, analyzed the data, and co-wrote the paper.

Chapter 4 is in preparation for publication with co-authors Matthias Egger, Issaku Kohl, Caroline Slomp, Barbara Sherwood Lollar, Tina Treude, R. John Parkes, Barry Cragg and Edward D. Young. R.J. Parkes and B. Cragg contributed the microbial activity measurement data. I. Kohl assisted in sample measurement. All authors contributed to the discussion, and E.D. Young is the Principle Investigator. I designed the study, collected the samples, measured them, analyzed the data and wrote the paper. This work was supported by a Deep Carbon Observatory Deep Energy grant to Tina Treude submitted on behalf of Jeanine Ash.

JEANINE L. ASH

Education

C.Ph., Geochemistry, UCLA	March 2017
M.S., Geochemistry, UCLA	April 2015
B.S., Earth Systems Geosciences, University of Arizona	August 2011
AA., Liberal Arts, Hillsborough Community College	August 2008

Positions held

NSF Graduate Research Fellow, UCLA	2013-2015
Intern, Shell International Exploration & Production	2015
Inorganic Geochemist (off/onshore), IODP Exp. 347	2013/2014
Lecturer, UCLA	2012-2014
Graduate Research and Teaching Assistant, UCLA	2011-2017
NSF Research Experience for Undergraduates Fellow, University of Akron	2009
Undergraduate Research Assistant, University of Arizona	2008-2011

Publications

1. Kotthoff, U., Groeneveld, J., Ash, J.L., Fanget, A-S., Quintana Krupinski, N., Peyron, O., Stepanova, A., Warnock, J., Van Helmond, N.A.G.M., Passey, B.H., Clausen, O.R., Bennike, O., Andr n, E., Granoszewski, W., Andr n, T., Filipsson, H.L., Seidenkrantz, M-S., Slomp C.P., and Bauersachs, T. "Reconstructing Holocene temperature and salinity variations in the western Baltic Sea region: A multi-proxy comparison from the Little Belt (IODP Expedition 347, Site M0059)," *Biogeosciences*, accepted for publication, 2017. Discussions paper URL: <https://doi.org/10.5194/bg-2017-101>.
2. Young, E.D., Kohl, I.E., Sherwood Lollar, B., Etiope, G., Rumble III, D., Li, S., Haghnegahdar, M.A., Schauble, E.A., McCain, K.A., Foustoukos, D.I., Sutcliffe, C., Warr, O., Ballentine, C.J., Onstott, T.C., Hosgormez, H., Neubeck, A., Marques, J.M., P rez-Rodr guez, I., Rowe, A.R., LaRowe, D.E., Magnabosco, C., Yeung, L.Y., Ash, J.L., and Bryndzia, L.T. "The relative abundances of resolved $^{12}\text{CH}_2\text{D}_2$ and $^{13}\text{CH}_3\text{D}$ and mechanisms controlling isotopic bond ordering in abiotic and biotic methane gases." *Geochimica et Cosmochimica Acta*, 203, 235-264. 2017.
3. Yeung, L.Y., Murray, L.T., Ash, J.L., Young, E.D., Boering, K.A., Atlas, E.L., Schauffler, S.M., Lueb, R.A., Langenfelds, R.L., Krummel, P.B., Steele, L.P., and Eastham, S.D. "Isotopic ordering in atmospheric O_2 as a tracer of ozone photochemistry and the tropical atmosphere." *Journal of Geophysical Research-Atmospheres*, 127. 2016.
4. Yeung, L.Y.,* & Ash, J.L.,* and Young, E.D. "Biological signatures in clumped isotopes of O_2 ," *Science*, 348 (6233), 431-434. 2015. *denotes equal contributions

5. Yeung, L.Y., Ash, J.L., and Young, E.D. "Rapid photochemical equilibration of isotopic bond ordering in O₂," *Journal of Geophysical Research: Atmospheres*, 119 (17), 10552-10566. 2014.
6. Pelletier, J.D., McGuire, L.A., Ash, J.L., Engelder, T.M., Hill, L.E., Leroy, K.W., Orem, C.A., Rosenthal, S.W., Trees, M.A., Rasmussen, C., and Chorover, J. "Calibration and testing of upland hillslope evolution models in a dated landscape: Banco Bonito, New Mexico," *Journal of Geophysical Research: Earth Surface*, 116. 2011.

Grants and Awards

Harold and Mayla Sullwold Scholarship "in recognition of academic performance and outstanding original research by a PhD Candidate" by UCLA Department of Earth, Space, and Planetary Sciences, 2017, 2016.

"Clumped isotope measurements of biogenic methane from the Baltic Sea on the high-resolution Panorama mass spectrometer," PI: Tina Truede on behalf of J.L. Ash, Deep Carbon Observatory Deep Energy Committee, 2016.

"Carbonate clumped-isotope and triple oxygen isotope analysis of Baltic Sea foraminifera to constrain Quaternary temperatures and hydrology," PI: Ed Young on behalf of J.L. Ash, U.S. Science Support Post-Expedition Awards, 2014.

Teaching Assistant Excellence Award by UCLA Department of Earth, Space, and Planetary Sciences, 2013.

"Trace metal and clumped isotope geochemistry as paleo-environmental indicators in Lake Tanganyika, Africa," PI: J.L. Ash, Geological Society of America Graduate Student Research Grant, 2012.

Select Presentations

Ash, J.L., Egger, M., Kohl, I.E., Treude, T., Slomp, C.P., Cragg, B., Parkes, R.J., Rumble, D., and Young, E.D. " $\Delta^{13}\text{CH}_3\text{D}$ and $\Delta^{12}\text{CH}_2\text{D}_2$ signals of methanogenesis and methanotrophy." *Goldschmidt Geochemistry Conference*, Paris, France, 2017. Oral presentation.

Ash, J.L., Egger, M., Kohl, I.E., Treude, T., Slomp, C.P., Cragg, B., Parkes, R.J., Rumble, D., and Young, E.D. "Tracing deep biosphere methane cycling with fully resolved $^{13}\text{CH}_3\text{D}$ and $^{12}\text{CH}_2\text{D}_2$." *Deep Carbon Observatory International Science Meeting*, St. Andrews, Scotland, 2017. Invited oral presentation.

Ash, J.L., Yeung, L.Y., and Young, E.D. "Biological Influences on Isotopic Ordering in O₂," *Goldschmidt Geochemistry Conference*, Sacramento, CA, 2014. Oral presentation.

Chapter 1: Introduction

“...the equation for $^{18}\text{O}_2$ is not of interest in part because ^{18}O atoms are rare and a very small fraction end up bonded to another...” (Bender and Grande, 1987)

“There appear to be no data on natural backgrounds of CH_2D_2 , CH_3D or CD_4 . Although their concentrations should be very small, their information content would be very high.” (Cicerone and Oremland, 1988)

Molecular oxygen (O_2) and methane (CH_4) are fundamentally significant to Earth’s habitability and the evolution of life. Concentrations of these gases in the atmosphere are the result of constant interplay between the biological and geological processes that create and consume them. Within this dissertation, new isotopic tracers are queried for their utility in probing the creation and destruction of O_2 and CH_4 at the enzymatic level and how these enzyme-level processes influence global biogeochemical cycling is explored.

Recent advances in mass spectrometry now allow for the precise measurement of multiply-substituted isotopologues of gases such as O_2 and CH_4 (Eiler et al., 2013; Ono et al., 2014; Young et al., 2016). These measurements are commonly referred to as “clumped” isotope approaches because rare heavy isotopes are clumped together in the molecules of interest. A defining characteristic of these approaches is that abundances of these rare isotopologues are theoretically independent of the isotopic composition of substrate materials in reactions that

create them (Schauble et al., 2006; Wang et al., 2004). Relative abundances of singly-substituted rare isotopologues however, are often the result of both the reaction temperature and “reservoir effects.” Therefore, clumped isotopes are potentially excellent tracers of bond creating processes (i.e. photosynthesis and methanogenesis) and bond-scission processes (i.e. respiration and methanotrophy) without necessitating prior knowledge of the reservoir.

Chapter 2 introduces biological and photochemical oxygen and its isotopes. First, a review of the stable isotopic composition of atmospheric oxygen and how biological and photochemical cycles influence these signals is given. Clumped isotopes of oxygen are introduced and photochemical experiments that alter bond ordering are described (Yeung et al., 2014). The initial results of dark respiration oxygen consumption experiments in water collected from Lake Houston are used to derive effective β fractionation factors for both the singly- and doubly-substituted molecular oxygen species. These measured fractionation factors are compared to calculated ones that highlight either fractionation due to diffusion or bond-breaking processes. The results indicate that bond-breaking processes likely contribute more to effective β fractionation factor signals than does diffusion into the cell, and this pilot study is the first of its kind to provide these measurements of the doubly-substituted isotopologues for comparison.

Chapter 3 describes the results of a year-long terrarium experiment where five isotopologues of O_2 were monitored to determine the influence of photosynthesis and respiration on the clumped isotope composition of headspace O_2 (Yeung et al., 2015). During diurnal light-dark cycles, the oxygen isotopes of the headspace evolved toward their biological steady state endmember composition. Two approximately week-long terrarium blackouts monitored the evolution of the

headspace during dark respiration cycles. We use these results to predict that the Photosystem II enzyme assembles molecular oxygen with clumped-isotope compositions less than 0‰, and that respiration will leave behind an oxygen reservoir enriched in double-substituted isotopologues relative to its starting composition. The significance of these findings is that biological oxygen processes have unique clumped-isotope signatures not related to formation temperatures.

In **Chapter 5**, the clumped-isotope composition of sedimentary methane samples from the Bornholm Basin, Baltic Sea is presented. We find that zones of methanogenesis correlate with relative abundances of $^{13}\text{CH}_3\text{D}$ and $^{12}\text{CH}_2\text{D}_2$ that are not in isotopic equilibrium with their environmental temperatures, consistent with methane produced from axenic lab cultures (Young et al., 2017). Conversely, anaerobic methane oxidation (AOM) seems to drive methane towards isotopic equilibrium. We use these data to suggest that exchange catalysis on methyl coenzyme M reductase (MCR) and enzymatic back reaction during the first steps of AOM provides a mechanism for equilibrating isotopologues of methane. We suggest that measuring the relative abundances of multiply-substituted isotopologues could shed new light on understanding the deep biosphere methane cycle and offer a potential new methane biosignature where there is a dearth of carbon and hydrogen reservoir information. Within **Appendix 1** is an additional record of deep biosphere methane isotopologue variations from Landsort Deep, Baltic Sea.

References

- Bender, M.L. and Grande, K.D. (1987) Production, respiration, and the isotope geochemistry of O₂ in the upper water column. *Global Biogeochemical Cycles* 1, 49-59.
- Cicerone, R.J. and Oremland, R.S. (1988) Biogeochemical Aspects of Atmospheric Methane. *Global Biogeochemical Cycles* 2, 299-327.
- Eiler, J.M., Clog, M., Magyar, P., Piasecki, A., Sessions, A., Stolper, D., Deerberg, M., Schlueter, H.-J. and Schwieters, J. (2013) A high-resolution gas-source isotope ratio mass spectrometer. *International Journal of Mass Spectrometry* 335, 45-56.
- Ono, S., Wang, D.T., Gruen, D.S., Sherwood-Lollar, B., Zahniser, M.S., McManus, B.J. and Nelson, D.D. (2014) Measurement of doubly substituted methane isotopologue, ¹³CH₃D, by tunable infrared laser direct absorption spectroscopy. *Anal Chem* 86, 6487-6494.
- Schauble, E.A., Ghosh, P. and Eiler, J.M. (2006) Preferential formation of ¹³C-¹⁸O bonds in carbonate minerals, estimated using first-principles lattice dynamics *Geochim Cosmochim Acta* 70, 2510-2529.
- Wang, Z., Schauble, E.A. and Eiler, J.M. (2004) Equilibrium thermodynamics of multiply substituted isotopologues of molecular gases. *Geochim Cosmochim Acta* 68, 4779-4797.
- Yeung, L.Y., Ash, J.L. and Young, E.D. (2014) Rapid photochemical equilibration of isotope bond ordering in O₂. *Journal of Geophysical Research* 119, 10552-10566.
- Yeung, L.Y., Ash, J.L. and Young, E.D. (2015) Biological signatures in clumped isotopes of O₂. *Science* 348, 431-434.
- Young, E., Kohl, I., Lollar, B.S., Etiope, G., Rumble, D., Li, S., Haghnegahdar, M., Schauble, E., McCain, K., Foustoukos, D., Sutcliffe, C.N., Warr, O., Ballentine, C., Onstott, T., Hosgormez, H., Neubeck, A., Marques, J., Pérez-Rodríguez, I., Rowe, A., LaRowe, D., Magnabosco, C., Yeung, L., Ash, J. and Bryndzia, L. (2017) The relative abundances of resolved ¹²CH₂D₂ and ¹³CH₃D and mechanisms controlling isotopic bond ordering in abiotic and biotic methane gases. *Geochim Cosmochim Acta*.
- Young, E.D., Rumble, D., Freedman, P. and Mills, M. (2016) A large-radius high-mass-resolution multiple-collector isotope ratio mass spectrometer for analysis of rare isotopologues of O₂, N₂, CH₄ and other gases. *International Journal of Mass Spectrometry* 401, 1-10.

Chapter 2: Clumped isotope measurements of respired O₂ in Lake Houston

Concentrations of oxygen in Earth's atmosphere and ratios of its three naturally occurring isotopes (¹⁶O, ¹⁷O and ¹⁸O) are the result of a constant balance of short-term biological and photochemical cycles as well as long-term weathering cycles. In this chapter, a review of the biological and photochemical cycling of oxygen is presented followed by preliminary results from two replicate respiration experiments with water collected from Lake Houston (Houston, TX; USA). The purpose of these experiments was to derive effective β_{resp} (where β is the factor that describes how two isotope species fractionate and subscript *resp* is respiration) for the multiply-substituted isotopologues of O₂ (¹⁸O¹⁸O and ¹⁷O¹⁸O). Stable and clumped isotope and O₂/Ar ratios are reported along with β_{resp} values and the contribution of diffusion vs. respiration in these signals is discussed. These data serve as a pilot study for future work to isolate specific respiration mechanisms such as the cytochrome oxidase (COX) and alternative oxidase (AOX) pathways in addition to the photosynthesis pathway.

The $\delta^{18}\text{O}$ composition of atmospheric oxygen

Photosynthetic O₂ inherits water-bound oxygen

Ratios of oxygen isotopes are measured relative to a standard such as VSMOW (Vienna Standard Mean Ocean Water) and reported as differences in per mil (‰) so that

$$\delta^i = 10^3 \left(\frac{{}^iR_{\text{sample}}}{{}^iR_{\text{standard}}} - 1 \right) \quad (2.1)$$

for rare isotope i where for instance

$$\frac{{}^i R_{\text{sample}}}{{}^i R_{\text{standard}}} = \frac{\left(\frac{{}^i \text{O}}{16\text{O}}\right)_{\text{sample}}}{\left(\frac{{}^i \text{O}}{16\text{O}}\right)_{\text{standard}}} = \alpha_i, \quad (2.2)$$

and α is referred to as the fractionation factor.

The first measurements of the isotopic composition of atmospheric oxygen over 80 years ago demonstrated that atmospheric oxygen was isotopically heavier than water-bound oxygen by about 20‰ (Dole, 1935). This difference became known as the “Dole Effect” and it is discussed in the following section. The net reaction for photosynthesis, $6\text{CO}_2 + 6\text{H}_2\text{O} \rightarrow \text{C}_6\text{H}_{12}\text{O}_6 + 6\text{O}_2$, implies that photosynthetic oxygen could inherit its stable isotopic composition from carbon dioxide, water, or some combination of both. These reactants will be referred to hereafter as “substrates,” the molecules involved in enzymatic reactions.

To address this question, photosynthetic oxygen was evolved from ^{18}O labeled H_2O and CO_2 , and the results indicated water as the substrate for O_2 (Dole and Jenks, 1944; Ruben et al., 1941). Most other workers agreed with these initial findings (Kamen and Barker, 1945; Stevens et al., 1975; Vinogradov et al., 1960). However, some questioned the precision of these early oxygen isotope measurements due to slight discrepancies in these results and hypothesized that CO_2 might play some role as a substrate (Metzner, 1975; Metzner et al., 1979). Careful modern experiments have confirmed water as the substrate and suggest that there is no isotope fractionation from water to O_2 in higher plants (Guy et al., 1993; Helman et al., 2005; Luz and Barkan, 2005) while similar experiments for marine photosynthesizers such as cyanobacteria,

green algae and diatoms have found photosynthetic O₂ to be enriched in δ¹⁸O by ~0.5 to 6‰ (Eisenstadt et al., 2010; Helman et al., 2005). However, this enrichment seems to be the result of an O₂ consumption process concurrent with photosynthesis in these organisms, not as the result of an intrinsic fractionation process between water and O₂ (Eisenstadt et al., 2010).

Respiration and the Dole Effect

The offset between the isotopic composition of atmospheric and water oxygen known as the Dole Effect has been the subject of extensive research since its discovery. Early work focused on exchange reactions between CO₂ and O₂ in the stratosphere (Roake and Dole, 1950) and the chemisorption of O₂ by metals (Dole and Lane, 1954). H.A. Barker is credited with first hypothesizing that the oxygen isotopic composition of the atmosphere might be influenced by the preferential bacterial oxidation of the lighter isotopes of oxygen, but the first experiments to test this hypothesis did not produce a large enough fractionation to explain the natural variation (Dole et al., 1947). However, observations that as oxygen was consumed by respiration in the ocean, δ¹⁸O increased (Rakestraw et al., 1951), renewed interest in the biological fractionation of oxygen isotopes as the cause of the Dole Effect (Figure 2.1). Lane and Dole measured the oxygen isotope discrimination during respiration of several organisms (from molds to humans) and used their findings to formally propose that the Dole Effect could be explained as the global sum of respiration, $C_6H_{12}O_6 + 6O_2 \rightarrow 6CO_2 + 6H_2O$, in the atmosphere (Lane and Dole, 1956).

In sum, photosynthesis produces O₂ with an isotope composition similar to that of water, and organisms preferentially metabolize ¹⁶O during respiration, leaving the atmosphere enriched in

^{18}O compared to water. Measurements of atmospheric O_2 with modern precision result in $\delta^{18}\text{O}_{\text{VSMOW}}$ values such as $23.5 \pm 0.3\text{‰}$ (Kroopnick and Craig, 1972), $23.88 \pm 0.02\text{‰}$ (Barkan and Luz, 2005) and $23.533 \pm 0.045\text{‰}$ (Young et al., 2014). Since the original measurements of Lane and Dole (1956), fractionation factors for bacteria and yeast (Schleser, 1979), cytochrome oxidase (COX) and alternative oxidation (AOX) pathways (Guy et al., 1989), human respiration (Epstein and Zeiri, 1988) and discrimination during oxygen uptake by Rubisco, glycolate oxidase and the Mehler reaction (Guy et al., 1993; Helman et al., 2005), marine organisms (Kidson et al., 1993) and root respiration (Angert and Luz, 2001) were measured. These oxygen isotope discrimination factors ranged from approximately -6 to -31‰.

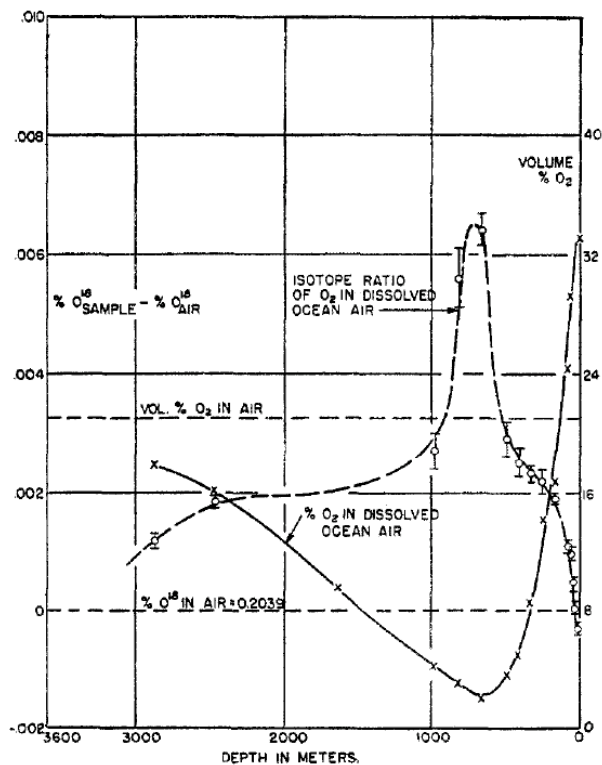


Figure 2.1: Volume of O_2 as a percentage of air dissolved in Pacific seawater (solid line) decreases with depth down to ~ 800 m as the difference between $\%^{18}\text{O}_{\text{sample}}$ and $\%^{18}\text{O}_{\text{air}}$ (dashed line) increases concurrently (Rakestraw et al., 1951).

Isotopic fractionation can also occur due to diffusion. In essence, O₂ must be transported to the site of consumption before respiration occurs. When oxygen is diffusion limited, O₂ of any isotopic composition that reaches the consumption site is consumed, masking intrinsic respiration fractionation factors (Guy et al., 1989). This is particularly true for any organism where the surface area is small compared to the volume and has been confirmed in a range of organisms (Epstein and Zeiri, 1988; Kiddon et al., 1993). In essence, large animals have much smaller apparent respiration fractionation factors (but are a small component of the oxygen cycle) compared to those of small aquatic organisms [that are a much greater component of the oxygen cycle (Bender et al., 1994)]. A more quantitative discussion of diffusion and isotopes will be presented in the following section, “*δ¹⁷O and the triple oxygen isotope parameter.*”

Two additional processes are thought to contribute to the Dole Effect, evapotranspiration and stratospheric chemistry. Water vapor can evaporate through leaf stomata, leaving behind a water that is isotopically heavy compared to the bulk isotopic composition of water for that region. Leaf water enriched due to this evapotranspiration may contribute to the Dole Effect by as much as 4 to 8‰ (Dongmann et al., 1974; Farquhar et al., 1993). Finally, in the stratosphere, O₂ is broken apart by ultraviolet (UV) light and the resulting atomic oxygen recombines with O₂ to make ozone. Ozone is enriched in heavy isotopes and transfers these to CO₂ by isotope exchange (Yung et al., 1991). This net removal of heavy isotopes of oxygen from the atmospheric O₂ pool decreases δ¹⁸O in the atmosphere by less than 0.5‰ (Bender et al., 1994; Luz et al., 1999). However, even with the consideration of these two additional processes on the difference between water and atmospheric oxygen, the precise magnitude of the modern Dole

Effect remains challenging to fully account for, and this difficulty is exacerbated when examining records of past Dole Effect (Landais et al., 2010).

$\delta^{17}\text{O}$ and the triple oxygen isotope parameter

An inability to fully account for the magnitude of the Dole Effect (Bender et al., 1994) and the discovery of mass independent isotope exchange in the stratosphere (Thiemens and Heidenreich, 1983; Thiemens et al., 1995) inspired an additional isotope tracer utilizing the other rare stable isotope of oxygen, ^{17}O . Measured abundances of $^{18}\text{O}/^{16}\text{O}$ and $^{17}\text{O}/^{16}\text{O}$ are used in combination to define “triple oxygen isotope space.” I will describe the triple oxygen isotope parameter using the terminology of Young et al (2002); discussion of alternate terminologies can be found elsewhere (Angert et al., 2003; Young et al., 2014).

During mass dependent processes such as respiration, $^{18}\text{O}/^{16}\text{O}$ will be fractionated approximately twice as much as $^{17}\text{O}/^{16}\text{O}$, so the relationship between the fractionation factors from Eq. 2.2 is

$$\alpha_{17} = (\alpha_{18})^{\beta} . \quad (2.3)$$

Values of β characterizing the mass dependent fractionation of $^{18}\text{O}/^{16}\text{O}$ and $^{17}\text{O}/^{16}\text{O}$ are therefore ~ 0.5 , but they vary depending on whether the process is equilibrium (e.g. bond-breaking) or kinetic (e.g. transport), and how they are calculated likewise varies (Young et al., 2002). For instance, the β values of transport processes should be calculated using molecular or atomic masses that select for velocity as in

$$\beta = \frac{\ln\left(\frac{m_2}{m_1}\right)}{\ln\left(\frac{m_3}{m_1}\right)} \quad (2.4)$$

where m is an atomic (or molecular) mass and subscripts refer to three isotopes (i.e. ^{16}O , ^{17}O , ^{18}O). Then β (in this case referred to as β_{kin}) values are calculated from Eq. 2.4 as

$$\beta_{17/18,kin} = \frac{\ln(\alpha_{17})}{\ln(\alpha_{18})}. \quad (2.5)$$

The β values associated with equilibrium processes are calculated differently as

$$\beta_{17/18,Eq} = \frac{\left(\frac{1}{m_{16}} - \frac{1}{m_{17}}\right)}{\left(\frac{1}{m_{16}} - \frac{1}{m_{18}}\right)} \quad (2.6)$$

Here, the equation is derived from the declaration that differences in the squares of vibrational energies of a material depend on their isotopic masses. The reader is directed to Young, Galy & Nagahara (2002) for a full discussion of both transport/velocity and bond-breaking/vibrational energy fractionation factors. Solving equations 2.5 and 2.6 produces values of $\beta_{17/18, kin, atomic} = 0.515$, $\beta_{17/18, kin, molecular} = 0.509$ and $\beta_{17/18, Eq} = 0.529$ (Table 2.4).

These calculated β values provide a framework for examining isotope fractionation processes in nature. Stable isotope measurements of both $^{18}\text{O}/^{16}\text{O}$ ratios and $^{17}\text{O}/^{16}\text{O}$ permit the extraction of β values from suites of natural samples believed to be representative of a fractionation process.

This is achieved by rewriting Eq. 2.1 in logarithmic form as

$$\delta'^i = 10^3 \ln\left(\frac{{}^i\text{R}_{\text{sample}}}{{}^i\text{R}_{\text{standard}}}\right) \quad (2.7)$$

and then substituting α_i so that

$$\delta'^i = 10^3 \ln(\alpha_i) , \quad (2.8)$$

Eq. 2.3 can be rewritten as

$$\delta'^{17}\text{O} = \beta\delta'^{18}\text{O} - \left(\delta'^{17}\text{O}_{\text{ref}} + \beta\delta'^{18}\text{O}_{\text{ref}} \right) \quad (2.9)$$

where “ref” refers to a reference composition at any point on the line defined by Eq. 2.6, and a linear relationship between $\delta'^{18}\text{O}$ and $\delta'^{17}\text{O}$ is preserved (Hulston and Thode, 1965). The difference from the line defined by Eq. 2.9 and the isotopic composition of a material is then defined as

$$\Delta'^{17}\text{O} = \delta'^{17}\text{O} - \beta\delta'^{18}\text{O} + \left(\delta'^{17}\text{O}_{\text{ref}} + \beta\delta'^{18}\text{O}_{\text{ref}} \right) . \quad (2.10)$$

Therefore, $\Delta'^{17}\text{O}$ describes an excess or deficit of $^{17}\text{O}/^{16}\text{O}$ in a sample relative to a fractionation line with slope β . This excess or deficit is normally reported in parts per million (ppm).

In the stratosphere, photochemical reactions drive mass-independent fractionations (those that do not scale with the mass of the isotope species) in oxygen into carbon dioxide and ozone, and these isotope anomalies are then inherited by O_2 . However, the isotopic composition of atmospheric oxygen is also influenced by photosynthesis [which inherits both the $\delta^{18}\text{O}$ and $\delta^{17}\text{O}$ of the source water (Helman et al., 2005)] and respiration, a mass-dependent fractionation process (Angert et al., 2003; Helman et al., 2005). Therefore, $\Delta'^{17}\text{O}_{\text{air}}$ is a balance between the mass independent photochemistry in the stratosphere and mass dependent respiration at Earth’s surface.

The balance between photochemistry and biological reactions has been exploited as a measure of primary productivity in the ocean where $O_{2, \text{air}}$ (with its isotopic anomalies) is dissolved in surface waters and mixes with the photosynthetically produced and mass-dependently fractionated $O_{2, \text{bio}}$ (Hendricks et al., 2005; Luz and Barkan, 2000; Prokopenko et al., 2011). This method is highly dependent on the values of $\Delta'^{17}O_{\text{air}}$ and β used in equations that estimate primary productivity, and these values are discussed below.

$\Delta'^{17}O_{\text{air}}$ and β

One of the challenges in measuring $\Delta'^{17}O_{\text{air}}$ lies in the necessity to compare the isotope ratios in air to a standard material. Atmospheric O_2 itself, due to the simplicity of obtaining it, is often used a reference material, and therefore defined as $\Delta'^{17}O_{\text{air}} = 0$. For instance, dissolved O_2 in seawater may be compared to $O_{2, \text{air}}$ to estimate primary productivity as described above (Luz et al., 1999). Additionally, modern air has been used as a standard for comparison to archives of air trapped in ice cores to examine past changes in global primary productivity (Blunier et al., 2002; Blunier et al., 2012). This approach is problematic because $O_{2, \text{modern air}}$ is a single datum that cannot solely define a fractionation line in triple-isotope space, and assumptions made regarding how various processes alter triple-isotope values are unlikely to hold when considering past archives of O_2 (Young et al., 2014). Therefore either the triple oxygen isotope composition of water or rocks such as San Carlos Olivine are perhaps better reference materials for quantifying $\Delta'^{17}O_{\text{air}}$.

Measurements of $\Delta^{17}\text{O}_{\text{air}}$ compared to biologically-cycled terrarium O_2 showed that $\Delta^{17}\text{O}_{2, \text{bio}}$ was 155 ppm above a line defined by $\beta = 0.521$ (derived from observed $\delta^{18}\text{O}$ and $\delta^{17}\text{O}$ values of terrarium O_2), and that $\Delta^{17}\text{O}_{\text{VSMOW}}$ was enriched by 184 ppm on a line defined by $\beta = 0.521$ where $\delta^{18}\text{O}_{\text{VSMOW}} = -22.960\text{‰}$ and $\delta^{17}\text{O}_{\text{VSMOW}} = -11.778\text{‰}$ when compared to air [see (Luz et al., 1999) for the definition of $\Delta^{17}\text{O}$ in contrast to $\Delta'^{17}\text{O}$]. A value for $\Delta'^{17}\text{O}_{\text{air}} = -344 \pm 15$ ppm when compared to a line defined by 52 measurements of terrestrial rock samples with $\beta = 0.5237$ (Pack et al., 2007). At UCLA, repeated measurements of atmospheric O_2 against a reference gas that has been calibrated using the isotopic composition of San Carlos olivine yield $\Delta'^{17}\text{O}_{\text{air}} = -373.6 \pm 4.8$ ppm (1σ , $n = 37$) from a line defined by $\beta = 0.528$ (Young et al., 2014).

These estimates of $\Delta'^{17}\text{O}_{\text{air}}$, and in fact all estimates of $\Delta'^{17}\text{O}$, are extremely sensitive to β , which varies depending on the fractionation process. These processes can be somewhat isolated in laboratory experiments, but uncertainty remains. For instance, β values of 0.516, 0.514 and 0.506 were experimentally determined for respiration through the COX, AOX and photorespiration pathways respectively (Angert et al., 2003), however later workers measured a β value of 0.512 for photorespiration (Helman et al., 2005). These uncertainties stem in part from the fact that β values measured in such experiments are actually the result of several summed fractionation processes including diffusion into cells and bond breaking at the enzyme. Slight variations during experiments in the parameters that influence these individual steps (e.g. temperature and the partial pressure of O_2) likely account for some of this disagreement in the effective β values. Finally, natural samples of O_2 are the result of multiple processes, therefore β values that can be determined through measurements of $\delta^{18}\text{O}$ and $\delta^{17}\text{O}$ are also effective rather than intrinsic.

Due to these uncertainties, it is difficult to quantify the contributions of various processes to $\Delta^{17}\text{O}_{\text{air}}$ signals in the modern, much less in past atmospheres. For instance, one estimate suggests that respiration and evapotranspiration account for 57% and 10% respectively of the $\Delta^{17}\text{O}_{\text{air}}$ value (Young et al., 2014) is in stark contrast with estimates that 83% of the $\Delta^{17}\text{O}_{\text{air}}$ signal is due to stratospheric chemistry (Bao et al., 2008).

In short, although measuring abundances of ^{18}O and ^{17}O in O_2 has been useful for tracing both the biological and photochemical processes that alter its composition, bulk isotope tracers are not sufficient for distinguishing these processes from one another in either the modern or the past. Two additional oxygen isotope tracers were developed in aid of this persistent challenge; clumped isotopes of oxygen are described below.

Clumped isotopes, bond reordering and transport

Notation

Molecular oxygen has six isotopologues, molecules that vary from one another in isotopic composition only. (Table 2.1) While ratios of $^{18}\text{O}^{16}\text{O}/^{16}\text{O}^{16}\text{O}$ and $^{17}\text{O}^{18}\text{O}/^{16}\text{O}^{16}\text{O}$ have been measured for decades as described above, advances in isotope ratio mass spectrometry were necessary to quantify others precisely (Huntington et al., 2009). The ratios of two such rare isotopologues ($^{18}\text{O}^{18}\text{O}/^{16}\text{O}^{16}\text{O}$ and $^{17}\text{O}^{18}\text{O}/^{16}\text{O}^{16}\text{O}$) were first measured at UCLA (Yeung et al., 2012).

Isotopologue	Mass (amu)	Relative abundance	Atmospheric abundance
$^{16}\text{O}^{16}\text{O}$	31.989829	1	0.2095
$^{16}\text{O}^{17}\text{O}$	32.994046	7.8×10^{-4}	1.6×10^{-4}
$^{16}\text{O}^{18}\text{O}$	33.994076	4.1×10^{-3}	8.6×10^{-4}
$^{17}\text{O}^{17}\text{O}$	33.998263	1.5×10^{-7}	3.1×10^{-8}
$^{17}\text{O}^{18}\text{O}$	34.998293	1.6×10^{-6}	3.4×10^{-7}
$^{18}\text{O}^{18}\text{O}$	35.998322	4.2×10^{-6}	8.8×10^{-7}

Table 2.1: The isotopologues of O₂ and their abundance [adapted from (Yeung et al., 2012)].

While traditional stable isotope measurements are reported against a standard such as VSMOW, clumped isotope measurements are reported against the stochastic distribution of isotopologues using “big delta” notation where

$$\Delta_{36} = \left(\frac{{}^{36}\text{R}_{\text{measured}}}{{}^{36}\text{R}_{\text{stochastic}}} - 1 \right) \quad (2.11)$$

and

$$\Delta_{35} = \left(\frac{{}^{35}\text{R}_{\text{measured}}}{{}^{35}\text{R}_{\text{stochastic}}} - 1 \right). \quad (2.12)$$

Here, ${}^x\text{R}$ are molecular ratios so that

$${}^{36}\text{R}_{\text{measured}} = \frac{[{}^{36}\text{O}_2]}{[{}^{32}\text{O}_2]}, \quad (2.13)$$

$${}^{35}\text{R}_{\text{measured}} = \frac{[{}^{35}\text{O}_2]}{[{}^{32}\text{O}_2]}, \quad (2.14)$$

$${}^{36}\text{R}_{\text{stochastic}} = \frac{[{}^{18}\text{O}][{}^{18}\text{O}]}{[{}^{16}\text{O}][{}^{16}\text{O}]} = ({}^{18}\text{R})^2 \quad (2.15)$$

and

$${}^{35}\text{R}_{\text{stochastic}} = 2 \frac{[{}^{18}\text{O}][{}^{17}\text{O}]}{[{}^{16}\text{O}][{}^{16}\text{O}]} = 2 {}^{18}\text{R} {}^{17}\text{R}. \quad (2.16)$$

These stochastic ratios are predictions of abundances of these rare isotopologues based on random chance for a given bulk isotopic composition. Δ_n values then, are a deviation from this prediction where $\Delta_n = 0$ is no different than the random distribution of isotopes, $\Delta_n > 0$ has more multiply-substituted isotopologues than random chance predicts and $\Delta_n < 0$ has fewer rare isotopologues than random chance predicts (Figure. 2.2).

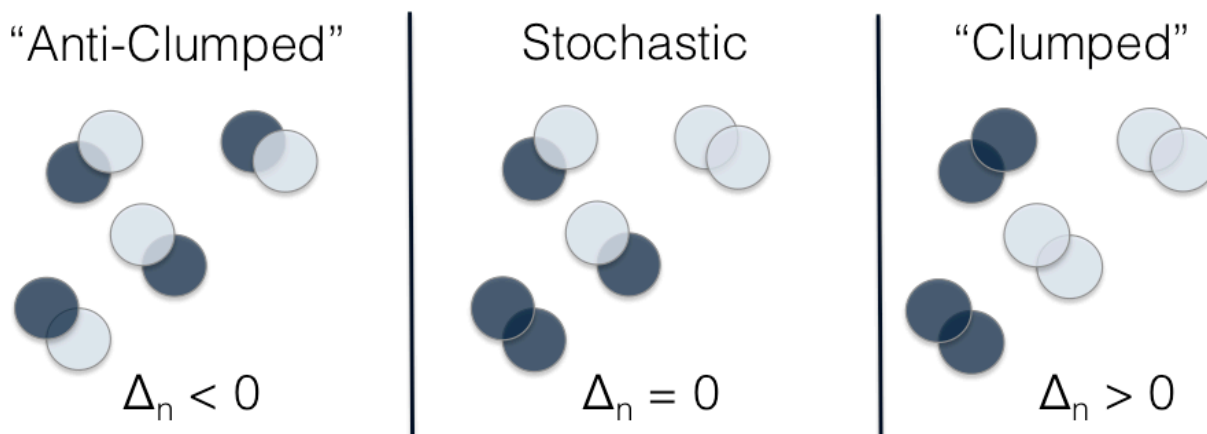


Figure 2.2: A graphical representation anti-clumped, stochastic and clumped distributions (left to right). The pale circles represent a common, light isotope such as ^{16}O while the dark circles represent a heavy molecule such as ^{17}O or ^{18}O . Overlapping circles represent O_2 as a diatomic molecule. In each panel, the clumped isotope distributions are different, but the stable isotope composition are identical.

How multiple-isotope substitutions differ from single substitutions

An important distinction of clumped isotope geochemistry from stable isotope geochemistry is that it is a measure of “bond-ordering,” a phrase intended to reference descriptions of crystal structure by the arrangement or “ordering” of atoms within a unit cell as isotopes are ordered within a molecule. In other words, measurements of stable isotopes seek to describe the

abundance of rare isotopes, but clumped isotope measurements seek to describe the abundance of rare isotopes bonded to one another.

An additional dissimilarity between these two tracers is that stable isotopes are sensitive to the isotopic composition of substrates, often referred to as “the reservoir effect,” as well as temperature. For example, because there is virtually no fractionation of oxygen isotopes during photosynthesis, the isotopic composition of photosynthetic O₂ will vary with isotopic composition of water. Natural waters vary by tens of per mil in oxygen isotopic composition (Craig, 1961), so there is no universal stable isotope identifier of photosynthesis. However, the bond formation chemistry that occurs at the Photosystem II enzyme during photosynthesis is universal and potentially traceable with clumped isotope measurements regardless of the isotopic composition of the substrate. This topic is the subject of the following chapter.

A careful understanding of the effects of various physical and chemical processes on the distribution of clumped isotopes in O₂ is necessary to interpret these signals in natural materials. Experiments that stimulated bond breaking and formation in O₂ through photochemistry and repeated clumped-isotope measurements of atmospheric O₂ were carried out at UCLA from 2013-2014. Knudsen diffusion experiments were carried out that to investigate β values for transport processes for molecules of O₂. Key findings from this work will be briefly summarized here, but the reader is referred to the published work for further details (Yeung et al., 2014; Yeung et al., 2016; Yeung et al., 2012).

Δ_{36} and Δ_{35} in equilibrium photochemical reactions and the atmosphere

We measured Δ_{36} and Δ_{35} in O_2 that had been isotopically exchanged through $O(^3P) + O_2$ reactions stimulated by UV at temperatures ranging from 200-250K and determined that O_2 had been reordered to isotopic equilibrium in some agreement with theoretical predictions (Wang et al., 2004) (Figure 2.3). Variations from theoretical predictions are due to reordering of O_2 isotopologues during a purification step and are discussed in detail in Yeung et al., 2014.

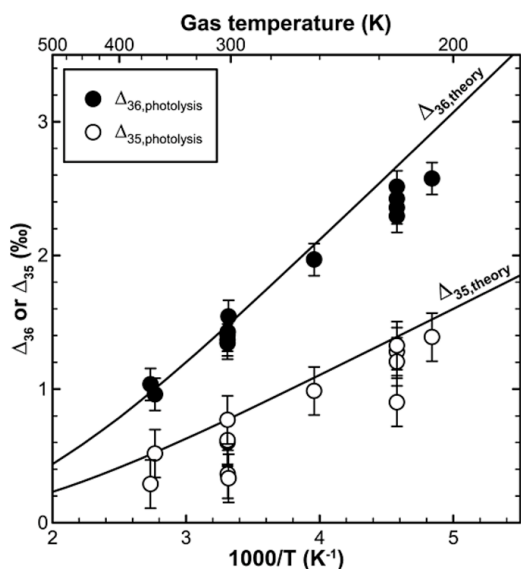


Figure 2.3: Inverse relationship between temperature and Δ_{36} and Δ_{35} from photolysis experiments at steady state is shown as black and open circles respectively. Solid black lines represent the theoretical equilibrium values of Δ_{36} and Δ_{35} (Yeung et al., 2014).

Furthermore, we measured atmospheric O_2 collected from UCLA's Court of Sciences from 2012 to 2014. These repeated analyses permitted us to precisely assign values of $\Delta_{36} = 1.97 \pm 0.07\text{‰}$ and $\Delta_{35} = 1.0 \pm 0.1\text{‰}$ (Figure 2.4). This Δ_{36} value corresponds to a temperature of 260 ± 5 K, implying that Δ_{36} is out of equilibrium with both annual mean local and global temperatures of 290 K and 288 K, respectively. Rather, the clumped isotope composition of tropospheric O_2 is the result of the decadal-scale mixing of O_2 reordered at cold stratospheric temperatures with that reordered at warmer temperatures in the troposphere. Variations in the Δ_{36} and Δ_{35} values from

the troposphere to the mid-stratosphere were confirmed by measurements made at UCLA and Rice University (Yeung et al., 2016) (Figure 2.5).

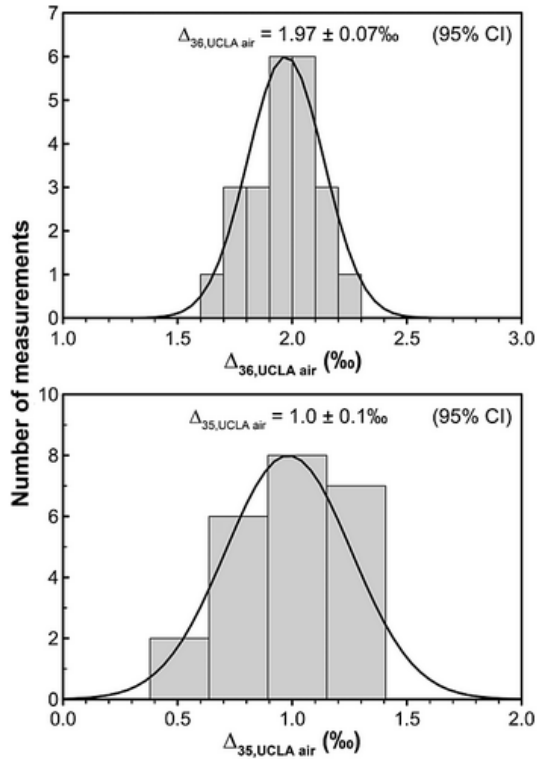


Figure 2.4 (left): Histograms of Δ_{36} and Δ_{35} values measured in UCLA air O_2 from 2012-2014. Mean values and 95% confidence intervals are listed (Yeung et al., 2014).

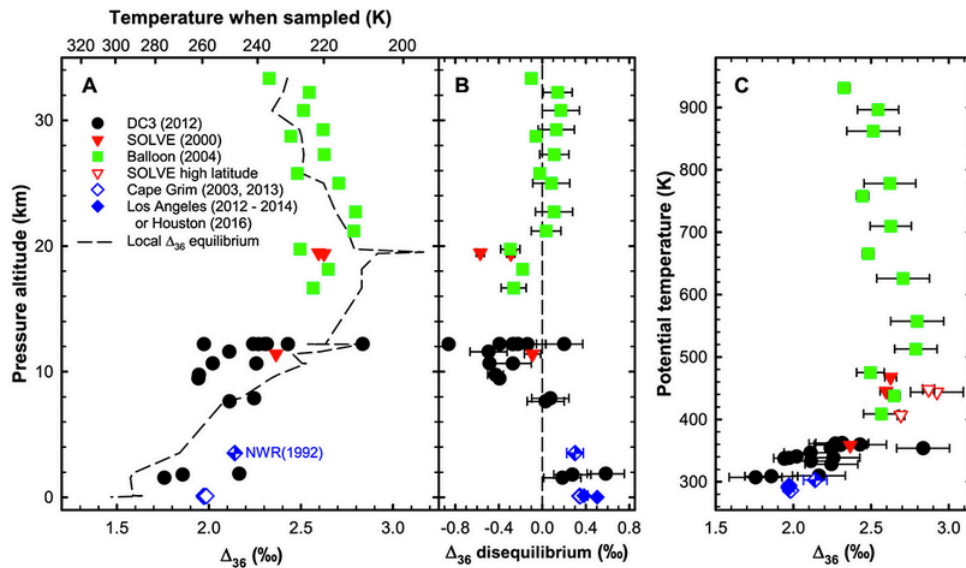


Figure 2.5 (below): Δ_{36} values versus height as pressure altitude (A). Shown in (B) is the degree of Δ_{36} disequilibrium from temperatures at which air was sampled (denoted as dashed line). Δ_{36} values versus potential temperature (C). Error bars shown are 1σ except for surface samples which are 1 standard error of the mean; neither are shown in (A) for clarity.

β values for transport and bond breaking processes in multiply substituted isotopologues

Knudsen diffusion experiments (where gas flows through an orifice smaller than the mean free path of that gas) were performed at UCLA to examine β_{diff} (hereafter, the subscript “*diff*” will denote that this is the β value associated with multiply substituted isotopologues and “*kin*” the β value associated with singly-substituted isotopologues). In the case of Knudsen diffusion, the flux of gas through the orifice is inversely proportional to the square root of its mass so that relevant α fractionation factors can be predicted as

$$\alpha_{m_i} = \frac{m_i R_{diffused}}{m_i R_{initial}} = \sqrt{\frac{m_{32}}{m_i}} \quad (2.17)$$

where m here is the molecular mass and i is the multiply-substituted isotopologue. Then β_{diff} values are calculated from Eq. 2.17 as

$$\beta_{i/34,diff} = \frac{\ln(\alpha_i)}{\ln(\alpha_{34})}. \quad (2.18)$$

Transport processes like diffusion are strongly dependent on the velocities of molecules and this is reflected in the calculations in Eq. 2.17 and 2.18. This can be contrasted to how equilibrium β values are calculated for multiply-substituted isotopologues. Here, vibrational energies are selected for rather than velocities to highlight the importance of bond stability in processes that break and create bonds (such as respiration). Here, β values will be denoted as β_{BB} , where “*BB*” signifies bond breaking. This serves to delineate it from the β_{Eq} used for singly substituted isotopes as well as call out that respiration is not an equilibrium process, but a consumption process that destroys bonds by selecting them in a mass dependent fashion. The use of reduced masses is required to highlight this dependence on vibrational frequencies for bond-breaking processes. Reduced masses are calculated as

$$\mu_i = \frac{Mm_i}{M + m_i} \quad (2.19)$$

where M is a mass M bonded to an isotope with mass m_i . Therefore,

$$\alpha_i = \sqrt{\frac{\mu_{32}}{\mu_i}} \quad (2.20)$$

and

$$\beta_{i/34, BB} = \frac{\ln(\alpha_i)}{\ln(\alpha_{34})} \quad (2.21)$$

Solving Eq. 2.18 yields $\beta_{33/34, diff} = 0.509$, $\beta_{35/34, diff} = 1.479$ and $\beta_{36/34, diff} = 1.943$ while solving Eq. 2.21 yields $\beta_{33/34, BB} = 0.522$, $\beta_{35/34, BB} = 1.553$ and $\beta_{36/34, BB} = 2.061$. β values derived from Knudsen diffusion experiments carried out at UCLA are in good agreement with the calculated β_{diff} values (Yeung et al., 2012). All values for β_{diff} and β_{BB} are listed in Table 2.4.

Materials and Methods

Water sampling

Surface waters were sampled from Lake Houston's Deussen Park (29°55'7.1256" N, 95°8'56.9076" W) on June 15 and July 5, 2016 (hereafter referred to as LH1 and LH2) by casting a 20L Nalgene container from the dock and allowing it to fill with water (Figure 2.6). Upon retrieval, water was immediately partitioned into 300mL glass Wheaton Bottles, stoppered and covered in aluminum foil to stimulate dark respiration. Wheaton Bottles were prepared for this experiment by acid washing in 50:50 HCl and 50:50 NaOH cold rinses, then autoclaved. Evacuated 2L flasks pre-poisoned with 200 μ L of a saturated $HgCl_2$ were filled with ~400 mL

of cast water in order to determine the starting conditions of the following respiration experiment.



Figure 2.6: Sampling at Lake Houston. Pictured are the location of water sampling, flasks and Wheaton Bottles.

Respiration experiments

Waters were immediately transported to Rice University's Stable Isotope Lab for incubation at room temperature; time from first sampling to lab was on the order of 2 hours. Ideally, temperature would be controlled for immediately upon sampling into Wheaton Bottles [as temperature controls the rate of respiration and isotopic fractionation i.e., (Degens et al., 1968)], but such precision was beyond the scope of these pilot studies. Wheaton Bottles were placed in a dark cabinet out of direct sunlight to limit temperature variations for the remainder of incubation. One bottle was immediately unsealed and monitored with a calibrated Lazar Micro Oxygen Electrode as a gauge for the rate of respiration to guide sampling throughout the experiments.

At intervals throughout the respiration experiment, Wheaton Bottles were unsealed and water siphoned into 1L, 2L, and 5L flasks evacuated and pre-poisoned as above to halt respiration. The size of the flask was determined by the number of Wheaton Bottles needed for combination to keep the final amount of O₂ to be analyzed between ~60-90 μmols and to keep the total volume of water less than half that of the flask. Filled flasks were transferred to a rotating shaker table where the dissolved O₂ equilibrated with the flask headspace for 48 hours.

O₂ extraction, purification and mass spectrometry

Equilibrated flasks were placed upside down and water removed to an evacuated flask held under constant low vacuum until <10mL water remained in the poisoned flask. At this point, the poisoned flask was isolated and moved to a vacuum line where the residual water was held at -40°C and headspace air was transferred over two U-shaped traps held at -196°C (for drying) to a silica gel finger.

Sample purification and mass spectrometry methods are similar to those described in (Yeung et al., 2012), but have been updated with an automatic sample preparation line and the use of high resolution mass spectrometry. These will be covered here briefly as they are the topic in detail of a paper currently in preparation (Hu et al., 2017).

Samples of O₂ on silica gel fingers are moved to an automated O₂ purification system held at high vacuum with an inline gas chromatograph shown schematically in Figure 2.7. Here, gas samples are expanded off of the silica gel, cryogenically dried once more, then pre-concentrated

onto a silica-filled U-trap prior to GC injection. Upon injection, the U-trap is heated to 90°C and flushed with helium for transfer to the GC column, which is held at -80°C to separate O₂ from Ar and N₂. Baseline resolution achieved by cryogenic separation of O₂ and Ar permits each peak to be integrated (see Figure 2.7 inset). Then, the ratio of these O₂ and Ar peak areas are compared to those in air so that $\delta(\text{O}_2/\text{Ar})_{\text{air}} = [(\text{O}_2/\text{Ar})_{\text{dissolved}}/(\text{O}_2/\text{Ar})_{\text{air}} - 1]$ and reported as per mil differences from air. After Ar is eluted, O₂ is recollected on a U-trap filled with silica gel and held at -196°C until the collection is finished and excess He is pumped out. Finally, O₂ is warmed to 90°C for 5 minutes prior to transfer to the isotope-ratio mass spectrometer (IRMS).

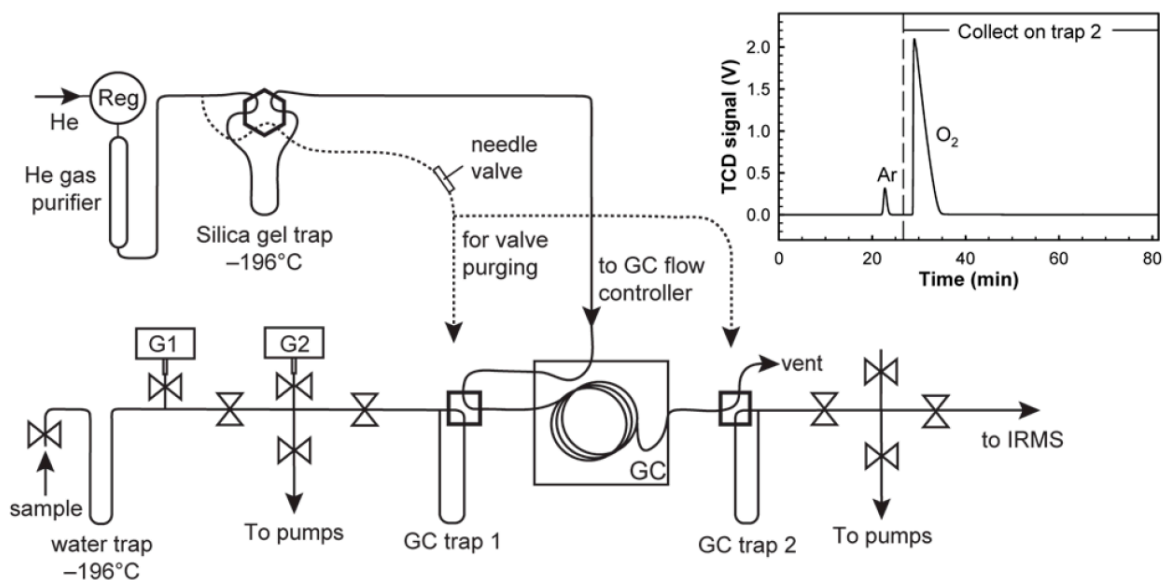


Figure 2.7: A schematic of the automated O₂ purification system. The inset shows the separation of O₂ and Ar (an important mass 36 interference) typically achieved during purification (Hu et al., 2017).

After this final purification step, O₂ is transferred cryogenically to a cold prep finger adjacent to the mass spectrometer sample bellows for expansion and measurement relative to a laboratory working gas. The mass spectrometer used is a modified Nu Instruments *Perspective IS* IRMS

that typically achieves a mass resolving power (MRP) over 4500 where $MRP = m_{36}/(m_{95\%}-m_{5\%})$. This increase in MRP from prior methods resolves mass interferences that were known to be an issue such as Ar (Yeung et al., 2012) in addition to others that were not. For instance $^{35}\text{Cl}^+$ (34.9689 amu) is resolved from $^{17}\text{O}^{18}\text{O}^+$ (34.9983 amu) on $m/z = 35$ and $^{36}\text{Ar}^+$ (35.9676 amu) as well as H^{35}Cl^+ (35.9767 amu) is resolved from $^{18}\text{O}^{18}\text{O}$ (35.9983 amu) on $m/z = 36$. Bulk isotopic compositions are reported relative to air (we assume $\delta^{18}\text{O}_{\text{VSMOW}} = 23.880\text{‰}$ and $\delta^{17}\text{O}_{\text{VSMOW}} = 12.080\text{‰}$) and clumped isotope distributions are reported relative to the stochastic distribution.

Samples are run within a rotating bevy of standards used in previous work such as O_2 generated from heating barium peroxide powder in sealed glass tubes at high temperatures (Yeung et al., 2012) and O_2 equilibrated by photolysis at low-temperature (Yeung et al., 2014) in addition to air and air dissolved in water.

Results

O_2/Ar ratios

During the course of these respiration studies, eight air samples dissolved in water were measured (Table 2.2) and found to have $\delta(\text{O}_2/\text{Ar})_{\text{air}} = -90.6 \pm 2.1\text{‰}$ (95% CI), indistinguishable from the expected value of -91.9‰ at 25°C equilibrium (Garcia and Gordon, 1992; Hamme and Emerson, 2004). For LH1 and LH2, $\delta\text{O}_2/\text{Ar}$ ratios at $t = 0$ are -185.41‰ and -311.998‰ respectively and decrease linearly to -459.406‰ and -730.296‰ respectively (Figure 2.8, Table 2.3). The fraction of O_2 consumed is determined by assuming that $\delta\text{O}_2/\text{Ar}_{t=0}$ is 100% of the O_2 .

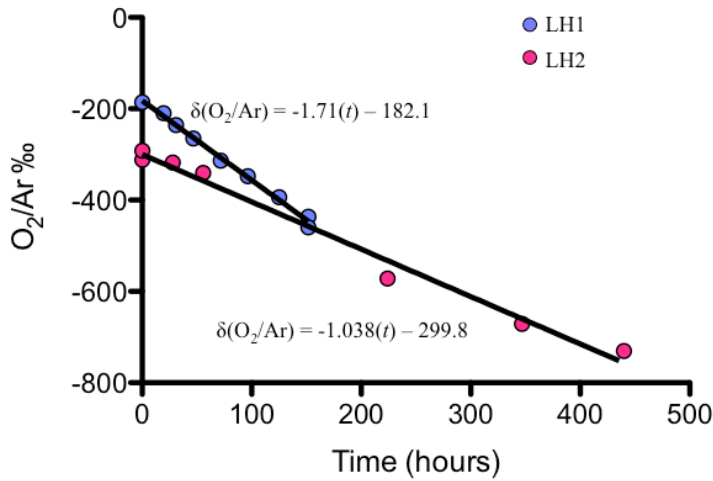


Figure 2.8: O_2/Ar ratios for LH1 and LH2 as a function of time. 95% CI error bars from repeated measurements of air dissolved in water are smaller than symbols.

Table 2.2: Isotopic compositions and O_2/Ar ratios for air dissolved in distilled H_2O at $25^\circ C$

Sample	$\delta(O_2/Ar)_{air}$ ‰	$\delta^{18}O$ ‰	$\Delta^{17}O$ ppm*	Δ_{35} ‰	Δ_{36} ‰
1	-89.5	0.723	7	0.908	1.926
2	-89.8	0.703	13	0.911	1.862
3	-90.1	0.626	12	0.971	2.003
4	-91.2	0.619	10	0.947	1.944
5	-92.9	0.704	2	0.946	1.967
6	-91.5	0.775	4	0.811	1.962
7	-91.2	0.776	4	0.770	1.971
8	-88.5	0.716	15	1.043	1.910
Mean $\pm 1\sigma$	-90.6 ± 1.4	0.706 ± 0.058	9 ± 5	0.913 ± 0.087	1.943 ± 0.044
Mean $\pm 95\%$ CI	-90.6 ± 2.1	0.706 ± 0.058	9 ± 5	0.913 ± 0.080	1.943 ± 0.053

* $\Delta^{17}O \equiv \ln(\delta^{17}O + 1) - 0.518 \times \ln(\delta^{18}O + 1)$. Data from (Hu et al., 2017).

Table 2.3: Isotopic compositions and O_2/Ar ratios for Lake Houston respiration

Experiment	Time (hours)	$\delta(O_2/Ar)_{air}$ ‰	f	$\delta^{18}O$ ‰	$\Delta^{17}O$ ppm*	Δ_{35} ‰	Δ_{36} ‰
LH1	0	-185.4	1.0	-0.17	35	0.942	1.767
LH1	19.67	-209.7	0.97	0.68	50	1.117	1.854
LH1	30.92	-235.8	0.94	1.43	49	0.976	1.812
LH1	46.9	-264.8	0.90	1.81	51	0.970	1.877
LH1	71.8	-313.8	0.84	3.11	63	1.086	1.866
LH1	96.42	-347.8	0.80	4.31	58	1.004	1.961
LH1	125.17	-394.0	0.74	6.46	66	1.016	1.922
LH1	151.67	-436.3	0.69	7.26	68	0.973	1.944
LH2	0	-312.0	1.0	0.47	26	1.025	1.948
LH2	0	-291.4	1.03	0.36	25	0.969	1.884
LH2	27.9	-317.9	0.99	1.45	32	0.946	1.924
LH2	55.7	-340.0	0.96	2.46	28	1.040	1.949
LH2	223.9	-571.7	0.62	12.55	62	1.198	2.239
LH2	346.8	-670.8	0.48	17.35	88	1.366	2.382
LH2	439.8	-730.3	0.39	20.95	61	1.269	2.564

$\Delta^{17}O \equiv \ln(\delta^{17}O + 1) - 0.518 \times \ln(\delta^{18}O + 1)$. See text for estimates of errors.

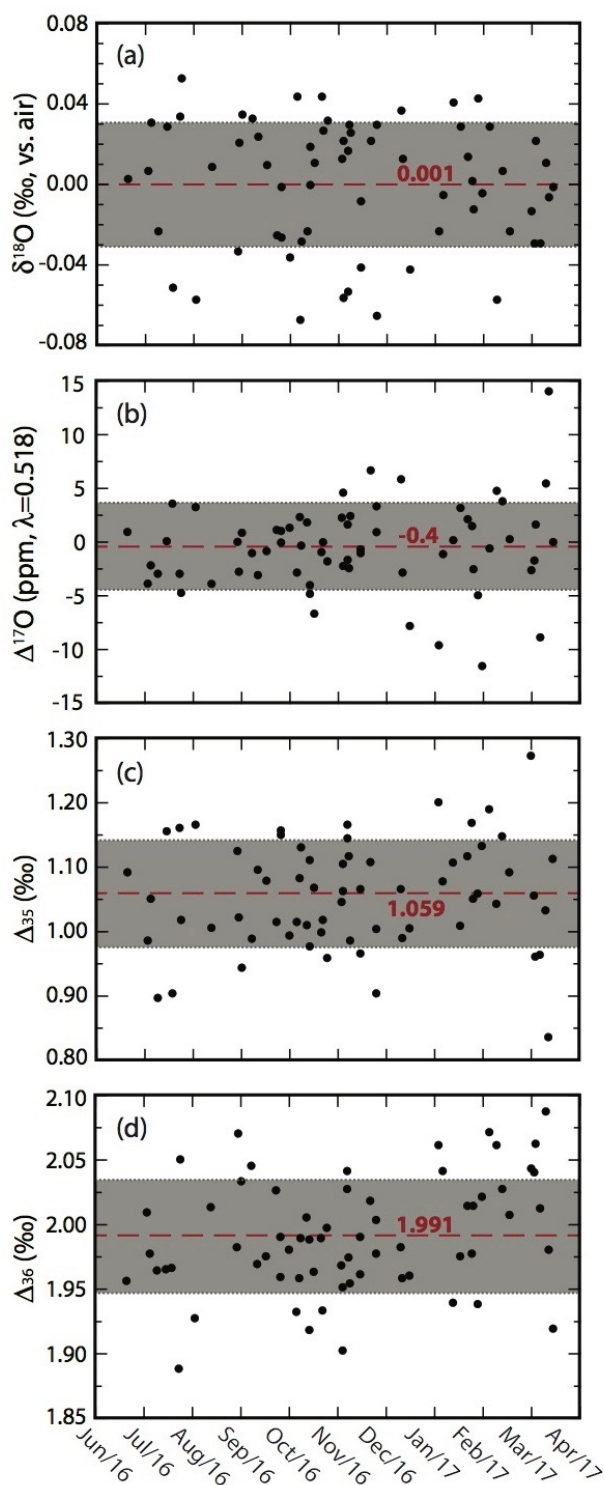
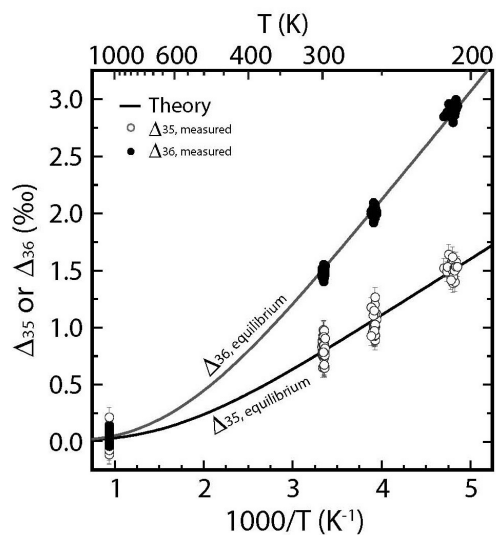


Figure 2.9 (left): O₂ air samples run from June 2016 to April 2017. Red dashed line is average value, grey bar is 1 σ . Data from (Hu et al., 2017).

Figure 2.10 (below): Photolysis experiment Δ_{35} (open circles) and Δ_{36} (black circles) inversely correlate with temperature. Solid black line is the theoretical equilibrium temperature curve. Error bars shown are 0.09‰ for Δ_{35} and 0.039‰ for Δ_{36} (1 σ , $n = 86$). Data from (Hu et al., 2017).



Air and Photolysis Measurements

Samples of O₂ purified from atmosphere collected from the third floor balcony of the Rice University's Wiess Geology Lab were measured from June 2016-April 2017 (Figure 2.9). Average values for this time period were determined to be $\delta^{18}\text{O}_{\text{air}} = 0.001 \pm 0.031\text{‰}$, $\Delta'^{17}\text{O}_{\text{air}, 0.518} = -0.4 \pm 4.1$ ppm, $\Delta_{36} = 1.991 \pm 0.044\text{‰}$ and $\Delta_{35} = 1.06 \pm 0.08\text{‰}$ [1σ , $n = 65$ (Hu et al., 2017)]. Photolysis experiments following a previously published method (Yeung et al., 2014) were also run over this time period and are shown in Figure 2.10 (Hu et al., 2017). No average values are reported for these standards as slight variations in the photolysis temperature are unavoidable, thus each photolysis Δ_n value is compared to $\Delta_{n, T}$ where T is the theoretical value at the experiment temperature.

Stable and Clumped Isotope Values

Values of $\delta^{18}\text{O}$, $\Delta'^{17}\text{O}$, Δ_{35} and Δ_{36} for LH1 and LH2 are listed in Table 2.3 and shown varying with time in Figure 2.11. During the course of LH1 and LH2, 31% and 61% of the initial O₂ concentrations were consumed respectively. At $t = 0$, $\delta^{18}\text{O}$ values are -0.172‰ and 0.469‰ for LH1 and LH2 respectively, and they increase linearly to 7.48‰ and 20.95‰ respectively (Figure 2.11). A β value of 0.518 produces $\Delta'^{17}\text{O}$ values of 35 ppm at $t = 0$ that increase to 68 ppm for LH1 and values of 26 ppm at $t = 0$ that increase to 88 ppm for LH2. During LH1, average Δ_{35} value is $1.01 \pm 0.06\text{‰}$ with no discernable trend through time. However Δ_{35} values during LH2 increase from 1.025‰ at $t = 0$ to 1.27‰ . LH1 and LH2 values of Δ_{36} increase from 1.77‰ at $t = 0$ to 1.94‰ and from 1.95‰ at $t = 0$ to 2.56‰ respectively.

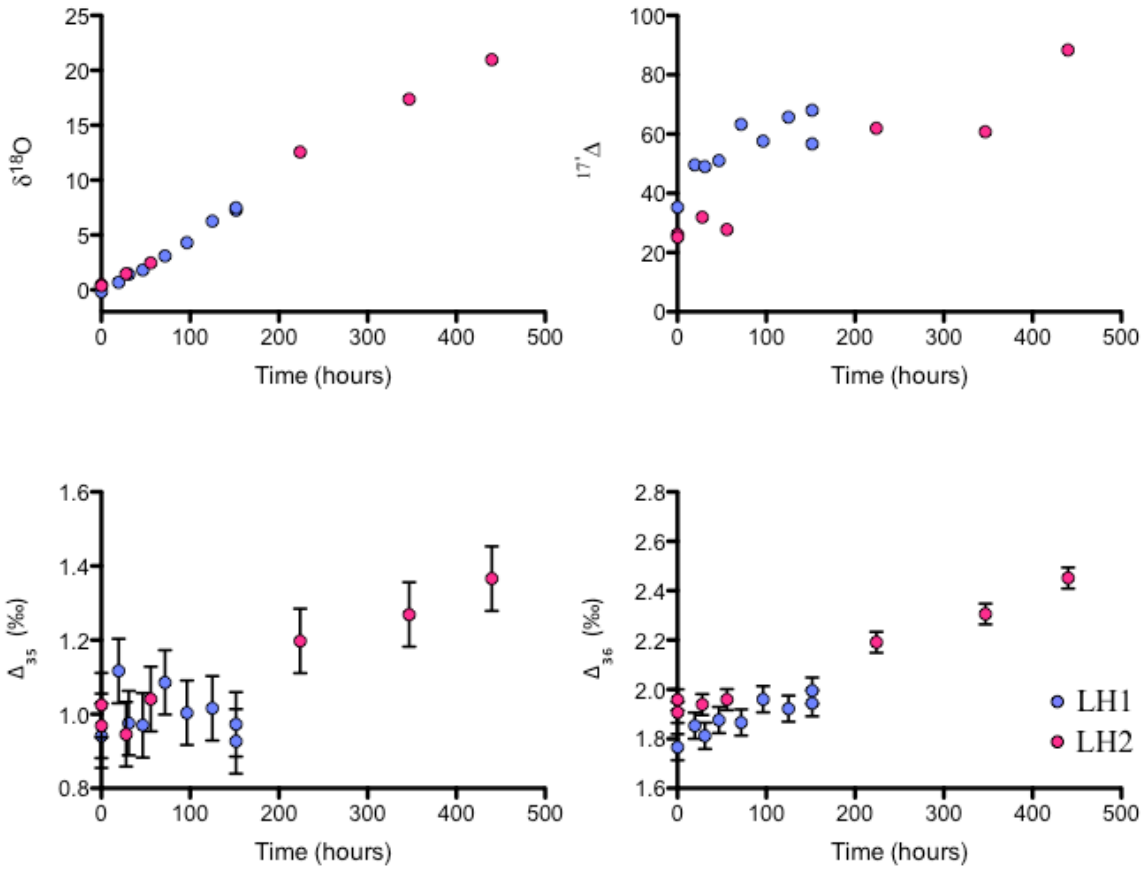


Figure 2.11: Variations in $\delta^{18}\text{O}$, $\Delta^{17}\text{O}$, Δ_{35} and Δ_{36} for LH1 (blue circles) and LH2 (pink circles) as a function of time. Error bars are 95% CI from replicate measurements of air dissolved in water are smaller than symbols for $\delta^{18}\text{O}$ and $\Delta^{17}\text{O}$.

$$\beta_{17/18}, \beta_{36/34}, \beta_{35/34}$$

The evolution of isotopes in these respiration experiments can be described by closed-system

Raleigh fractionation to derive β_{resp} fractionation factors where

$$\alpha_{resp} = \frac{\ln\left(\frac{R}{R_0}\right)}{\ln(f)} + 1 \quad (2.22)$$

and

$$\beta_{i/j, resp} = \frac{\ln({}^i\alpha)}{\ln({}^j\alpha)} \quad (2.23)$$

Here, $\beta_{17/18, resp}$ was determined to be 0.519 and 0.518 for LH1 and LH2 respectively. Values for $\beta_{36/34, resp}$ are 2.040 and 2.053 for LH1 and LH2 respectively. Values for $\beta_{35/34, resp}$ are 1.529 and 1.553 for LH1 and LH2 respectively. Finally, values for $\beta_{33/34, resp}$ are 0.519 and 0.518 LH1 and LH2 respectively. All β_{resp} values are listed in Table 2.4.

Table 2.4: Calculated β_{Eq} , $\beta_{kin, atomic/molecular}$, β_{diff} , β_{BB} and measured β_{resp}

i/j	β_{eq}	$\beta_{kin, atomic}$	$\beta_{kin, molecular}$	B_{diff}	β_{BB}	LH1 β_{resp}	LH2 β_{resp}
17/18	0.529	0.515	0.509	-	-	0.519	0.518
33/34	-	-	-	0.509	0.522	0.519	0.518
35/34	-	-	-	1.479	1.553	1.529	1.553
36/34	-	-	-	1.943	2.061	2.040	2.053

Discussion

Although the rates of respiration for these two experiments were quite different (LH1 respired ~60% faster than LH2), there is good agreement between the measured β_{resp} values. $\beta_{17/18, resp}$ values are similar to the 0.5179 “universal” respiration slope recommended for determining marine primary productivity (Luz and Barkan, 2005).

However, what has remained unclear is how much of the ~0.518 slope is due to diffusion and how much is due to respiration *sensu stricto* as a value of 0.518 lies almost exactly halfway between the predicted β_{eq} and $\beta_{kin, molecular}$ values of 0.529 and 0.509. By a simple weighted average calculation, the implication is that ~55% of these measured β_{resp} signals are due to

diffusion. This is in direct conflict with the many experiments that seek to distinguish diffusion effects from respiration effects [i.e. (Luz and Barkan, 2005) and references within] in that nearly all such experiments have β values that are quite similar to one another even if the α values are quite different. In contrast, a similar thought experiment with the β values calculated by the reduced molecular masses produces a much different initial result. Here, the same calculation suggests that 73%, 83% and 87% of the β_{resp} signals are due to bond breaking processes.

Additionally, these reduced molecular β values tell us something about the molecular preferences of respiration enzymes at play in these samples of Lake Houston waters. For instance, if the enzymatic preference for molecular oxygen is a mass dependent process that preserves Δ_{36} and Δ_{35} values, then $\beta_{36/34, resp}$ should equal 2.000 and $\beta_{35/34, resp}$ should be between 1.499 and 1.529 (Yeung et al., 2012). The measured β_{resp} values from LH1 and LH2 are quite close to these, but may actually be slightly higher. If true, this implies that respiration enzymes have a slightly greater than expected preference for molecules of $^{16}\text{O}^{18}\text{O}$ compared to either $^{18}\text{O}^{18}\text{O}$ or $^{17}\text{O}^{18}\text{O}$.

Conclusion

We favor the interpretation that β_{resp} signals are primarily due to bond breaking processes rather than diffusion processes. Earlier calculations of β_{Eq} and $\beta_{kin, atomic}$ are based on an “atomistic” approach where atomic O is the variable of interest, not molecular O₂. While $\beta_{kin, molecular}$ is a better estimate of molecular transport fractionation (i.e. it is O₂ diffusing into cells, not atomic O), it still emphasizes mass rather than vibrational frequency. However, it is bonds of molecular O₂ that are broken in every respiration mechanism, and our data suggest that bond breaking is the mechanism responsible for the greater part of β_{resp} signals. These first measurements of multiply

substituted isotopologues during an isolated dark respiration process have permitted the first comparison of these measured β_{resp} values to their calculated β_{diff} and β_{BB} end-members.

In the future, modeling respiration and diffusion as a two-step fractionation process, isolating individual respiration mechanisms and conducting respiration experiments from other environments (i.e. marine) will be key to continued testing of hypotheses discussed here.

References

- Angert, A. and Luz, B. (2001) Fractionation of oxygen isotopes by root respiration: Implications for the isotopic composition of atmospheric O₂. *Geochim Cosmochim Acta* 65, 1695-1701.
- Angert, A., Rachmilevitch, S., Barkan, E. and Luz, B. (2003) Effects of photorespiration, the cytochrome pathway, and the alternative pathway on the triple isotopic composition on atmospheric O₂. *Global Biogeochemical Cycles* 17, 1030.
- Bao, H., Lyons, J. and Zhou, C. (2008) Triple oxygen isotope evidence for elevated CO₂ levels after a Neoproterozoic glaciation. *Nature* 453, 504-506.
- Barkan, E. and Luz, B. (2005) High precision measurements of ¹⁷O/¹⁶O and ¹⁸O/¹⁶O ratios in H₂O. *Rapid Communications in Mass Spectrometry* 19, 3737-3742.
- Bender, M., Sowers, T. and Labeyrie, L. (1994) The Dole effect and its variations during the last 130,000 years as measured in the Vostok ice core. *Global Biogeochemical Cycles* 8, 363-376.
- Blunier, T., Barnett, B., Bender, M.L. and Hendricks, M.B. (2002) Biological oxygen productivity during the last 60,000 years from triple oxygen isotope measurements. *Global Biogeochemical Cycles* 16, 1029.
- Blunier, T., Bender, M.L., Barnett, B. and von Fischer, J.C. (2012) Planetary fertility during the past 400 ka based on the triple isotope composition of O₂ in trapped gases from the Vostok ice core. *Climate of the Past* 8, 1509-1526.
- Craig, H. (1961) Isotopic variations in meteoric waters. *Science* 133, 1702-1703.
- Degens, E., Guillard, R., Sackett, W. and Hellebust, J. (1968) Metabolic fractionation of carbon isotopes in marine plankton—I. Temperature and respiration experiments, *Deep Sea Research and Oceanographic Abstracts*. Elsevier, pp. 1-9.
- Dole, M. (1935) The relative atomic weight of oxygen in water and air. *Journal of the American Chemical Society* 57, 273.
- Dole, M., Hawkins, R.C. and Barker, H.A. (1947) Bacterial Fractionation of Oxygen Isotopes. *Journal of the American Chemical Society* 69, 226-228.
- Dole, M. and Jenks, G. (1944) Isotopic composition of photosynthetic oxygen. *Science* (Washington, D. C., 1883-) 100, 409.
- Dole, M. and Lane, G. (1954) Fractionation of Oxygen Isotopes during the Formation of Metal Oxide Films. *The Journal of Chemical Physics* 22, 949-950.
- Dongmann, G., Nürnberg, H., Förstel, H. and Wagener, K. (1974) On the enrichment of H₂¹⁸O in the leaves of transpiring plants. *Radiat Environ Bioph* 11, 41-52.

- Eisenstadt, D., Barkan, E., Luz, B. and Kaplan, A. (2010) Enrichment of oxygen heavy isotopes during photosynthesis in phytoplankton. *Photosynthesis Research* 103, 97-103.
- Epstein, S. and Zeiri, L. (1988) Oxygen and Carbon Isotopic Compositions of Gases Respired by Humans. *P Natl Acad Sci USA* 85, 1727-1731.
- Farquhar, G.D., Lloyd, J., Taylor, J.A., Flanagan, L.B., Syvertsen, J.P., Hubick, K.T., Wong, S.C. and Ehleringer, J.R. (1993) Vegetation effects on the isotope composition of oxygen in atmospheric CO₂. *Nature (London)* 363, 439-443.
- Garcia, H.E. and Gordon, L.I. (1992) Oxygen solubility in seawater: Better fitting equations. *Limnol Oceanogr* 37, 1307-1312.
- Guy, R.D., Berry, J.A., Fogel, M.L. and Hoering, T.C. (1989) Differential fractionation of oxygen isotopes by cyanide-resistant and cyanide-sensitive respiration in plants. *Planta* 177, 483-491.
- Guy, R.D., Fogel, M.L. and Berry, J.A. (1993) Photosynthetic Fractionation of the Stable Isotopes of Oxygen and Carbon. *Plant Physiology* 101, 37-47.
- Hamme, R.C. and Emerson, S.R. (2004) The solubility of neon, nitrogen and argon in distilled water and seawater. *Deep Sea Research Part I: Oceanographic Research Papers* 51, 1517-1528.
- Helman, Y., Barkan, E., Eisenstadt, D., Luz, B. and Kaplan, A. (2005) Fractionation of the Three Stable Oxygen Isotopes by Oxygen-Producing and Oxygen-Consuming Reactions in Photosynthetic Organisms. *Plant Physiology* 138, 2292-2298.
- Hendricks, M.B., Bender, M.L., Barnett, B.A., Strutton, P. and Chavez, F.P. (2005) Triple oxygen isotope composition of dissolved O₂ in the equatorial Pacific: A tracer of mixing, production, and respiration. *Journal of Geophysical Research* 110, C12021.
- Hu, H., Yeung, L.Y., Ash, J.L., Li, S. and Li, B. (2017) High precision measurements of ¹⁸O¹⁸O and ¹⁷O¹⁸O in tropospheric O₂ and their significance to oceanography. In preparation.
- Hulston, J.R. and Thode, H.G. (1965) Variations in the S³³, S³⁴, and S³⁶ Contents of Meteorites and Their Relation to Chemical and Nuclear Effects. *Journal of Geophysical Research* 70, 3475-3484.
- Huntington, K.W., Eiler, J.M., Affek, H.P., Guo, W., Bonifacie, M., Yeung, L.Y., Thiagarajan, N., Passey, B., Tripathi, A., Daëron, M. and Came, R. (2009) Methods and limitations of 'clumped' CO₂ isotope (Δ₄₇) analysis by gas-source isotope ratio mass spectrometry. *Journal of Mass Spectrometry* 44, 1318-1329.
- Kamen, M.D. and Barker, H.A. (1945) Inadequacies in Present Knowledge of the Relation between Photosynthesis and the O¹⁸ Content of Atmospheric Oxygen. *P Natl Acad Sci USA* 31, 8-15.

- Kiddon, J., Bender, M.L., Orchardo, J., Caron, D.A., Goldman, J.C. and Dennett, M. (1993) Isotopic fractionation of oxygen by respiring marine organisms. *Global Biogeochemical Cycles* 7, 679-694.
- Kroopnick, P. and Craig, H. (1972) Atmospheric Oxygen: Isotopic Composition and Solubility Fractionation. *Science* (Washington, D. C., 1883-) 175, 54-55.
- Landais, A., Dreyfus, G., Capron, E., Masson-Delmotte, V., Sanchez-Goni, M.F., Desprat, S., Hoffmann, G., Jouzel, J., Leuenberger, M. and Johnsen, S. (2010) What drives the millennial and orbital variations of $\delta^{18}\text{O}_{\text{atm}}$? *Quaternary Science Reviews* 29, 235-246.
- Lane, G.A. and Dole, M. (1956) Fractionation of oxygen isotopes during respiration. *Science* (Washington, D. C., 1883-) 123, 574-576.
- Luz, B. and Barkan, E. (2000) Assessment of Oceanic Productivity with the Triple-Isotope Composition of Dissolved Oxygen. *Science* (Washington, D. C., 1883-) 288, 2028-2031.
- Luz, B. and Barkan, E. (2005) The isotopic ratios $^{17}\text{O}/^{16}\text{O}$ and $^{18}\text{O}/^{16}\text{O}$ in molecular oxygen and their significance in biogeochemistry. *Geochim Cosmochim Acta* 69, 1099-1110.
- Luz, B., Barkan, E., Bender, M.L., Thiemens, M.H. and Boering, K.A. (1999) Triple-isotope composition of atmospheric oxygen as a tracer of biosphere productivity. *Nature* (London) 400, 547-550.
- Metzner, H. (1975) Water decomposition in photosynthesis? A critical reconsideration. *Journal of theoretical biology* 51, 201-231.
- Metzner, H., Fischer, K. and Bazlen, O. (1979) Isotope ratios in photosynthetic oxygen. *Biochimica et Biophysica Acta (BBA)-Bioenergetics* 548, 287-295.
- Pack, A., Toulouse, C. and Przybilla, R. (2007) Determination of oxygen triple isotope ratios of silicates without cryogenic separation of NF_3 —technique with application to analyses of technical O_2 gas and meteorite classification. *Rapid Communications in Mass Spectrometry* 21, 3721-3728.
- Prokopenko, M.G., Pauluis, O.M., Granger, J. and Yeung, L.Y. (2011) Exact evaluation of gross photosynthetic production from the oxygen triple-isotope composition of O_2 : Implications for the net-to-gross primary production ratios. *Geophys Res Lett* 38, L14603.
- Rakestraw, N.M., Rudd, D.P. and Dole, M. (1951) Isotopic composition of oxygen in air dissolved in Pacific Ocean water as a function of depth. *Journal of the American Chemical Society* 73, 2976-2976.
- Roake, W. and Dole, M. (1950) Oxygen isotope exchange in the electric discharge. *Journal of the American Chemical Society* 72, 36-40.
- Ruben, S., Randall, M., Kamen, M. and Hyde, J.L. (1941) Heavy Oxygen (O^{18}) as a Tracer in the Study of Photosynthesis. *Journal of the American Chemical Society* 63, 877-879.

Schleser, G.H. (1979) Oxygen Isotope Fractionation during Respiration for Different Temperatures of *T-Utilis* and *Escherichia-Coli-K12*. *Radiat Environ Bioph* 17, 85-93.

Stevens, C.L.R., Schultz, D., Van Baalen, C. and Parker, P.L. (1975) Oxygen isotope fractionation during photosynthesis in a blue-green and green alga. *Plant Physiology* 56, 126-129.

Thiemens, M.H. and Heidenreich, J.E. (1983) The Mass-Independent Fractionation of Oxygen: A Novel Isotope Effect and its Possible Cosmochemical Implications. *Science (Washington, D. C., 1883-)* 219, 1073-1075.

Thiemens, M.H., Jackson, T., Zipf, E.C., Erdman, P.W. and van Egmond, C. (1995) Carbon Dioxide and Oxygen Isotope Anomalies in the Mesosphere and Stratosphere. *Science (Washington, D. C., 1883-)* 270, 969-972.

Vinogradov, A.P., Kuturina, V.M., Ulubekova, M.B. and Zadorozhnyi, I.K. (1960) Isotopic Composition of Oxygen in Photosynthesis and Respiration. *Dokl Akad Nauk Sssr* 134, 1486-1489.

Wang, Z.G., Schauble, E.A. and Eiler, J.M. (2004) Equilibrium thermodynamics of multiply substituted isotopologues of molecular gases. *Geochim Cosmochim Acta* 68, 4779-4797.

Yeung, L.Y., Ash, J.L. and Young, E.D. (2014) Rapid photochemical equilibration of isotope bond ordering in O₂. *Journal of Geophysical Research* 119, 10,552-10566.

Yeung, L.Y., Murray, L.T., Ash, J.L., Young, E.D., Boering, K.A., Atlas, E.L., Schauffler, S.M., Lueb, R.A., Langenfelds, R.L. and Krummel, P. (2016) Isotopic ordering in atmospheric O₂ as a tracer of ozone photochemistry and the tropical atmosphere. *Journal of Geophysical Research: Atmospheres* 121.

Yeung, L.Y., Young, E.D. and Schauble, E.A. (2012) Measurements of ¹⁸O¹⁸O and ¹⁷O¹⁸O in the atmosphere and the influence of isotope-exchange reactions. *Journal of Geophysical Research* 117, D18306.

Young, E.D., Galy, A. and Nagahara, H. (2002) Kinetic and equilibrium mass-dependent isotope fractionation laws in nature and their geochemical and cosmochemical significance. *Geochim Cosmochim Acta* 66, 1095-1104.

Young, E.D., Yeung, L.Y. and Kohl, I.E. (2014) On the $\Delta^{17}\text{O}$ Budget of Atmospheric O₂. *Geochim Cosmochim Acta* 135, 102-125.

Yung, Y.L., DeMore, W.B. and Pinto, J.P. (1991) Isotopic Exchange Between Carbon Dioxide and Ozone via O(¹D) in the Stratosphere. *Geophys Res Lett* 18, 13-16.

Chapter 3: Biological signatures in clumped isotopes of O₂

A version of this chapter has been previously published as Yeung, L.Y.,* & Ash, J.L.,* and Young, E.D. “Biological signatures in clumped isotopes of O₂,” *Science*, 348 (6233), 431-434. 2015. *denotes equal contributions

Abstract

The abundances of molecules containing more than one rare isotope have been applied broadly to determine formation temperatures of natural materials. These applications of “clumped” isotopes rely on the assumption that isotope-exchange equilibrium is reached, or at least approached, during the formation of these materials. In a closed-system terrarium experiment, we demonstrate that biological oxygen (O₂) cycling drives the clumped-isotope composition of O₂ away from isotopic equilibrium. Our model of the system suggests that unique biological signatures are present in clumped isotopes of O₂ – and not formation temperatures. Photosynthetic O₂ is depleted in ¹⁸O¹⁸O and ¹⁷O¹⁸O relative to a stochastic distribution of isotopes, unlike at equilibrium, where heavy-isotope pairs are enriched. Similar signatures may be widespread in nature, offering new tracers of biological and geochemical cycling.

Statistical thermodynamics predicts that heavy isotopes will be bound together in a molecule more often than predicted by chance alone, provided the system is at isotopic equilibrium (Richet et al., 1977; Wang et al., 2004). This preference for heavy-isotope pairing and its variation with temperature forms the basis of clumped-isotope thermometry (Ghosh et al., 2006; Stolper et al., 2014a; Yeung et al., 2014), a class of approaches based on precise measurements of molecules containing more than one rare isotope. When isotope-exchange reactions facilitate the equilibration of heavy-isotope

pairs, the resulting isotopic distribution has indeed been shown to achieve equilibrium across a wide range of temperatures (Affek, 2013; Passey and Henkes, 2012; Stolper et al., 2014b; Yeung et al., 2014); however, isotopic equilibrium is the exception rather than the rule in nature. Biogenic substances for example, are often formed through irreversible enzymatic reactions for which isotope-exchange equilibrium cannot be expected a priori. Yet, many natural materials with kinetically constrained and/or biological origins (e.g. carbonate shells) show only minor departures from equilibrium isotope fractionation (Affek and Zaarur, 2014; Guo et al., 2009; Tang et al., 2014). Large biological and physical effects on heavy-isotope pairing could complicate the interpretation of emerging clumped-isotope thermometers in methane, O₂, and other candidate systems (Ono et al., 2014; Stolper et al., 2014a; Yeung et al., 2014).

Here we consider photosynthetic O₂ formation from water at the oxygen-evolving complex of Photosystem II (OEC). In the OEC, O-O bond formation occurs at the end of a five-step light-dependent sequence (Figure 3.1). This reaction most likely does not equilibrate O-O isotope pairs given the lack of isotopic equilibration between water and the O₂ produced (Guy et al., 1993; Helman et al., 2005; Stevens et al., 1975; Urey and Grieff, 1935). We argue that the tendency for two heavy oxygen isotopes to be bound together during oxygenic photosynthesis reflects primarily the isotopic preferences of water molecules binding to the OEC. These patterns of heavy-isotope pairing should be apparent in clumped isotopes of O₂. Measurements of the ¹⁸O¹⁸O (mass 36) and ¹⁷O¹⁸O (mass 35) isotopologues of O₂, together with bulk isotope ratios (¹⁸O/¹⁶O and ¹⁷O/¹⁶O) characterize

the number of heavy-isotope pairs in a sample relative to the number expected by chance alone (i.e., the stochastic distribution). These deviations are quantified as Δ_{36} and Δ_{35} values: Excesses of $^{18}\text{O}^{18}\text{O}$ and $^{17}\text{O}^{18}\text{O}$ relative to the stochastic distribution of isotopes in the sample results in $\Delta_{36} > 0$ and $\Delta_{35} > 0$ respectively. A deficit in $^{18}\text{O}^{18}\text{O}$ and $^{17}\text{O}^{18}\text{O}$ results in $\Delta_{36} < 0$ and $\Delta_{35} < 0$.

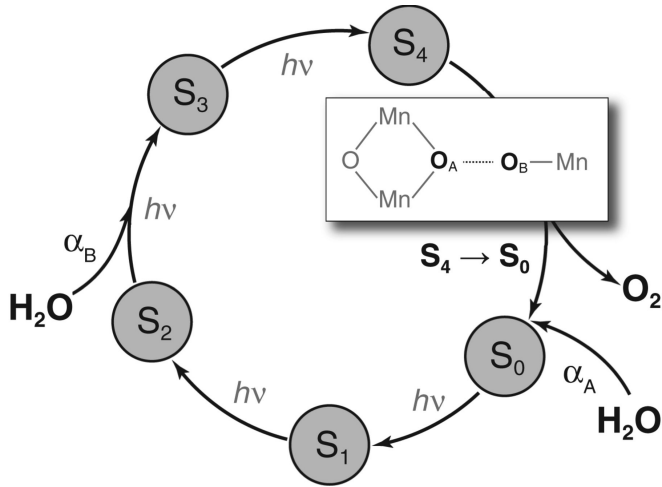


Figure 3.1: The five-step Kok cycle for the water-splitting reaction $2\text{H}_2\text{O} + 4h\nu \rightarrow \text{O}_2 + 4\text{H}^+ + 4\text{e}^-$ is shown without electron flow (Kok et al., 1970). Transitions between intermediate oxidation states of the OEC (S_0 to S_4) occur upon absorption of visible light. The water-binding sequence is based on experimental results (Cox et al., 2014; Noguchi, 2008; Rapatskiy et al., 2012), which also indicate that water substrates are exchangeable at least up to state S_3 on chemically

distinct binding sites (Hillier and Wydrzynski, 2008; Rapatskiy et al., 2012). The O–O bond is formed during the S_4 -to- S_0 transition, expressing the isotopic fractionations α_A and α_B from water substrate binding.

The Δ_{36} and Δ_{35} signatures of oxygenic photosynthesis can thus be estimated by assigning each water-binding site its own isotopic fractionation factor $\alpha = {}^{18}R_{\text{bound}}/{}^{18}R_{\text{water}}$ where ${}^{18}R$ is the ratio of ^{18}O to ^{16}O atoms in each reservoir. At natural isotopic abundances, the bulk isotopic composition of photosynthetic O_2 is the weighted sum of those contributions – i.e., ${}^{18}R_p \approx \frac{1}{2}[({}^{18}R_{\text{water}} \times \alpha_A) + ({}^{18}R_{\text{water}} \times \alpha_B)]$ with binding sites A and B each contributing one of the two oxygen atoms in each O_2 molecule. The probability of generating ^{18}O - ^{18}O bonds is therefore ${}^{36}R_p = ({}^{18}R_{\text{water}} \times \alpha_A) ({}^{18}R_{\text{water}} \times \alpha_B)$. The stochastic

distribution of ^{18}O atoms is calculated from the bulk $^{18}\text{O}/^{16}\text{O}$ ratio as ${}^{36}R_{\text{stochastic}} = ({}^{18}R_p)^2$.

The expression for $\Delta_{36,p}$ then reduces to

$$\Delta_{36,p} = \left[\frac{\alpha_A \alpha_B}{\frac{1}{4}(\alpha_A + \alpha_B)^2} - 1 \right] \quad (3.1)$$

See the supplementary text for details. Equation 3.1 reveals that, in all cases, $\Delta_{36,p} \leq 0$; contrary to the enhanced isotope pairing that would be expected at isotopic equilibrium, there is an apparent aversion to heavy-isotope pairing associated with photosynthetic O_2 production. If the isotopic preferences at each water-binding site are equal ($\alpha_A = \alpha_B$), then $\Delta_{36,p} = 0$. If the binding sites are not equivalent ($\alpha_A \neq \alpha_B$) as isotope labeling studies indicate (Hillier and Wydrzynski, 2008; Rapatskiy et al., 2012), then $0 \geq \Delta_{36,p} > -0.9$ per mil (‰) for plausible α -values between 0.97 and 1.03 (Angeles-Boza et al., 2014; Angeles-Boza and Roth, 2012). A similar expression can be derived for $\Delta_{35,p}$ values, which are predicted to be about half those of $\Delta_{36,p}$ (see the supplementary text). These values cannot be interpreted as formation temperatures because all equilibrated samples have $\Delta_n \geq 0$ (Wang et al., 2004). Photosynthesis should therefore impart a distinct non-equilibrium clumped isotope signature on O_2 .

We conducted a closed-system terrarium experiment with six water hyacinths (*Eichhorniae crassipes*) to explore the effects of biological oxygen cycling on five isotopologues of O_2 (see supplementary text). The terrarium was illuminated with fluorescent lights on a 12-hour/12-hour light-dark cycle. Headspace samples were purified and analyzed over a 1-year period for both the bulk and clumped isotopic composition of O_2 . We found that biological oxygen cycling altered isotopic ordering in

the headspace O₂, yielding apparent steady-state Δ_{36} and Δ_{35} values that are inconsistent with O₂ formation temperatures and more consistent with the predicted photosynthetic endmembers (Figure 3.2 and Table S3.3).

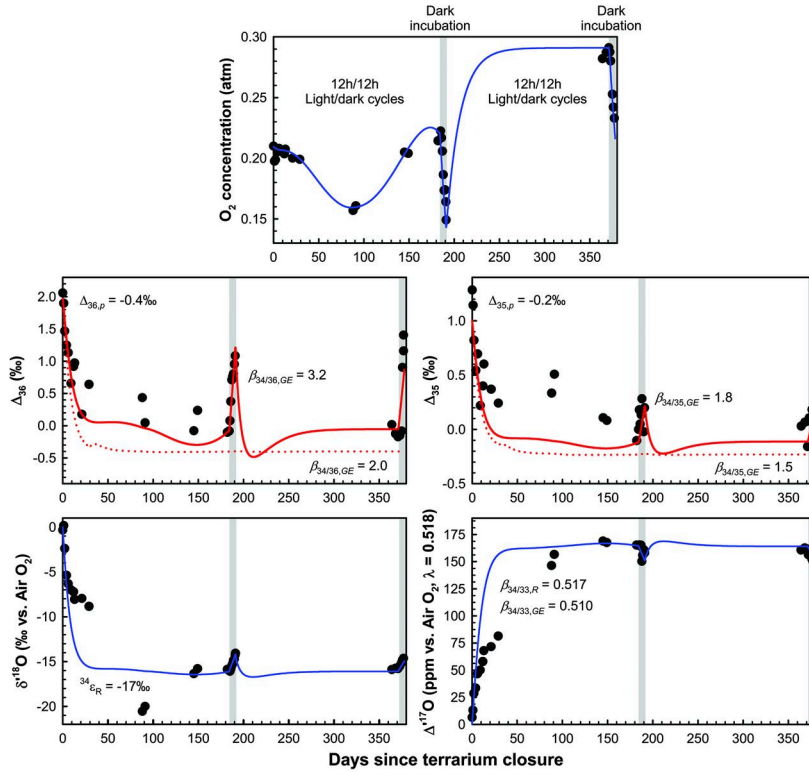


Figure 3.2: Evolution of concentration and O₂ isotopologue composition in the terrarium. Observations (data points) are compared with model results (curves). Uncertainties are not shown for clarity, but long-term analytical uncertainties in O₂ concentration, $\delta^{18}\text{O}$, $\Delta^{17}\text{O}$, Δ_{36} , and Δ_{35} are 1%, 0.04‰, 5 ppm, 0.17‰, and 0.3‰, respectively. A single isotopologue discrimination factor ($^{34}\epsilon_R = -17\text{‰}$) is used here to illustrate steady-state behavior in

$\delta^{18}\text{O}$ and $\Delta^{17}\text{O}$; a more detailed model run yields better agreement for $\delta^{18}\text{O}$ and $\Delta^{17}\text{O}$ but similar results for Δ_{36} and Δ_{35} . Mass-dependent exponents used in the model, $\beta_{34/n}$, are labeled, with subscripts *R* and *GE* denoting values for respiration and gas exchange, respectively. For $\beta_{34/35,GE}$ and $\beta_{34/36,GE}$, two model runs are shown to illustrate their effects on the Δ_{36} and Δ_{35} time traces (see supplementary text).

The Δ_{36} and Δ_{35} values of O₂ were driven down from atmospheric values [2‰ and 1‰, respectively (Yeung et al., 2014)] and down past equilibrium values at 25°C (1.5‰ and 0.8‰, respectively), finally approaching an apparent isotopic steady state at the stochastic distribution of isotopes ($\Delta_{36} = -0.01 \pm 0.08\text{‰}$ and $\Delta_{35} = 0.0 \pm 0.1\text{‰}$; 1 SEM, $n = 4$). The plant community shifted to an algae-dominated ecosystem during the first 6

months, altering the isotopic, chemical and physical properties of the terrarium (Figure S3.1). However, the clumped-isotope composition of the headspace O₂ evolved steadily toward its apparent steady state, similar to the evolution of the oxygen triple-isotope composition. Stead-state $\Delta^{17}\text{O}$ values were 165 parts per million (ppm), consistent with those reported in similar experiments (Angert et al., 2003; Luz et al., 1999).

Dark incubations of the terrarium, which consumed up to 35% of the headspace O₂, caused Δ_{36} values to increase linearly with time up to ~1‰ (Figure 3.2). The Δ_{35} values, in contrast, remained generally constant (means of $\Delta_{35} = 0.1 \pm 0.1\text{‰}$ and $0.1 \pm 0.05\text{‰}$; 1SD). Returning to the light-dark cycles restored the clumped-isotope composition to its apparent steady-state value after 6 months ($\Delta_{36} = -0.09 \pm 0.06\text{‰}$ and $\Delta_{35} = 0.0 \pm 0.1\text{‰}$; 1 SEM, $n = 3$). To test the veracity of these measurements, headspace O₂ samples drawn from both light and dark incubations were photolytically equilibrated at known temperatures (Yeung et al., 2014). The equilibrations yielded Δ_{36} and Δ_{35} values of O₂ consistent with isotope-exchange equilibrium (Table S3.3), suggesting that our observations are unlikely to be analytical artifacts. Atmospheric O₂ leaking into the terrarium would increase $\delta^{18}\text{O}$ far too rapidly relative to Δ_{36} to explain these observations. The observed clumped-isotope variations therefore most likely arise from biological and physical processes inside the terrarium.

We constructed a two-reservoir model of O₂ (i.e., in headspace and water) in the terrarium that accounts for photosynthetic O₂ formation, fractionation of O₂ due to respiration and air-water gas exchange (see supplementary materials). We included

kinetic isotope fractionation for gas transfer into and out of solution [$^{34}\alpha_{GE,kinetic} = 0.9972$ for $^{18}\text{O}/^{16}\text{O}$ (Knox et al., 1992)]. The model was run with a range of plausible isotope fractionation factors for respiration [$^{34}\alpha_R = 0.97\text{-}0.99$ (Cheah et al., 2014; Luz and Barkan, 2005)] and gas exchange rates (Knox et al., 1992; Tempest and Emerson, 2013) to examine the sensitivity of the terrarium headspace to changes in these quantities. The oxygen triple-isotope composition of the terrarium water was measured and used as the bulk isotopic composition of photosynthetic O_2 (Guy et al., 1993; Helman et al., 2005). No single set of parameters explained all of the isotopic variations at steady state and during dark incubations.

The increase of headspace Δ_{36} and Δ_{35} values in the dark implies that the apparent steady-state values near zero can only be reached if light-dependent processes drive Δ_{36} and Δ_{35} values below zero. Equation 1.1 suggests that photosynthesis could be the relevant mechanism, because the O_2 generated is likely to have $\Delta_{36,p}$ and $\Delta_{35,p}$ values less than zero. To estimate the composition of this source, we note that kinetic and equilibrium isotope effects for relevant photosynthetic fractionations are probably in the range $0.96 > ^{18}\alpha > 1.04$ (Angeles-Boza et al., 2014; Angeles-Boza and Roth, 2012), which we broaden to a more conservative plausible range of $0.9 > ^{18}\alpha > 1.1$. This range of isotope effects gives lower limits on $\Delta_{36,p}$ and $\Delta_{35,p}$ of -10‰ and -5‰ respectively.

If the Δ_{36} increase during dark incubations were solely caused by fractionation in respiration, then large isotope effects in water-enzyme binding would be required: $\Delta_{36,p} < -10\text{‰}$ is needed to achieve steady-state values of Δ_{36} near zero (see supplementary text).

In addition, the associated $\Delta_{35,p} < -5\%$ endmember compositions causes poor agreement between measured and modeled Δ_{35} values (Figure S3.4C). Furthermore, an increase in respiration rates would drive Δ_{36} and Δ_{35} values higher, whereas a decrease in respiration rates would drive the O_2 toward its $\Delta_{36,p}$ and $\Delta_{35,p}$ photosynthetic values (see supplemental text). Therefore, when the O_2 cycle was out of balance in the first 6 months, Δ_{36} would have fluctuated inversely with O_2 concentration (Figure S3.4, B and C). Instead, both Δ_{36} and Δ_{35} decreased nearly monotonically.

Isotopologue fractionation during nonequilibrium O_2 gas exchange could explain the increases of headspace Δ_{36} and Δ_{35} values during dark incubations. The fractionation in headspace $^{16}O^{18}O/^{16}O_2$ is closer to that for gas exchange than that for respiration ($^{34}\alpha_{\text{observed}} = 0.995$ versus $^{34}\alpha_{GE,\text{kinetic}} = 0.9972$ versus $^{34}\alpha_R \sim 0.98$), suggesting that the Δ_{36} and Δ_{35} increases are similarly dominated by gas exchange. Modeling the mass dependence of gas exchange using the dark incubations data yields $\Delta_{36,p}$ and $\Delta_{35,p}$ values within a plausible range (i.e., $\Delta_{36,p} = -0.4\%$, $\Delta_{35,p} = -0.2\%$) (Figure 3.2). The evolution of Δ_{36} and Δ_{35} is also more robust to imbalances in the O_2 cycle (see supplemental text). Other oxygen consumption mechanism such as sulfide oxidation, could impart additional isotopologue signatures (Thurston et al., 2010), so attributing isotopologue discrimination in the dark to a single process is necessarily a simplification. Indeed the implied mass dependence of O_2 consumption in the dark terrarium is unusual, and it merits further investigation (see supplemental text). A detailed understanding of isotopologue fractionation factors will require more controlled experiments of isolated biological and physical properties. Yet, the specific isotopologue discrimination during dark

incubations does not affect the conclusion that photosynthesis generates O₂ with an “anticlumped” isotopologue distribution (i.e., $\Delta_{36} \leq 0$ and $\Delta_{35} \leq 0$). This biological signature in O₂ may be readily observed in the surface ocean, where it could be used to constrain gross primary productivity by exploiting the contrast between biological and atmospheric O₂ clumped-isotope signatures (Juraneck and Quay, 2013). Isotopic ordering in atmospheric O₂ is relatively unaffected by biological O₂ cycling because photochemical equilibration of O₂ exceeds rates of biological cycling by at least a factor of 100 (Yeung et al., 2014; Yeung et al., 2012). Using a biological endmember composition of $\Delta_{36} = 0$, we calculate that biological effects on the tropospheric Δ_{36} budget are therefore most likely on the order of 0.01%.

Our observations indicate that variations in the isotopologue abundance of even simple molecules like O₂ capture the chemistry of complex natural systems. Broader application of these techniques could yield insights into the mechanisms of biomolecule synthesis e.g. methanogenesis, nitrogen reduction during denitrification, and molecular hydrogen release during nitrogen fixation (Hoffman et al., 2013). Moreover, because clumped-isotope signatures can depend only on isotope fractionation factors and not on the isotopic composition of substrates, a new class of reservoir-insensitive approaches for tracing biogeochemical cycling could emerge from these molecular-scale insights.

Supplementary Text

Materials and Methods

Isotopic notation: Definitions and mass dependence

Deviations in $^{18}\text{O}/^{16}\text{O}$ and $^{17}\text{O}/^{16}\text{O}$ abundances from the stochastic distribution of isotopes are expressed as Δ_{36} and Δ_{35} values. Mathematically, $\Delta_{36} = [(^{36}R_{\text{measured}}/^{36}R_{\text{stochastic}})-1]$, where $^{36}R_{\text{measured}} = ^{36}\text{O}_2/^{32}\text{O}_2$ and $^{36}R_{\text{stochastic}} = (^{18}\text{O}/^{16}\text{O})^2$. Similarly, $\Delta_{35} = [(^{35}R_{\text{measured}}/^{35}R_{\text{stochastic}})-1]$ where $^{35}R_{\text{measured}} = ^{35}\text{O}_2/^{32}\text{O}_2$ and $^{35}R_{\text{stochastic}} = 2 \times (^{17}\text{O}/^{16}\text{O})(^{18}\text{O}/^{16}\text{O})$. The triple-isotope composition is reported relative to atmospheric O_2 : $\Delta'^{17}\text{O} = \delta'^{17}\text{O} - 0.518 \times \delta'^{18}\text{O}$. It derives from the bulk oxygen isotope composition, i.e., $\delta'^{18}\text{O} = \ln(^{18}R_{\text{measured}}/^{18}R_{\text{air}})$ and $\delta'^{17}\text{O} = \ln(^{17}R_{\text{measured}}/^{17}R_{\text{air}})$. All isotopic data are reported in units of per mil (‰).

To describe mass-dependent isotopic fractionation (MDF), $^{18}\text{O}/^{16}\text{O}$ and $^{17}\text{O}/^{16}\text{O}$ fractionation factors are related by an exponent $\beta_{18/17}$ near 0.52 using the expression $^{17}\alpha = (^{18}\alpha)^{\beta_{18/17}}$ (Thiemens, 2006; Young et al., 2002). This $\beta_{18/17}$ value of ~ 0.5 derives from the fact that the ^{17}O -to- ^{16}O mass difference is about half that for ^{18}O to ^{16}O . Deviations from this relationship can change steady-state values of $\Delta'^{17}\text{O}$ in the terrarium (Angert et al., 2003). A similar formalism has been derived for bond-preserving fractionation of isotopologues (Yeung et al., 2012), and it suggests that O_2 isotopologues are characterized by $^{36}\alpha \approx (^{34}\alpha)^2$, i.e., $\beta_{34/36} \approx 2$, because the $^{36}\text{O}_2$ -to- $^{32}\text{O}_2$ mass difference is twice that between $^{34}\text{O}_2$ and $^{32}\text{O}_2$. Deviations from $\beta_{34/36} \approx 2$ will alter Δ_{36} values as isotopologues are fractionated. Fractionation of $^{35}\text{O}_2$ was predicted to follow the mass-

dependent relationship $^{35}\alpha \approx (^{34}\alpha)^{1.5}$. See the Supplemental Text for a discussion of the range of expected β values for isotopologue fractionation.

Throughout the paper, we use $^{34}\alpha_R$ in places instead of the more common term $^{18}\alpha_R$ to mean the isotopic fractionation factor for $^{16}\text{O}^{18}\text{O}/^{16}\text{O}^{16}\text{O}$, where $^{16}\text{O}^{18}\text{O}$ is understood to include both isotopomers $^{16}\text{O}^{18}\text{O}$ and $^{18}\text{O}^{16}\text{O}$. It is equivalent to within several ppm (the abundance of $^{17}\text{O}^{17}\text{O}$ is vanishingly small) and emphasizes the distinction between isotopologue vs. bulk isotope fractionation. We also use the isotopic discrimination factor $\varepsilon = \alpha - 1$ to characterize isotopic fractionation in units of per mil for both bulk isotopes (e.g., $^{18}\varepsilon$) and isotopologues (e.g., $^{34}\varepsilon$).

Analytical methods

Isotopic analyses of O_2 were performed at UCLA using previously published techniques (Yeung et al., 2012). Samples of headspace O_2 from the terrarium (25 cm^3) were purified using two passes through a gas chromatograph to remove the ^{36}Ar isobar. The remaining isobaric interference was accounted for using an ion correction. Clumped isotope measurements were calibrated against photolytic equilibrations of bond ordering at known temperatures performed concurrently with analytical sessions (Yeung et al., 2014). Due to the complexity of the purification and analytical schemes, the maximum practical throughput was 1 sample, 1 standard per day. Uncertainty in manometric determinations of O_2 concentration is about 1%, whereas external long-term reproducibility of $\delta^{18}\text{O}$, $\Delta^{17}\text{O}$, Δ_{36} , and Δ_{35} measurements are 0.04‰, 5 ppm, 0.17‰, and 0.3‰, respectively [1 S.D.; (Yeung et al., 2014; Young et al., 2014)].

The triple-isotope composition of the terrarium source water was measured at Johns Hopkins University using the CoF3 method (Baker et al., 2002; Barkan and Luz, 2005; Berman et al., 2013) and normalized to the VSMOW-SLAP scale (Schoenemann et al., 2014) using freshly opened breakseals of VSMOW2 and SLAP2. The mean values of six replicate measurements, spread over two analytical sessions, are $\delta^{18}\text{O}_{\text{VSMOW-SLAP}} = -9.251 \pm 0.293\text{‰}$, $\delta^{17}\text{O}_{\text{VSMOW-SLAP}} = -4.826 \pm 0.156\text{‰}$ (95% confidence intervals; $n = 6$). The measured ^{17}O -excess in these waters, defined using the convention for natural waters ($\Delta^{17}\text{O}_{\text{VSMOW},0.528} = \delta^{17}\text{O}_{\text{VSMOW-SLAP}} - 0.528 \cdot \delta^{18}\text{O}_{\text{VSMOW-SLAP}}$), is $\Delta^{17}\text{O}_{\text{VSMOW},0.528} = 59 \pm 3$ ppm (95% confidence interval; $n = 6$). During these same analytical sessions, the USGS45 and USGS47 standards were measured to have $\Delta^{17}\text{O}_{\text{VSMOW},0.528} = 11 \pm 2$ ppm (1 s.e.m.; $n = 3$) and 39 ± 2 ppm (1 s.e.m.; $n = 2$), respectively, in quantitative agreement with $\Delta^{17}\text{O}_{\text{VSMOW},0.528}$ values of 12 ± 1 ppm and 40 ± 1 ppm reported in ref. (Berman et al., 2013).

Terrarium experiment

A 12 liter gas-tight terrarium was enclosed on July 11, 2013 with water and six common water hyacinths (*Eichhorniae crassipes*), each of which had ~6 associated bulbous petioles. A flexible tube and Tedlar gas-sampling bag filled with water were attached to the terrarium to maintain a constant pressure in the headspace, and a stir bar was used to ensure a well-mixed water reservoir. For the first ~200 days, the terrarium experienced 12 hour light/dark cycles under fluorescent lights ($75 \mu\text{E cm}^{-2} \text{s}^{-1}$). Internal temperature was not actively monitored, but it was assumed to be near 25°C on average given that the room temperature was $21^\circ\text{C} - 25^\circ\text{C}$.

A small amount (<5%) of leaf senescence was visible concurrent with initial terrarium closure, and by day 42 we estimate >60% leaf senescence based on visual estimates from leaf area. By day 131, water hyacinths were no longer the dominant biomass within the terrarium.

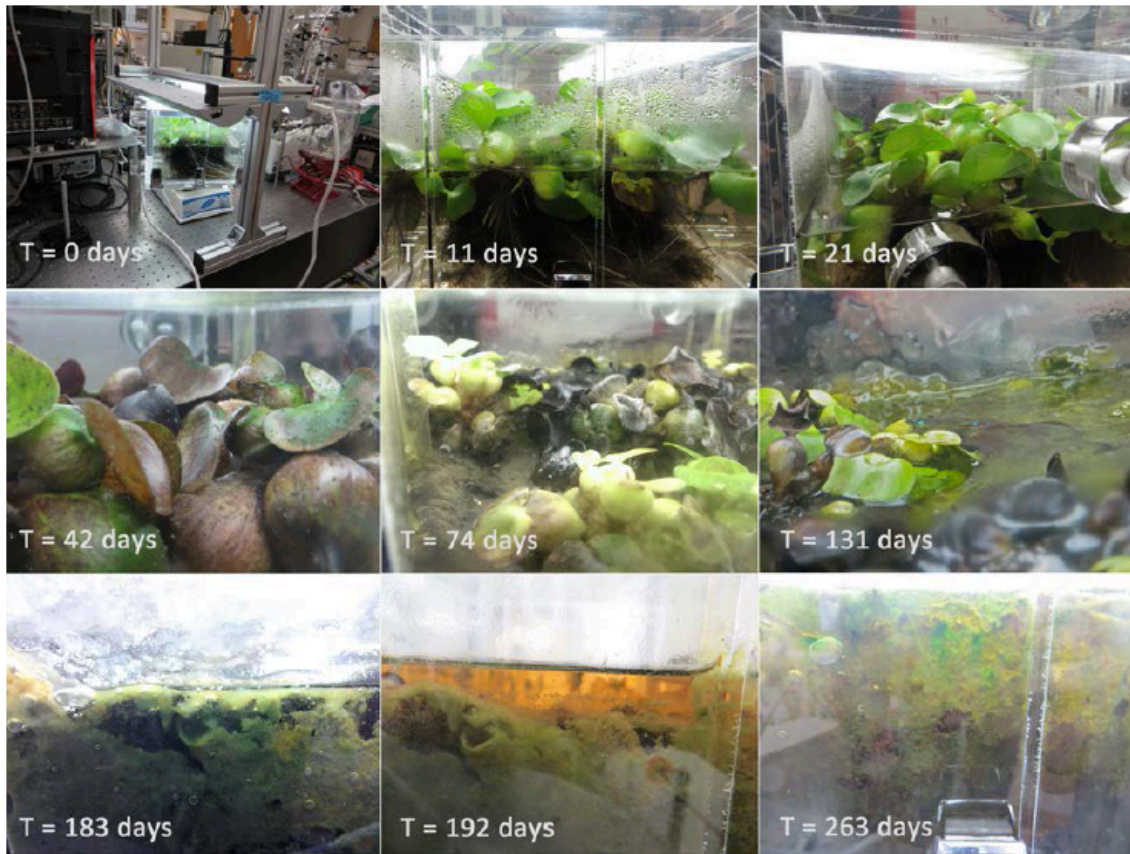


Figure S3.1. Photographs of the terrarium during the experiment. Over the course of a year, the biological community evolved from water hyacinths to an algae-dominated ecosystem.

Freshwater algae and other microorganisms (e.g., unicellular and filamentous cyanobacteria, heterotrophs, etc.) had completely replaced the water hyacinth by day 183 (see Figure S3.1). This biological community shift was reflected in the bulk isotopic composition of the headspace O_2 : $\delta^{18}O$ values evolved in a manner consistent with respiration in leaves being the dominant pathway for O_2 consumption during the first 30

days [$^{18}\epsilon_R \approx -24\text{‰}$; (Cheah et al., 2014)]. The rate of gas exchange between air and water that was required to reproduce the rate of $\delta^{18}\text{O}$ decrease was of order $10\% \text{ h}^{-1}$. Later, as CO_2 concentrations likely plummeted from initial atmospheric values near 400 ppmv, the importance of light-dependent photoprotective O_2 consumption mechanisms such as the glycolate oxidase pathway and the Mehler reaction would have increased. These pathways have smaller ^{18}O discrimination factors and a triple-isotope mass dependence closer to 0.5 [$^{18}\epsilon_R \approx -10\text{‰}$, $\beta_{18/17,R} = 0.5 - 0.51$; (Helman et al., 2005)], which drive $\delta^{18}\text{O}$ values in the headspace closer to that of the source water ($\delta^{18}\text{O}_{\text{air}} = -32.51\text{‰}$). The lowest $\delta^{18}\text{O}$ values measured near day 90 correspond to an overall $^{18}\epsilon_R \approx -12\text{‰}$. Smaller $\beta_{18/17,R}$ values and reduced air-water gas exchange rates would result in a less rapid increase of $\Delta^{17}\text{O}$, as the terrarium steady-state value of $\Delta^{17}\text{O}$ decreases when $\beta_{18/17,R}$ approaches 0.5.

Terrarium model description

The two-box model of the terrarium was constructed based on first-order differential equations for O_2 in the headspace (HS) and dissolved in water (DIS):

$$\frac{d\text{O}_{2,\text{HS}}}{dt} = F_{GE} \quad (\text{S1})$$

$$\frac{d\text{O}_{2,\text{DIS}}}{dt} = F_P - F_R - F_{GE} \quad (\text{S2})$$

where F_{GE} , F_P , and F_R correspond to gross fluxes of O_2 due to gas exchange, photosynthesis, and respiration, respectively. Here, we use the convention of $F_{GE} > 0$ as a net flux into the headspace from the water. For simplicity, F_P is a constant representing

the average effective photosynthetic O₂ flux ($F_P = 0$ during dark incubations). The respiration and gas exchange fluxes are treated as first-order reactions of the dissolved O₂:

$$F_R = k_R \times O_{2,DIS} \quad (S3)$$

$$F_{GE} = k_{GE} \times (O_{2,DIS} - O_{2,SAT}) \quad (S4)$$

First-order kinetics for respiration (i.e., a linear dependence of respiration rate on O₂ concentration) appear empirically valid between 10 – 30% O₂, e.g., (Canvin et al., 1980; Guy et al., 1993), and are conceptually consistent with respiration that is limited by organic matter substrates in a closed system: Changes in net productivity result in a similar change to organic matter (substrate) content. Isotopologues of O₂ were included, yielding a set of linear equations:

$$\tilde{F}_p = F_p \times \tilde{\chi}_{water} \quad (S5)$$

$$\tilde{F}_R = k_R \tilde{\alpha}_R \times \tilde{O}_{2,DIS} \quad (S6)$$

$$\tilde{F}_{GE} = k_{GE} \tilde{\alpha}_{GE,kinetic} \times (\tilde{O}_{2,DIS} - \tilde{\chi}_{HS} \tilde{\alpha}_{GE,equil} \tilde{O}_{2,SAT}) \quad (S7)$$

where χ is the mole fraction, α is the fractionation factor relative to ¹⁶O₂, and the tilde indicates the variables that are isotopologue-dependent; one set of the equations S5 – S7 was used for each O₂ isotopologue. Water was treated as an infinite reservoir of oxygen atoms due to the liquid reservoir having ~6000 times the oxygen in the headspace at closure. For gas exchange, both kinetic and equilibrium (subscript *equil*) fractionation factors were included, using the values ³⁴ $\alpha_{GE,kinetic} = 0.9972$ and ³⁴ $\alpha_{GE,equil} = 1.00073$ at 25°C (Benson and Krause Jr., 1984; Knox et al., 1992). The O₂ concentration in water at

saturation ($O_{2,SAT}$) was calculated using Henry's Law constants and the headspace O_2 partial pressure at each time step.

A value of F_P was estimated from a literature value of net productivity. Under 400 ppmv CO_2 , a water hyacinth is expected to consume $\sim 15 \mu\text{mol } CO_2 \text{ mg Chl}^{-1} \text{ h}^{-1}$ under $75 \mu\text{E m}^{-2} \text{ s}^{-1}$ of light (Spencer and Bowes, 1986). Further assuming $500 \text{ mg Chl m}^{-2}$ of plant leaf (Patterson and Duke, 1979) yields a photosynthetic rate of $7500 \mu\text{mol } CO_2 \text{ m}^{-2} \text{ h}^{-1}$. The terrarium had of order 0.07 m^2 of active leaf area (the cross-sectional area of the box), which results in a net productivity of $525 \mu\text{mol } CO_2 \text{ h}^{-1}$. We then used a photosynthetic quotient of 1.0 – 1.4 and a net-to-gross primary production ratio of 0.5 to obtain an estimate of $1050 - 1470 \mu\text{mol } O_2 \text{ h}^{-1}$ for F_P . With 12 hours of illumination per day, the daily average $F_P = 525 - 735 \mu\text{mol } O_2 \text{ h}^{-1}$ implies a mean turnover time for the headspace of 2 – 3 days ($3.5 \cdot 104 \mu\text{mol } O_2$ initially) before considering the effects of gas exchange. This estimate was used as a guideline for the model. While these calculations are not necessarily valid for the entire experiment, they provide an important order-of-magnitude constraint on likely F_P values inside the terrarium.

Other fixed input parameters include the measured isotopic composition of the terrarium water, the volume of water (8 L), and the volume of the headspace (4 L). The isotopic composition for air was assumed to be $\delta^{18}O = 23.260\text{‰}$, $\delta^{17}O = 11.828\text{‰}$. It is the mean value measured at UCLA between 2011 – 2013 (Young et al., 2014), corrected by -0.080‰ in $\delta^{17}O$ for the difference between water and San Carlos Olivine (Tanaka and Nakamura, 2012). See Tables S3.1 and S3.2 for a summary of model parameters, and the

text below for a discussion of model sensitivity tests and uncertainties.

Terrarium model: Rates of O₂ production, consumption, and gas exchange

The model was run at several levels of complexity to test the robustness of results given the relatively large number of parameters. In general, concentration measurements were modeled first, as they were affected by F_P , k_R , and k_{GE} , but they were unaffected by source isotopic compositions and isotopic fractionation factors. Furthermore, none of these variables affected the isotopic steady state; they only affected the shapes of the time traces as they shifted from one state to another. The k_{GE} value during the first month (0.12 h⁻¹) was highest because the surface area for gas exchange was largest. It decreased over the course of the experiment (eventually to 0.05 h⁻¹) because of leaf senescence, followed by the water developing a visible layer of polymeric substance that likely retarded gas exchange. This later k_{GE} value was derived from dark incubations using the coevolution of concentration and $\delta^{18}\text{O}$ curves: Headspace O₂ consumption was limited by gas exchange into the water, which has a fixed fractionation factor of $^{34}\alpha_{GE,kinetic} = 0.9972$ in these calculations. While no single set of parameters described the entire year's evolution of the terrarium, the data did offer constraints on the sensitivity of Δ_{35} and Δ_{36} . The goal of this modeling exercise was not necessarily to interpret every detail of the time traces quantitatively so much as to gain a general understanding of the role of non-equilibrium gas fluxes and isotopic discrimination factors.

Headspace O₂ concentrations during the initial part of the experiment coincided with changes in biological community. To simplify the task of modeling them, we chose a constant k_R value for the model and fit F_P curves for that k_R value (e.g., Figure S3.2).

Overall, these changes had little direct impact on the modeled time-traces of $\delta^{18}\text{O}$ and $\Delta^{17}\text{O}$; they could affect Δ_{35} and Δ_{36} , depending on the source of non-mass-dependent fractionation (see below). The F_P curve affected the rapidity of the $\delta^{18}\text{O}$ and $\Delta^{17}\text{O}$ time-traces in the first 30 days, but the gas exchange rate could be adjusted to compensate (see below). As k_R was varied over an order of magnitude ($0.1 - 1 \text{ h}^{-1}$), the magnitude of F_P required to fit the O_2 concentration data changed proportionately (i.e., $200 - 2000 \mu\text{mol O}_2 \text{ h}^{-1}$), but the shape of the curve remained constant. This observation is not surprising given that F_P and F_R both determine the dissolved O_2 concentration. There was little change to the bulk-isotope time traces ($\delta^{18}\text{O}$ and $\Delta^{17}\text{O}$) except at the lowest F_P and k_R values, where they primarily altered the curvature of the isotope traces. We found qualitatively good fits in the range of our *a priori* estimates, i.e., $k_R = 0.3 \text{ h}^{-1}$ and $F_P \sim 990 - 1280 \mu\text{mol O}_2 \text{ h}^{-1}$ (averaging $495 - 640 \mu\text{mol O}_2 \text{ h}^{-1}$ per 24h period) which we use as our control run. F_P was set to zero for dark incubations and to $1820 \mu\text{mol O}_2 \text{ h}^{-1}$ ($910 \mu\text{mol O}_2 \text{ h}^{-1}$ per 24h period) at the conclusion of the first dark incubation to drive the O_2 concentration to $\sim 29\%$, as observed in the headspace between days 364 – 371 (Figure S3.2).

The k_R value in the terrarium could have changed over the course of the experiment instead of or alongside F_P values to modulate the O_2 concentration. If so, isotopic traces were only affected during the light-dark cycle periods, primarily by altering the curvature of the initial approach to steady-state. The evolution of the isotopologue composition during dark respiration experiments would not be affected.

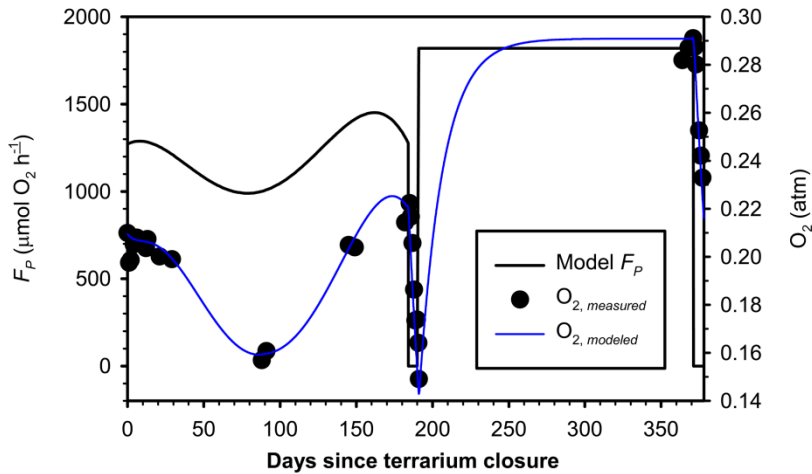


Figure S3.2: Modeled rate of gross photosynthesis, F_p , as a function of time. Using instantaneous F_p variations could also reproduce the data, but they did not alter the qualitative behavior of the model.

The gas exchange rate (k_{GE}) is an important variable that could greatly influence the shape of the time trace of all variables but which does not affect steady-state isotopic values. Because no direct measurements of gas exchange rate were carried out, we tested a range of gas exchange rates at room temperature, $\tau = 5 - 48$ h. We found that gas exchange rates needed to be high during the first month ($\tau \sim 8$ h) to explain the rapidity in changes to $\delta^{18}O$. These high rates were likely due to the high surface area available for gas exchange between the headspace and leaf water. They were decreased ($\tau \sim 20$ h) and kept constant starting at day 90, consistent with leaf senescence decreasing the available surface area for air-water gas exchange. Once the algal population became dominant, the water surface became covered in a viscous, transparent material that resembled transparent extracellular polysaccharides; this surface likely provided a stable, if much slower, gas exchange rate than was available during the first 30 days. The k_{GE} value was adjusted to $\tau \sim 30$ h for the second dark incubation to better fit the O_2 concentration and $\delta^{18}O$ data. This range of k_{GE} values is reasonable given the equilibration timescales measured for O_2 (Knox et al., 1992) and Ar (Tempest and Emerson, 2013) in freshwater

gas-invasion experiments between 10°C – 20°C.

Between days 35 and 184, there was a sizeable decline and rebound of the O₂ concentration that was correlated with a decrease in δ¹⁸O and associated with a shift of the biological community toward an algae-dominated ecosystem. Few measurements were made during this time, so the shape of the isotopic and concentration curves is poorly known. Consequently, we choose not to model F_P and isotope discrimination factors in this part of the time trace in much detail. We used a simple polynomial curve that intersected the measured data points (Figure S3.2). The value of F_P , initially at ~1280 μmol O₂ h⁻¹, needed to decrease to 980 μmol O₂ h⁻¹ by day 90 (lowering the headspace O₂ concentration to 16%) and return to 1280 μmol O₂ h⁻¹ by day 184. Using instantaneous changes in F_P values required slightly larger perturbations (e.g., a decrease to 960 μmol O₂ h⁻¹ by day 90), but it did not change the results qualitatively except to make transitions more abrupt.

Terrarium model: Bulk isotopic discrimination factors

While a single isotopic discrimination factor [$^{34}\epsilon_R = (^{34}\alpha_R - 1) = -17\%$] described the apparent isotopic steady state well (Figure 3.2), the effective discrimination factor needed to change over the course of the year to explain all of the observed variations in δ¹⁸O (Figure S3.3). This observation is not surprising, considering that leaf respiration, aqueous microbial respiration, and light-dependent oxygen consumption have different fractionation factors (Angert et al., 2003; Cheah et al., 2014; Guy et al., 1989; Guy et al., 1993; Helman et al., 2005; Luz and Barkan, 2005). Here, we discuss possible causes for

fluctuating bulk isotopic discrimination values, as well as the reasonableness of the $^{34}\epsilon_R$ and $\beta_{18/17}$ values that explain the observations.

While the hyacinth plants were still green, and no algae was visible to the human eye (the first 30-40 days), leaf respiration likely dominated. The isotopic discrimination factors for water hyacinths have not been measured, but using $^{34}\alpha_R$ value of 0.976 ($^{34}\epsilon_R = -24\text{‰}$), within the range of whole-leaf respiration in other C3 plants (Cheah et al., 2014), yielded a good fit to the first 30 days of $\delta'^{18}\text{O}$ data. A 1‰ greater discrimination (i.e., $^{34}\epsilon_R = -25\text{‰}$) led to modeled $\delta'^{18}\text{O}$ values on day 30 that were 1‰ too high, and vice versa. The k_{GE} value and, to a lesser extent, the F_P value, affected the first ~5 days of the curve, while $^{34}\alpha_R$ determined days 10-30, when the isotopic composition was nearly constant. Therefore, $^{34}\epsilon_R = -24\text{‰}$ is sufficiently accurate to describe the data during the first 30 days. This value of $^{18}\epsilon_R$ suggests that the alternative oxidase pathway of O_2 consumption ($^{34}\epsilon_R \sim -28\text{‰}$) was the most important, as it has a ~10‰ greater discrimination than the cytochrome oxidase pathway ($^{34}\epsilon_R \sim -18\text{‰}$) (Guy et al., 1989; Guy et al., 1993).

From days 30 –184, photoprotective oxygen consumption pathways may have been active, based on the $\delta'^{18}\text{O}$ values measured around day 90; contributions from the Mehler reaction (Helman et al., 2005) could explain the implied $^{34}\epsilon_R$ value of $\sim -12.5\text{‰}$, but light-dependent respiration is believed to be minor in C3 plants (Badger et al., 2000). Discrimination factors as small as $^{34}\epsilon_R \approx -7.7\text{‰}$, however, have been reported for rapidly respiring plants (Guy et al., 1989), so $^{34}\epsilon_R = -12.5\text{‰}$ does not seem unreasonable under low- O_2 conditions. Regardless of its origin, the effective $^{34}\epsilon_R$ clearly changed when O_2

decreased, so the model's $^{34}\epsilon_R$ was increased instantaneously to -12.5‰ from days 30 – 90. A second-order influence of O_2 concentration was apparent on $\delta^{18}O$: Lowering the O_2 concentration to 1/3 its initial value (via a change in F_P) leads to $\delta^{18}O$ being $\sim 3\text{‰}$ too high at day 90, due perhaps to a slower O_2 turnover time.

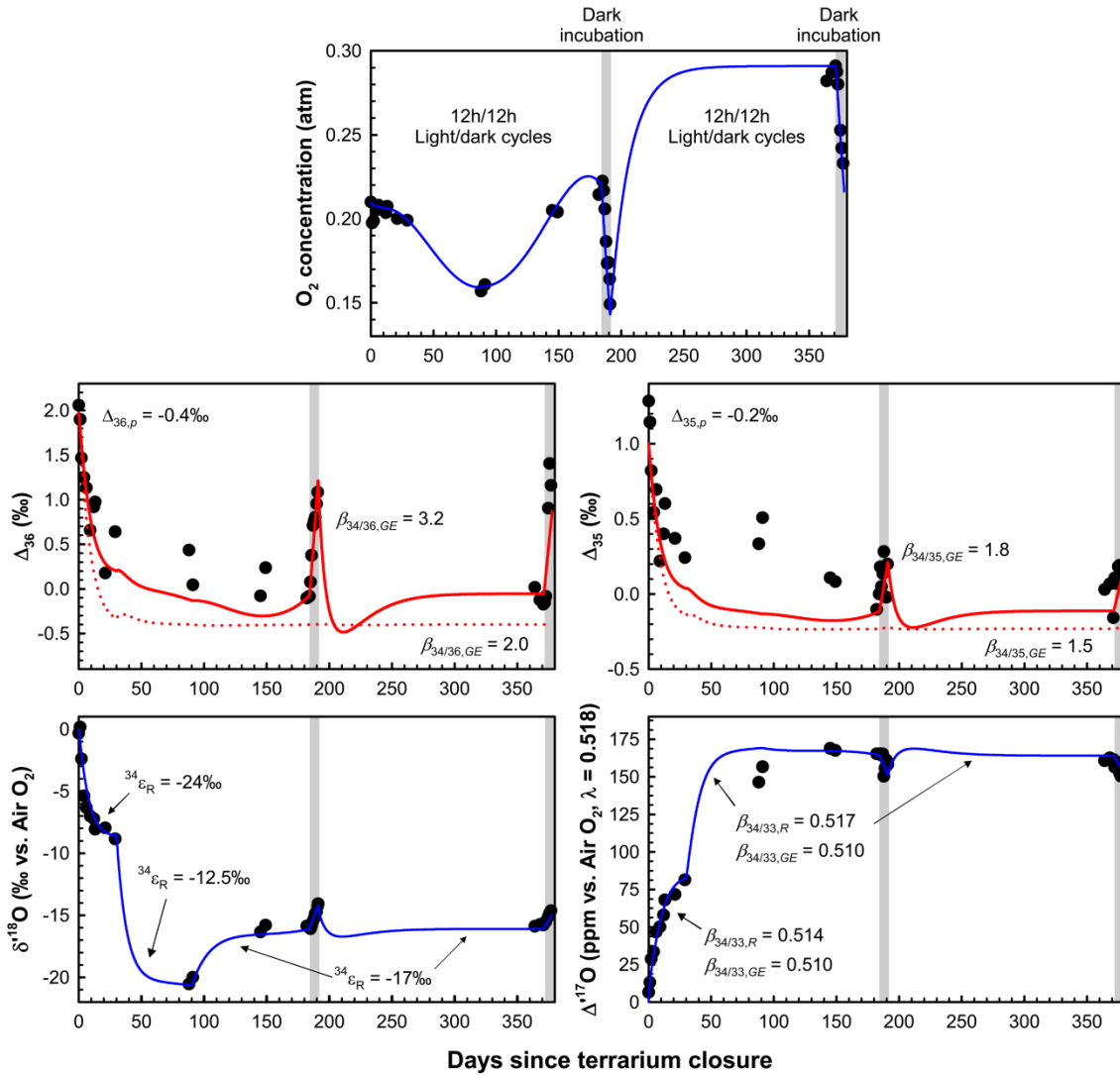


Figure S3.3. Same as Figure 3.1, except the modeled curves include temporal variations in $^{34}\epsilon_R$ and $\beta_{18/17}$ as described in the Materials and Methods. Isotopic steady-state is unaffected by these temporal variations.

At the apparent isotopic steady state, an effective $^{34}\epsilon_R = -17\text{‰}$ is consistent with terrarium studies containing plants and natural bacteria (Angert et al., 2003; Luz and Barkan, 2005). While we could not predict this value *a priori*, it seemed robust, as the terrarium headspace O_2 returned to the apparent steady-state composition after the first dark incubation. Thus, we decreased $^{34}\epsilon_R$ to -17‰ instantaneously after day 90 and left it unchanged for the remainder of the model run shown in Figure S3.3. We note again that the apparent isotopic steady state was independent of the factors directly affecting the O_2 concentration (F_P , k_R , and k_{GE}). The Δ_{35} and Δ_{36} values were sensitive to the evolution of $\delta^{18}\text{O}$ in a second-order way, via the mass-dependent exponents β (see below).

Using $\beta_{34/33,R} = 0.517$ for respiration reproduced the steady-state $\Delta^{17}\text{O}_{\text{air},0.518}$ value of 165 ppm. This value is consistent with previous work [$\beta_{34/33}$ in the model corresponds to θ in papers by Luz & Barkan and Angert et al. (Angert et al., 2003; Luz and Barkan, 2005; Luz et al., 1999)]. Variations in $\beta_{34/33,R}$ of order 0.002 resulted in steady-state values that shifted by 35 ppm, with no discernible effect on Δ_{35} and Δ_{36} values. Despite relatively large uncertainties in the individual $\delta^{18}\text{O}$ and $\delta^{17}\text{O}$ values of water, the uncertainties are correlated, so the triple-isotope composition of the source water is highly precise (see Analytical Methods). The modeled steady-state value of $\Delta^{17}\text{O}_{\text{air},0.518}$ was consequently not sensitive to the absolute $\delta^{18}\text{O}$ and $\delta^{17}\text{O}$ values beyond the ^{17}O -excess uncertainty of 3 ppm. We note that some ambiguity exists in the absolute isotopic difference between VSMOW and air in both its $\delta^{18}\text{O}$ and $\Delta^{17}\text{O}$ values, of order $+0.3\text{‰}$ in $\delta^{18}\text{O}$ and $+0.1\text{‰}$ in $\delta^{17}\text{O}$ (Barkan and Luz, 2005, 2011; Young et al., 2014). These uncertainties broaden the acceptable range of $\beta_{34/33}$ values giving satisfactory fits at steady-state to 0.514 –

0.518. During the first 30 days, increased expression of the alternative oxidase pathway would move $\beta_{34/33}$ values closer to 0.514 (Angert et al., 2003; Helman et al., 2005), a value that described the concurrent $\Delta^{17}\text{O}$ value well (Figure S3.3).

The β values for solubility equilibrium were fixed at mass-dependent values of 0.528, 1.5, and 2 for $\beta_{34/33}$, $\beta_{34/35}$, and $\beta_{34/36}$. See below for a discussion of the β values used for isotopologue fractionation due to respiration and non-equilibrium gas exchange.

Terrarium model: Clumped-isotope discrimination factors

In the model, the evolution of Δ_{35} and Δ_{36} is relatively insensitive to bulk isotopic discrimination factors. Steady state Δ_{35} and Δ_{36} values are primarily sensitive to the balance between the photosynthetic signatures ($\Delta_{35,p}$ and $\Delta_{36,p}$) and the mass-dependent exponents $\beta_{34/35}$ and $\beta_{34/36}$. The dark incubation experiments can only be explained with non-mass-dependent fractionation between O_2 isotopologues (i.e., $\beta_{34/35} \gg 1.5$ and $\beta_{34/36} \gg 2$) during O_2 consumption, but due to the biogeochemical complexity of the terrarium system, this observation requires further experimental studies to verify. We therefore discuss endmember sensitivity tests for Δ_{35} and Δ_{36} that focus on a biological (respiration) or physical (gas exchange) origin of non-MDF effects. Other oxygen-consumption mechanisms could be important e.g., sulfite oxidation, but we will not discuss them here.

Mass-dependent $\beta_{34/36}$ values near 2 could not reproduce the observed enrichments in Δ_{36} during dark incubations. At least one $\beta_{34/36}$ value (e.g., for respiration or gas exchange),

contributing to the overall effective $\beta_{34/36}$ value, must be much larger to explain the observed increase in Δ_{36} (Figure S3.4A). The effective $\beta_{34/36}$ values consistent with the data are all > 2 and most likely in the range of 3 – 5, depending on the rates of respiration and air-water gas exchange. In contrast, variations in Δ_{35} can be modeled with the mass-dependent relationship $^{35}\alpha \approx (^{34}\alpha)^{1.5}$, although we are unable to rule out the possibility of a small non-mass-dependent effect below detection limits. While we cannot explicitly rule out the possibility that the Δ_{36} increase is due to an approach to isotopic equilibrium, the asymmetry in the Δ_{35} and Δ_{36} evolution (Δ_{36} increases while Δ_{35} might not) argues against this interpretation. If O_2 were approaching isotopic equilibrium, one would expect Δ_{35} and Δ_{36} to evolve in concert toward their equilibrium values (0.8‰ and 1.5‰, respectively, at 25°C).

Non-mass-dependent β values that explained the evolution of Δ_{35} and Δ_{36} during dark incubations, hereafter shorthand for $\beta_{34/35} \gg 1.5$ and $\beta_{34/36} \gg 2$, lead to three types of changes to model Δ_{35} and Δ_{36} time traces in the light. First, steady-state values increase. Assigning the non-mass dependence to respiration causes steady-state model values to increase about 10 – 100 times more than when non-mass-dependence is assigned to gas exchange, because of a first-order dependence on respiration rate (higher k_R led to higher steady-state offsets). The sensitivity of these offsets to F_P and k_R are also proportionately larger for respiration: Increasing k_R to 1 h^{-1} and F_P to $\sim 4100 \mu\text{mol } O_2 \text{ h}^{-1}$ (initial value) requires $\Delta_{35,p} = -27\text{‰}$ and $\Delta_{36,p} = -50\text{‰}$ if respiration were non-mass-dependent, whereas $\Delta_{35,p}$ and $\Delta_{36,p}$ could remain unchanged at -0.2‰ and -0.4‰ , respectively, if gas exchange were non-mass-dependent. Second, dark incubations produce Δ_{35} and Δ_{36}

increases. Non-mass-dependence in gas exchange had a larger effect on these increases for a given attendant offset in Δ_{35} and Δ_{36} (due to negative $\Delta_{35,p}$ and $\Delta_{36,p}$ values) at steady state. Furthermore, the $\beta_{34/35}$ value required to compensate for the offset in Δ_{35} at steady state results in Δ_{35} increases during dark incubations that are too large compared with the data by about a factor of two.

Third, the shapes of the Δ_{35} and Δ_{36} curves in the first 100 days are different. While non-mass-dependent fractionation in gas exchange causes small variations in Δ_{35} and Δ_{36} between days 30-184, non-mass-dependent fractionation associated with respiration causes variations in Δ_{35} and Δ_{36} that are 10 – 100 times larger. For example, instead of decreasing in the first 30 days, Δ_{35} and Δ_{36} would increase, as shown in Figures. S3.4B and S3.4C: The larger isotopologue discrimination relative to that at steady state (e.g., $^{34}\epsilon_R = -24\text{‰}$ vs. -17‰) led to a proportionately larger non-mass-dependent effect in Δ_{35} and Δ_{36} . This Δ_{35} and Δ_{36} increase in the first 30 days was followed by a similar underestimation of steady-state Δ_{35} and Δ_{36} values between days 30 – 100 because the isotopologue discrimination during that time was less than that at steady-state ($^{34}\epsilon_R = -12.5\text{‰}$ vs. -17‰). This model prediction is the least certain given that the precise shape of the O_2 and isotope progressions is unknown, so we caution the reader not to over-interpret this qualitative observation. For example, setting $^{34}\epsilon_R = -17\text{‰}$ and $\beta_{34/33} = 0.517$ for the entire duration of the terrarium experiment removed those fluctuations while preserving the clumped-isotope excursion during dark-respiration experiments (Figure S3.5). The relative sizes of these fluctuations depend on k_R (greater respiration rates fractionate O_2 isotopologues more) as well as presumed $\beta_{34/36,R}$ values for different

respiration pathways. Assuming that $\beta_{34/36,R}$ values are pathway-independent is a simplification: Pathway-dependent $\beta_{34/36,R}$ values would further complicate the

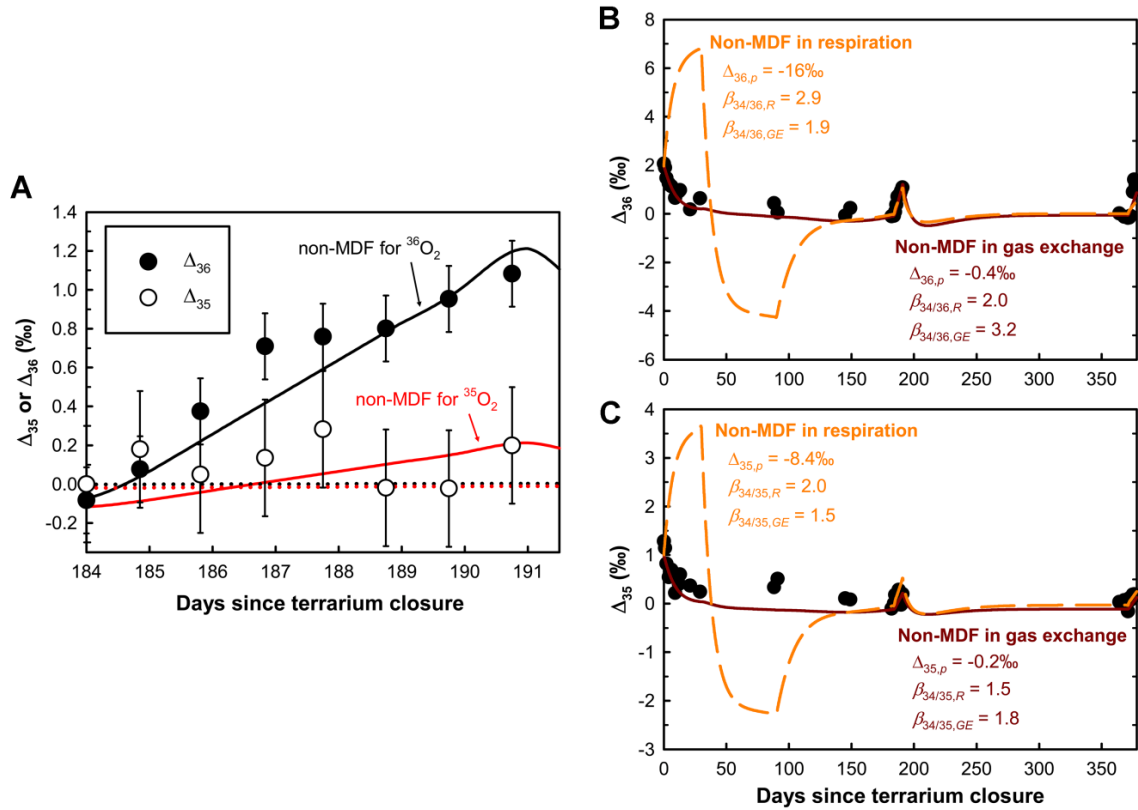


Figure S3.4. Effects of different MDF exponents on Δ_{36} and Δ_{35} values in terrarium headspace O_2 . (A) Dark incubation experiments require non-MDF effects that remain enigmatic. For the purposes of this discussion, we examine the endmember cases of non-MDF effects in respiration and gas exchange. Dotted lines show modeled scenarios in which both respiration and gas exchange exhibit MDF and the observations are not reproduced. (B and C) Non-MDF exponents for respiration cause large fluctuations in Δ_{36} and Δ_{35} values during the first 30 – 90 days that are not observed. They also required implausible values for $\Delta_{36,p}$ and $\Delta_{35,p}$. Non-MDF exponents in gas exchange, however, match the observations better.

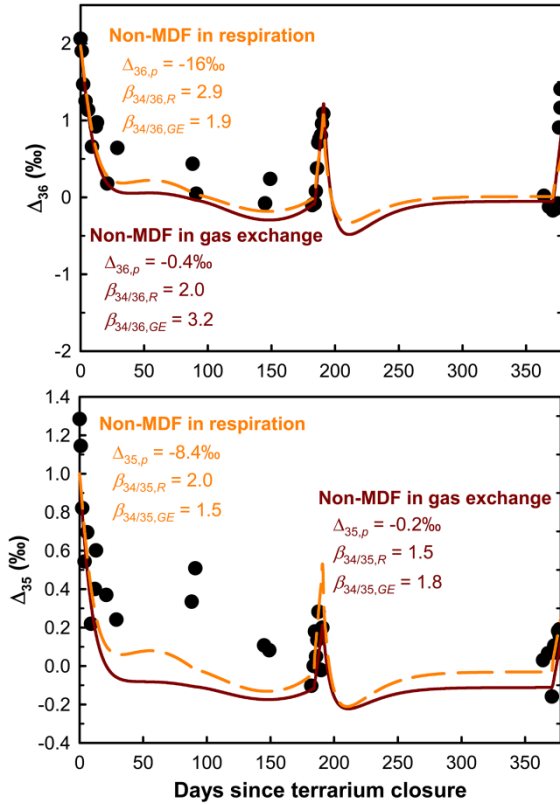


Figure S3.5: Same as Figures S3.4B and S3.4C, except the modeled curves assumed $^{34}\epsilon_R = -17\text{‰}$ and $\beta_{34/33} = 0.517$ throughout.

interpretation of the signals observed in the terrarium, and they could temper the large fluctuations in Δ_{36} and Δ_{35} in the model runs shown in Figures S3.4B and S3.4C.

Uncertainties in the time trace notwithstanding, the data favor a case for non-mass-dependent fractionation in gas exchange more so than in respiration. First, the inferred $\Delta_{35,p}$ and $\Delta_{36,p}$ values are close to the range computed by Equations (1) and (S10) and they are robust against changes in F_P , k_R , O_2 concentration, and β values. Second, both Δ_{35} and Δ_{36} behavior during dark incubations could be reproduced. Further determinations of gas exchange, photosynthesis, and respiration isotopologue signatures in controlled experiments with O_2 will help unravel the origin these enigmatic fractionation effects.

Supplementary text

Expected photosynthetic endmember for $\Delta_{35,p}$

Using the bulk isotopic composition for photosynthetic O₂ of $^{18}R_p = \frac{1}{2} [(^{18}R_{\text{water}} \times ^{18}\alpha_A) + (^{18}R_{\text{water}} \times ^{18}\alpha_B)]$ and $^{17}R_p = \frac{1}{2} [(^{17}R_{\text{water}} \times ^{17}\alpha_A) + (^{17}R_{\text{water}} \times ^{17}\alpha_B)]$, and the stochastic distribution for photosynthetic O₂, $^{35}R_{\text{stochastic}} = 2^{17}R_p^{18}R_p$, we obtain:

$$^{35}R_p = ^{17}R_{\text{water}}^{18}R_{\text{water}} \times \left(^{17}\alpha_A^{18}\alpha_B + ^{17}\alpha_B^{18}\alpha_A \right) \quad (\text{S8})$$

$$^{35}R_{\text{stochastic}} = \frac{1}{2} \left[^{17}R_{\text{water}}^{18}R_{\text{water}} \left(^{17}\alpha_A + ^{17}\alpha_B \right) \left(^{18}\alpha_A + ^{18}\alpha_B \right) \right] \quad (\text{S9})$$

Substituting these values into the expression for $\Delta_{35,p}$ gives:

$$\Delta_{35,p} = \left[\frac{^{17}\alpha_A^{18}\alpha_B + ^{17}\alpha_B^{18}\alpha_A}{\frac{1}{2} \left(^{17}\alpha_A^{18}\alpha_A + ^{17}\alpha_A^{18}\alpha_B + ^{17}\alpha_B^{18}\alpha_A + ^{17}\alpha_B^{18}\alpha_B \right)} - 1 \right] \quad (\text{S10})$$

The relationship between $\Delta_{35,p}$ and $\Delta_{36,p}$ can be derived by using a mass-dependent relationship between $^{18}\alpha$ and $^{17}\alpha$ of $\beta_{18/17} = 0.528$. We note in passing that because minimal $^{18}\text{O}/^{16}\text{O}$ and $^{17}\text{O}/^{16}\text{O}$ fractionation between water and product O₂ is observed in laboratory experiments of photosynthetic O₂ production (Guy et al., 1993; Helman et al., 2005), one can infer that $(\alpha_A - 1) \approx (1 - \alpha_B)$, i.e., any heavy-isotope preference at one H₂O binding site will be matched by an approximately equal aversion at the other site. If this equality were not approximately valid, a fractionation in bulk isotopes would have been observed in previous experiments.

Range of mass dependent β values for O₂ isotopologues

The range of expected mass-dependent β values of O₂ isotopologues, as they relate to the mass-34 isotopologue (¹⁶O¹⁸O) are drawn from the expression

$${}^n\alpha = \left({}^{34}\alpha\right)^{\beta_{34/n}} \quad (\text{S11})$$

where n is the cardinal mass of the other isotopologue (e.g., 35 or 36). We derive the range of reasonable $\beta_{34/n}$ values based on the limiting cases put forth in Ref. (Young et al., 2002). In the gas-kinetic limit, in which isotopologues fractionate only according to their mass, α values are determined by Graham's law, i.e., ${}^n\alpha = (m_{32}/m_n)^{1/2}$. In that limit, $\beta_{34/35} = 1.48$ and $\beta_{34/36} = 1.94$. In a closed system subject to Rayleigh fractionation, these values become $\beta_{35/34} = 1.47$ and $\beta_{34/36} = 1.92$. These $\beta_{34/n}$ values result in <1‰ decreases in Δ_{35} and Δ_{36} in the residue O₂ for ~50% gas-kinetic-limited O₂ consumption (Yeung et al., 2012). At equilibrium, $\beta_{34/n} = (m_{32-1} - m_{34-1})/(m_{32-1} - m_{n-1})$, resulting in $\beta_{34/35} = 1.46$ and $\beta_{34/36} = 1.89$. These result in a range of $\beta_{34/35} = 1.46 - 1.48$ and $\beta_{34/36} = 1.89 - 1.94$ for partitioning by molecular mass. The same calculations can be performed using O₂ reduced masses to simulate partitioning based on vibrational zero-point energies; they show a range of $\beta_{34/35} = 1.47 - 1.55$ and $\beta_{34/36} = 1.89 - 2.06$.

Therefore, we infer that reasonable mass-dependent β values for O₂ isotopologues are $\beta_{34/35} = 1.47 - 1.55$ and $\beta_{34/36} = 1.89 - 2.06$. In contrast, the β values for respiration or gas exchange required to explain the anomalous Δ_{36} enrichments during dark incubations were $\beta_{34/36} > 2.5$ (see “Terrarium model: Clumped-isotope discrimination factors” in Materials and Methods). Accompanying values of $\beta_{34/35}$ could also be anomalous, as the data cannot rule out values as high as $\beta_{34/35} \sim 2$.

Table S3.1: Description of model parameters used in Figures 3.2, S3.2, S3.3, S3.4 and S3.5

Parameter	Description	Value	Notes
$O_{2,DIS}$	Concentration of dissolved O_2	--	Modeled
F_P	Rate of gross photosynthesis	$960 - 1820 \mu\text{mol } O_2 \text{ h}^{-1}$	Variable
F_R	Rate of respiration	$k_R \times O_{2,DIS}$	
F_{GE}	Rate of gas exchange	$k_{GE} \times (O_{2,DIS} - O_{2,SAT})$	
k_R	First-order respiration rate coefficient	0.3 h^{-1}	
k_{GE}	First-order gas-exchange rate coefficient	0.125 h^{-1}	Days 1 – 30
		0.040 h^{-1}	Days 30 – 371
		0.033 h^{-1}	Days 371 – 378
$O_{2,SAT}$	Dissolved O_2 at saturation equilibrium	$P_{O_2} \times K_H$	O_2 partial pressure \times Henry's law coefficient
<i>Isotopologue discrimination factors</i>			
$^{33}\epsilon_R$	Respiration discrimination for $^{33}O_2$	$(^{34}\alpha_R)^{\beta_{34/33,R}} - 1$	
$^{34}\epsilon_R$	Respiration discrimination for $^{34}O_2$	-24‰	Days 1 – 30
		-12.5‰ -17‰	Days 30 – 90 Days 90 – 378
$^{35}\epsilon_R$	Respiration discrimination for $^{35}O_2$	$(^{34}\alpha_R)^{\beta_{34/35,R}} - 1$	
$^{36}\epsilon_R$	Respiration discrimination for $^{36}O_2$	$(^{34}\alpha_R)^{\beta_{34/36,R}} - 1$	
$^{33}\epsilon_{GE,kinetic}$	Kinetic gas-exchange discrimination for $^{33}O_2$	$(^{34}\alpha_{GE,kinetic})^{\beta_{34/33,GE,kinetic}} - 1$	
$^{34}\epsilon_{kGE,kinetic}$	Kinetic gas-exchange discrimination for $^{34}O_2$	-2.8‰	Ref. (Knox et al., 1992)
$^{35}\epsilon_{GE,kinetic}$	Kinetic gas-exchange discrimination for $^{35}O_2$	$(^{34}\alpha_{GE,kinetic})^{\beta_{34/35,GE,kinetic}} - 1$	
$^{36}\epsilon_{GE,kinetic}$	Kinetic gas-exchange discrimination for $^{36}O_2$	$(^{34}\alpha_{GE,kinetic})^{\beta_{34/36,GE,kinetic}} - 1$	
$^{33}\epsilon_{GE,eq}$	Gas-exchange equilibrium for $^{33}O_2$	0.38‰	At 25°C , Ref. (Benson and Krause Jr., 1984)
$^{34}\epsilon_{GE,eq}$	Gas-exchange equilibrium for $^{34}O_2$	0.73‰	At 25°C , Ref. (Benson and Krause Jr., 1984)
$^{35}\epsilon_{GE,eq}$	Gas-exchange equilibrium for $^{35}O_2$	$(^{34}\alpha_{GE,eq})^{1.5} - 1$	
$^{36}\epsilon_{GE,eq}$	Gas-exchange equilibrium for $^{36}O_2$	$(^{34}\alpha_{GE,eq})^2 - 1$	

Table S3.1 (con't): Description of model parameters used in Figures 3.2, S3.2, S3.3, S3.4 and S3.5

Parameter	Description	Value	Notes
<i>Mass-dependent exponents</i>			
$\beta_{34/33,R}$	Respiration, $^{33}\text{O}_2$ vs. $^{34}\text{O}_2$	0.514	Days 1 – 30
		0.517	Days 30 – 378
$\beta_{34/35,R}$	Respiration, $^{35}\text{O}_2$ vs. $^{34}\text{O}_2$	1.52	MDF case
		2.01	non-MDF case
$\beta_{34/36,R}$	Respiration, $^{36}\text{O}_2$ vs. $^{34}\text{O}_2$	2.02	MDF case
		2.94	non-MDF case
$\beta_{34/33,kGE}$	Kinetic gas exchange, $^{33}\text{O}_2$ vs. $^{34}\text{O}_2$	0.510	
$\beta_{34/35,kGE}$	Kinetic gas exchange, $^{35}\text{O}_2$ vs. $^{34}\text{O}_2$	1.47	MDF case
		1.82	non-MDF case

Table S3.2. Initial isotopic composition of terrarium reservoirs

Parameter	Description	Value	Notes
$\delta'^{18}\text{O}_{\text{water}}$	Photosynthesis source water	-9.251‰	Measured by IRMS
$\delta'^{17}\text{O}_{\text{water}}$	Photosynthesis source water	-4.826‰	Measured by IRMS
$\delta'^{18}\text{O}_{\text{air}}$	Atmospheric O_2	23.260‰	Ref. (Young et al., 2014)
$\delta'^{17}\text{O}_{\text{air}}$	Atmospheric O_2	11.828‰	Ref. (Young et al., 2014)
$\Delta_{35,\text{air}}$	Atmospheric O_2	1.0‰	Ref. (Yeung et al., 2014)
$\Delta_{36,\text{air}}$	Atmospheric O_2	1.97‰	Ref. (Yeung et al., 2014)

Table S3.3. Terrarium O₂ concentration and isotopologue data

Date	Day	Sample	Time	O ₂ / atm	δ ¹⁸ O / ‰	δ ¹⁷ O / ‰	Δ ¹⁷ O / ppm	Δ ₃₅ / ‰	Δ ₃₆ / ‰
<i>12h/12h Light/dark cycles</i>									
7/11/2013	0	B3-000	12:15 PM	0.210	-0.345	-0.172	7	1.28	2.06
7/12/2013	1	B3-001	7:25 AM	0.198	0.163	0.098	13	1.14	1.90
7/13/2013	2	B3-002	8:05 AM	0.199	-2.401	-1.215	29	0.82	1.47
7/15/2013	4	B3-003	7:20 AM	0.205	-5.392	-2.760	33	0.54	1.25
7/17/2013	6	B3-004	8:07 AM	0.208	-6.336	-3.235	47	0.69	1.13
7/20/2013	9	B3-005	9:32 AM	N/A	-7.017	-3.585	50	0.22	0.66
7/23/2013	12	B3-006	7:15 AM	0.204	-7.233	-3.689	58	0.40	0.92
7/24/2013	13	B3-007	12:10 PM	0.207	-8.076	-4.115	68	0.60	0.97
<i>Early</i>									
8/1/2013	21	B3-008	AM	0.200	-7.967	-4.056	72	0.37	0.18
8/9/2013	29	B3-010	7:30 AM	0.199	-8.847	-4.501	81	0.24	0.64
10/7/2013	88	B3-011	1:35 PM	0.157	-20.555	-10.501	146	0.33	0.43
10/10/2013	91	B3-012	9:25 AM	0.161	-19.996	-10.201	157	0.51	0.04
12/3/2013	145	B3-014	7:30 PM	0.205	-16.351	-8.301	169	0.11	-0.08
12/7/2013	149	B3-015	8:00 AM	0.204	-15.790	-8.012	168	0.08	0.24
1/9/2014	182	B3-016	Late AM	0.214	-15.875	-8.058	165	-0.10	-0.10
1/11/2014	184	B3-017	Late AM	0.222	-16.091	-8.170	165	0.00	-0.08
<i>Dark incubation #1</i>									
10:35									
1/12/2014	185	B3-018	AM	0.217	-15.826	-8.034	164	0.18	0.08
1/13/2014	186	B3-019	9:20 AM	0.206	-15.481	-7.854	165	0.05	0.38
10:00									
1/14/2014	187	B3-020	AM	0.186	-15.255	-7.752	150	0.13	0.71
1/15/2014	188	B3-021	8:00 AM	0.173	-14.895	-7.560	156	0.28	0.76
1/16/2014	189	B3-022	8:00 AM	0.174	-14.728	-7.468	161	-0.02	0.80
1/17/2014	190	B3-023	8:00 AM	0.164	-14.243	-7.218	160	-0.02	0.95
1/18/2014	191	B3-024	8:00 AM	0.149	-14.083	-7.137	158	0.20	1.08
<i>12h/12h Light/dark cycles (started 1/19/2014)</i>									
10:00									
7/10/2014	364	B3-026	AM	0.282	-15.885	-8.068	161	0.03	0.02
11:30									
7/14/2014	368	B3-027	AM	0.287	-15.751	-7.996	163	0.07	-0.12
10:30									
7/17/2014	371	B3-028	AM	0.291	-15.795	-8.020	162	-0.16	-0.17
<i>Dark incubation #2</i>									
7/18/2014	372	B3-029	1:15 PM	0.287	-15.592	-7.920	156	0.11	-0.15
11:15									
7/19/2014	373	B3-030	AM	0.280	-15.513	-7.876	159	0.07	-0.08
11:15									
7/22/2014	376	B3-031	AM	0.253	-15.126	-7.676	159	0.18	0.90
7/23/2014	377	B3-032	12:00 PM	0.242	-14.851	-7.540	152	0.19	1.40
7/24/2014	378	B3-033	12:15 PM	0.233	-14.639	-7.432	150	0.16	1.16

Photochemical equilibrations at 30°C

Sample	$\delta^{18}\text{O}$	$\delta^{17}\text{O}$	$\Delta^{17}\text{O}$	Predicted		Measured	
	/ ‰	/ ‰	/ ppm	Δ_{35} / ‰	Δ_{36} / ‰	Δ_{35} / ‰	Δ_{36} / ‰
B3-026	-16.321	-8.299	155	0.77	1.47	0.67	1.39
B3-031	-14.956	-7.603	144	0.77	1.47	0.75	1.55

References

- Affek, H.P. (2013) Clumped Isotopic Equilibrium and the Rate of Isotope Exchange between CO_2 and Water. *Am J Sci* 313, 309-325.
- Affek, H.P. and Zaarur, S. (2014) Kinetic isotope effect in CO_2 degassing: Insight from clumped and oxygen isotopes in laboratory precipitation experiments. *Geochim Cosmochim Acta* 143, 319-330.
- Angeles-Boza, A.M., Ertem, M.Z., Sarma, R., Ibañez, C.H., Maji, S., Llobet, A., Cramer, C.J. and Roth, J.P. (2014) Competitive oxygen-18 kinetic isotope effects expose O–O bond formation in water oxidation catalysis by monomeric and dimeric ruthenium complexes. *Chemical Science* 5, 1141-1152.
- Angeles-Boza, A.M. and Roth, J.P. (2012) Oxygen kinetic isotope effects upon catalytic water oxidation by a monomeric ruthenium complex. *Inorganic Chemistry* 51, 4722-4729.
- Angert, A., Rachmilevitch, S., Barkan, E. and Luz, B. (2003) Effects of photorespiration, the cytochrome pathway, and the alternative pathway on the triple isotopic composition on atmospheric O_2 . *Global Biogeochemical Cycles* 17, 1030.
- Badger, M.R., von Caemmerer, S., Ruuska, A. and Nakano, H. (2000) Electron flow to oxygen in higher plants and algae: rates and control of direct photoreduction (Mehler reaction) and rubisco oxygenase. *Philosophical Transactions of the Royal Society B* 355, 1433-1446.
- Baker, L., Franchi, I.A., Maynard, J., Wright, I.P. and Pillinger, C.T. (2002) A technique for the determination of $^{18}\text{O}/^{16}\text{O}$ and $^{17}\text{O}/^{16}\text{O}$ isotopic ratios in water from small liquid and solid samples *Anal Chem* 74, 1665-1673.
- Barkan, E. and Luz, B. (2005) High precision measurements of $^{17}\text{O}/^{16}\text{O}$ and $^{18}\text{O}/^{16}\text{O}$ ratios in H_2O . *Rapid Communications in Mass Spectrometry* 19, 3737-3742.
- Barkan, E. and Luz, B. (2011) The relationship among the three stable isotopes of oxygen in air, seawater and marine photosynthesis. *Rapid Communications in Mass Spectrometry* 25, 2367-2369.
- Benson, B.B. and Krause Jr., D. (1984) The concentration and isotopic fractionation of oxygen dissolved in freshwater and seawater in equilibrium with the atmosphere. *Limnol Oceanogr* 29, 620-632.
- Berman, E.S.F., Levin, N.E., Landais, A., Li, S. and Owano, T. (2013) Measurement of $\delta^{18}\text{O}$, $\delta^{17}\text{O}$, and ^{17}O -excess in water by off-axis integrated cavity output spectroscopy and isotope ratio mass spectrometry. *Anal Chem* 85, 10,392-310,398.
- Canvin, D.T., Berry, J.A., Badger, M.R., Fock, H. and Osmund, C.B. (1980) Oxygen exchange in leaves in the light. *Plant Physiology* 66, 302-307.

Cheah, M.H., Millar, A.H., Myers, R.C., Day, D.A., Roth, J., Hillier, W. and Badger, M.R. (2014) Online Oxygen Kinetic Isotope Effects Using Membrane Inlet Mass Spectrometry Can Differentiate between Oxidases for Mechanistic Studies and Calculation of Their Contributions to Oxygen Consumption in Whole Tissues. *Anal Chem* 86, 5171-5178.

Cox, N., Retegan, M., Neese, F., Pantazis, D.A., Boussac, A. and Lubitz, W. (2014) Electronic structure of the oxygen-evolving complex in photosystem II prior to O-O bond formation. *Science* (Washington, D. C., 1883-) 345, 804-808.

Ghosh, P., Adkins, J., Affek, H., Balta, B., Guo, W., Schauble, E.A., Schrag, D. and Eiler, J.M. (2006) ^{13}C - ^{18}O bonds in carbonate materials: A new kind of paleothermometer. *Geochim Cosmochim Acta* 70, 1439-1456.

Guo, W., Mosenfelder, J.L., Goddard III, W.A. and Eiler, J.M. (2009) Isotopic fractionations associated with phosphoric acid digestion of carbonate minerals: Insights from first-principles theoretical modeling and clumped isotope measurements *Geochim Cosmochim Acta* 73, 7203-7225.

Guy, R.D., Berry, J.A., Fogel, M.L. and Hoering, T.C. (1989) Differential fractionation of oxygen isotopes by cyanide-resistant and cyanide-sensitive respiration in plants. *Planta* 177, 483-491.

Guy, R.D., Fogel, M.L. and Berry, J.A. (1993) Photosynthetic Fractionation of the Stable Isotopes of Oxygen and Carbon. *Plant Physiology* 101, 37-47.

Helman, Y., Barkan, E., Eisenstadt, D., Luz, B. and Kaplan, A. (2005) Fractionation of the Three Stable Oxygen Isotopes by Oxygen-Producing and Oxygen-Consuming Reactions in Photosynthetic Organisms. *Plant Physiology* 138, 2292-2298.

Hillier, W. and Wydrzynski, T. (2008) ^{18}O -water exchange in photosystem II: Substrate binding and intermediates of the water splitting cycle. *Coordination Chemistry Reviews* 252, 306-317.

Hoffman, B.M., Lukoyanov, D., Dean, D.R. and Seefeldt, L.C. (2013) Nitrogenase: A Draft Mechanism. *Accounts of Chemical Research* 46, 587-595.

Juranek, L.W. and Quay, P.D. (2013) Using Triple Isotopes of Dissolved Oxygen to Evaluate Global Marine Productivity. *Annual Review of Marine Science* 5, 503-524.

Knox, M., Quay, P.D. and Wilbur, D. (1992) Kinetic isotope fractionation during air-water gas transfer of O_2 , N_2 , CH_4 , and H_2 . *Journal of Geophysical Research* 97, 335-343.

Kok, B., Forbush, B. and McGloin, M. (1970) Cooperation of charges in photosynthetic evolution - 1. A linear four step mechanism. *Photochemistry and Photobiology* 11, 457-475.

- Luz, B. and Barkan, E. (2005) The isotopic ratios $^{17}\text{O}/^{16}\text{O}$ and $^{18}\text{O}/^{16}\text{O}$ in molecular oxygen and their significance in biogeochemistry. *Geochim Cosmochim Acta* 69, 1099-1110.
- Luz, B., Barkan, E., Bender, M.L., Thiemens, M.H. and Boering, K.A. (1999) Triple-isotope composition of atmospheric oxygen as a tracer of biosphere productivity. *Nature (London)* 400, 547-550.
- Noguchi, T. (2008) FTIR detection of water reactions in the oxygen-evolving centre of photosystem II. *Philosophical Transactions of the Royal Society B* 363, 1189-1195.
- Ono, S., Wang, D.T., Gruen, D.S., Sherwood-Lollar, B., Zahniser, M.S., McManus, B.J. and Nelson, D.D. (2014) Measurement of doubly substituted methane isotopologue, $^{13}\text{CH}_3\text{D}$, by tunable infrared laser direct absorption spectroscopy. *Anal Chem* 86, 6487-6494.
- Passey, B.H. and Henkes, G.A. (2012) Carbonate clumped isotope bond reordering and geospeedometry. *Earth and Planetary Science Letters* 351-352.
- Patterson, D.T. and Duke, S.O. (1979) Effect of growth irradiance on the maximum photosynthetic capacity of water hyacinth [*Eichhornia crassipes* (Mart.) Solms]. *Plant and Cell Physiology* 20, 177-184.
- Rapatskiy, L., Cox, N., Savitski, A., Ames, W.M., Sander, J., Nowaczyk, M.M., Rögner, M., Boussac, A., Neese, F., Messinger, J. and Lubitz, W. (2012) Detection of the Water-Binding Sites of the Oxygen-Evolving Complex of Photosystem II Using W-Band ^{17}O Electron-Electron Double Resonance-Detected NMR Spectroscopy. *Journal of the American Chemical Society* 134, 16619-16634.
- Richet, P., Bottinga, Y. and Javoy, M. (1977) A review of hydrogen, carbon, nitrogen, oxygen, sulphur, and chlorine stable isotope fractionation among gaseous molecules. *Annual Review of Earth and Planetary Science* 5, 65-110.
- Schoenemann, S.W., Schauer, A.J. and Steig, E.J. (2014) Measurement of SLAP2 and GISP $\delta^{17}\text{O}$ and proposed VSMOW-SLAP normalization for $\delta^{17}\text{O}$ and $^{17}\text{O}_{\text{excess}}$. *Rapid Communications in Mass Spectrometry* 27, 582-590.
- Spencer, W. and Bowes, G. (1986) Photosynthesis and growth of water hyacinth under CO_2 enrichment. *Plant Physiology* 82, 528-533.
- Stevens, C.L.R., Schultz, D., Van Baalen, C. and Parker, P.L. (1975) Oxygen isotope fractionation during photosynthesis in a blue-green and green alga. *Plant Physiology* 56, 126-129.
- Stolper, D.A., Lawson, M., Davis, C.L., Ferreira, A.A., Neto, E.V.S., Ellis, G.S., Lewan, M.D., Martini, A.M., Tang, Y., Schoell, M., Sessions, A.L. and Eiler, J.M. (2014a) Formation temperatures of thermogenic and biogenic methane. *Science* 344, 1500-1503.

Stolper, D.A., Sessions, A.L., Ferreira, A.A., Neto, E.V.S., Schimmelmann, A., Shusta, S.S., Valentine, D.L. and Eiler, J.M. (2014b) Combined ^{13}C -D and D-D clumping in methane: Methods and preliminary results. *Geochim Cosmochim Acta* 126, 169-191.

Tanaka, R. and Nakamura, E. (2012) Determination of ^{17}O -excess of terrestrial silicate/oxide minerals with respect to Vienna Standard Mean Ocean Water (VSMOW). *Rapid Communications in Mass Spectrometry* 27, 285-297.

Tang, J., Dietzel, M., Fernandez, A., Tripathi, A.K. and Rosenheim, B.E. (2014) Evaluation of kinetic effects on clumped isotope fractionation (Δ_{47}) during inorganic calcite precipitation. *Geochim Cosmochim Acta* 134, 120-136.

Tempest, K.E. and Emerson, S. (2013) Kinetic isotopic fractionation of argon and neon during air-water gas transfer. *Marine Chemistry* 153, 39-47.

Thiemens, M.H. (2006) History and Applications of Mass-Independent Isotope Effects. *Annual Review of Earth and Planetary Science* 34, 217-262.

Thurston, R.S., Mandernack, K.W. and Shanks III, W.C. (2010) Laboratory chalcopyrite oxidation by *Acidithiobacillus ferrooxidans*: Oxygen and sulfur isotope fractionation. *Chem Geol* 269, 252-261.

Urey, H.C. and Grieff, L.J. (1935) Isotopic exchange equilibria. *Journal of the American Chemical Society* 57, 321-327.

Wang, Z.G., Schauble, E.A. and Eiler, J.M. (2004) Equilibrium thermodynamics of multiply substituted isotopologues of molecular gases. *Geochim Cosmochim Acta* 68, 4779-4797.

Yeung, L.Y., Ash, J.L. and Young, E.D. (2014) Rapid photochemical equilibration of isotope bond ordering in O_2 . *Journal of Geophysical Research* 119, 10552-10566.

Yeung, L.Y., Young, E.D. and Schauble, E.A. (2012) Measurements of $^{18}\text{O}^{18}\text{O}$ and $^{17}\text{O}^{18}\text{O}$ in the atmosphere and the influence of isotope-exchange reactions. *Journal of Geophysical Research* 117, D18306.

Young, E.D., Galy, A. and Nagahara, H. (2002) Kinetic and equilibrium mass-dependent isotope fractionation laws in nature and their geochemical and cosmochemical significance. *Geochim Cosmochim Acta* 66, 1095-1104.

Young, E.D., Yeung, L.Y. and Kohl, I.E. (2014) On the $\Delta^{17}\text{O}$ Budget of Atmospheric O_2 . *Geochim Cosmochim Acta* 135, 102-125.

Chapter 4: Exchange catalysis during anaerobic methanotrophy revealed by $^{12}\text{CH}_2\text{D}_2$ and $^{13}\text{CH}_3\text{D}$ in methane gas

Recent discoveries of dynamically varying methane in the Martian atmosphere and molecular hydrogen in the plumes of Enceladus have renewed excitement about the role of reduced gases of astrobiological potential and the possibility that habitability may not be unique to Earth (Waite et al., 2017; Webster et al., 2015). Methane can be produced in a number of biological and abiotic reactions, precluding our ability to determine unequivocally their sources on extraterrestrial bodies (Etiope and Sherwood Lollar, 2013; McCollom and Seewald, 2007). Even on Earth, where direct measurements of methane and substrate characteristics are possible, distinguishing microbial from other methanogenesis pathways is problematic (Martini et al., 1996; McCollom and Seewald, 2006; Pohlman et al., 2009; Whiticar, 1990). Additional complexity in sourcing methane is introduced by methanotrophy, the aerobic or anaerobic consumption of methane by microbes. This process can alter the parameters that are traditionally useful in sourcing methane such as bulk isotope ratios (Whiticar, 1999). Perhaps nowhere is this complexity greater than in the deep biosphere, where linking biogeochemistry to metabolisms and metabolisms to activities remains a standing challenge (Edwards et al., 2012).

Coupling exploration of the enzymatic chemistry that drives these cycles with isotope geochemical probing can provide powerful insights. Here, we focus on the anaerobic oxidation of methane (AOM), estimated to consume ~90% of methane created in marine sediments (Knittel and Boetius, 2009). AOM is traditionally thought to be carried out by a consortium of methane-oxidizing archaea and sulfate-reducing bacteria performing the

net reaction $\text{CH}_4 + \text{SO}_4^{2-} \rightarrow \text{HCO}_3^- + \text{HS}^- + \text{H}_2\text{O}$ (Boetius et al., 2000), although evidence suggests that these processes can be decoupled (Milucka et al., 2012; Scheller et al., 2016) and metal oxides may also act as terminal electron acceptors (Beal et al., 2009). In all cases, the first step of AOM involves interaction between methane and a modified methyl-coenzyme M reductase (*mcr*), the terminal enzyme in methanogenesis (Krüger et al., 2003; Scheller et al., 2010; Timmers et al., 2017). Methane production and consumption are linked via this homologous enzyme, prompting questions regarding the full or partial reversibility of these metabolisms (Lloyd et al., 2011).

Recent developments in high-resolution isotope-ratio mass spectrometry permit the interrogation of these metabolisms in field samples by determining high-precision concentrations of molecules containing at least two heavy isotopes. These multiply-substituted gas species, referred to as “clumped” isotopologues, are sensitive indicators of reversibility in reactions because they can drive clumped isotopologues toward intra-species isotopic equilibrium. The relative proportions of two rare but stable isotopologues in methane, $^{13}\text{CH}_3\text{D}$ and $^{12}\text{CH}_2\text{D}_2$ (reported as $\Delta^{13}\text{CH}_3\text{D}$ and $\Delta^{12}\text{CH}_2\text{D}_2$ values relative to a random distribution of isotopes among all CH_4 isotopologues; see Materials and Methods), have known temperature-sensitive equilibrium concentrations, and their relative proportions can be used as a geothermometer for thermogenic methane (Stolper et al., 2014a; Wang et al., 2015; Young et al., 2017).

Intriguingly, many environmental samples of methane exhibit non-equilibrium clumped isotope distributions (Wang et al., 2015; Young et al., 2017; Young et al., 2016).

Microbial methane in particular displays clumped isotopologue concentrations that range from those consistent with low-temperature equilibration within the environment of formation (Inagaki et al., 2015) to those with extreme depletions in $\Delta^{13}\text{CH}_3\text{D}$ and $\Delta^{12}\text{CH}_2\text{D}_2$ values reflective of isotope effects associated with kinetic processes (Wang et al., 2015; Young et al., 2017). This span in clumped-isotope distributions suggests that enzymatic reactions associated with methane metabolisms are capable of ranging from reversible to kinetic. How methanogenesis and methanotrophy contribute to these signals is an open debate.

Hypotheses to explain clumped-isotopologue variations in microbial methane have relied on the rate of methanogenesis controlling the degree of terminal reversibility of this metabolism (Stolper et al., 2015; Wang et al., 2015). These studies utilize only $\Delta^{13}\text{CH}_3\text{D}$ to gauge the degree of equilibrium, but comparisons of $\Delta^{13}\text{CH}_3\text{D}$ to environmental temperature and water isotopes alone are insufficient indicators of thermodynamic equilibrium. Processes like abiotic methane formation and physical mixing are capable of producing $\Delta^{13}\text{CH}_3\text{D}$ in apparent equilibrium, while examining $\Delta^{12}\text{CH}_2\text{D}_2$ reveals they are far from intra-species thermodynamic equilibrium (Young et al., 2017; Young et al., 2016). Furthermore, comparisons of $\Delta^{13}\text{CH}_3\text{D}$ to hydrogen isotopes in water (Douglas et al., 2016; Stolper et al., 2015; Wang et al., 2015) may also be problematic as the assumption that methane formation derives all hydrogen from water does not hold for all pathways of methane formation (Pine and Barker, 1956; Waldron et al., 1999). Measuring $\Delta^{12}\text{CH}_2\text{D}_2$ in addition to $\Delta^{13}\text{CH}_3\text{D}$ shows the true degree of equilibrium in a pool of methane (Young et al., 2017).

We suggest instead that methanogenesis is a terminally irreversible reaction, creating methane with clumped-isotope compositions in disequilibrium with environmental temperatures. On the other hand, AOM is known to have an enzymatic back-reaction (Holler et al., 2011; Yoshinaga et al., 2014) that we suggest drives methane towards thermodynamic equilibrium. We test this hypothesis by measuring $\delta^{13}\text{C}$, δD , $\Delta^{13}\text{CH}_3\text{D}$ and $\Delta^{12}\text{CH}_2\text{D}_2$ in sedimentary methane from the top 30 meters of Bornholm Basin, Baltic Sea collected during IODP Expedition 347, where methane produced in sediments deposited under brackish-marine conditions diffuses down into a lacustrine sediment package (see Materials and Methods). Metagenomic analysis reveals methyl coenzyme reductase subunit A (*mcrA*) is present throughout the core and indicates that anaerobic methanotrophs (ANME-1) and relatives of the methanogen *Methanohalobium evestigatum* are present (Marshall et al., 2017). We compare these data to geochemical profiles (Andr n et al., 2015; Egger et al., 2017) and rates of methanogenesis and methanotrophy derived from a multicomponent diagenetic model (Dijkstra et al., 2017) to determine the key parameters controlling the isotopic composition of methane in the deep biosphere.

Methane concentrations decrease from 10.1 to 1.4 mM over an interval of 3.5 to 30.0 meters composite depth [MCD, akin to meters below seafloor (Andr n et al., 2015)] and sulfate concentrations are <0.5 mM throughout while two sulfate methane transition zones (SMTZ) are noted at 3.3 MCD and 19 MCD (Fig. 4.1e-f). In sulfate-poor lacustrine sediments such as those from 10-20 MCD, metal oxides may play a role in methane

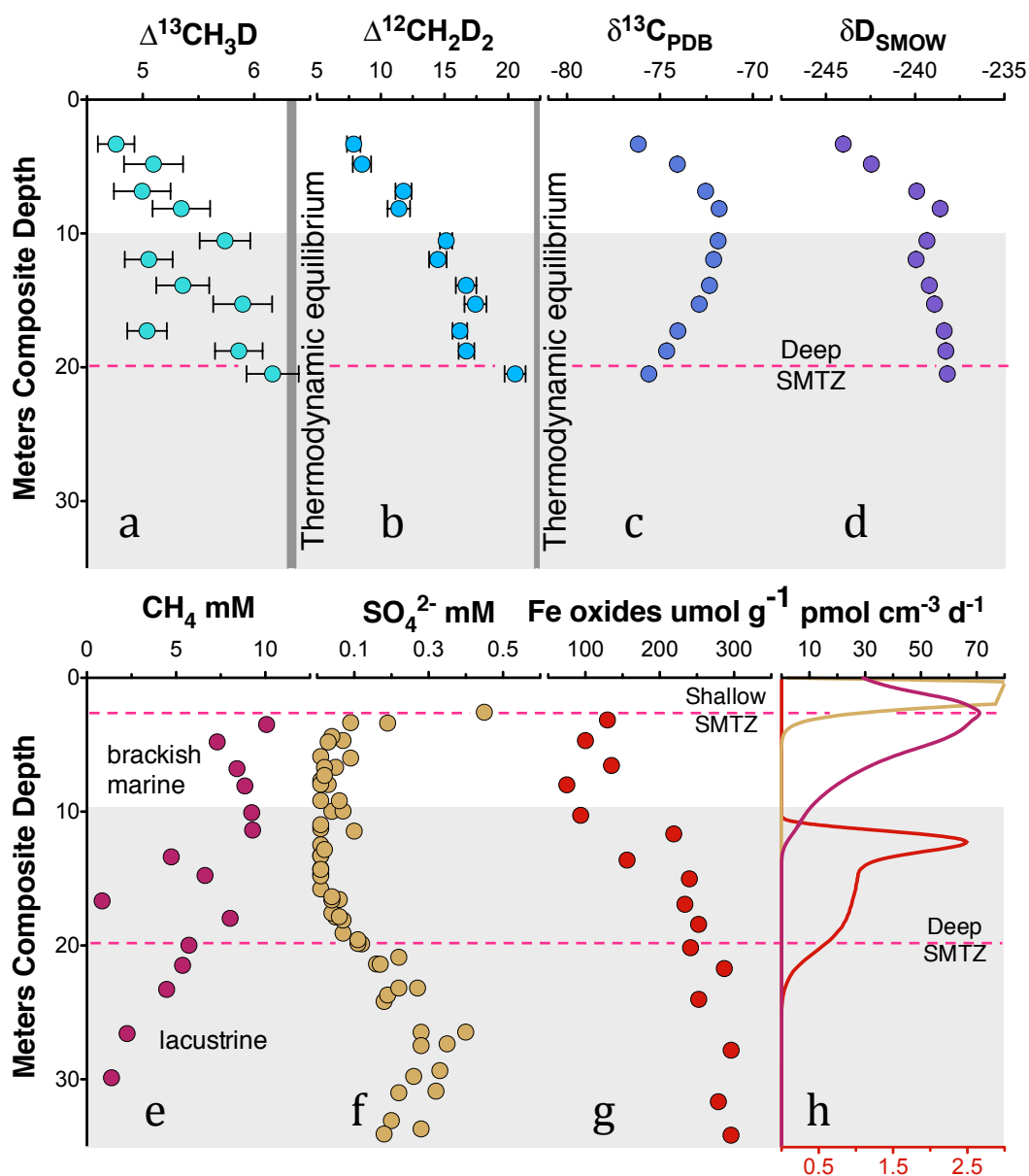


Figure 4.1: Geochemical profiles from Bornholm Basin from 3-30 MCD. Horizontal grey bar denotes sediments deposited during lacustrine conditions overlain with sediments deposited during brackish marine conditions. The 3 meters directly beneath the sediment-water transition were not collected due to safety concerns, so measurements were only made on samples collected below the shallow sulfate-methane transition zone (SMTZ). Pink dashed lines denote the shallow (3.3 MCD) and deep (19.8 MCD) SMTZ; the shallow SMTZ is only shown in the bottom panel for clarity. Grey vertical bars in **b** and **c** denote equilibrium isotopologue compositions for core temperature of $7.8 \pm 0.6^\circ\text{C}$. Modeled CH_4 production, Fe-AOM and $\text{SO}_4\text{-AOM}$ rates are shown in panel **h** (Dijkstra et al., 2017). CH_4 production (purple) and $\text{SO}_4\text{-AOM}$ (gold) rates correspond with the upper x-axis and Fe-AOM rates (red) correspond with the lower x-axis.

consumption (Sivan et al., 2011), and iron oxide concentrations range from ~100 to 300 $\mu\text{mol g}^{-1}$ (Fig 4.1g) (Egger et al., 2017). At 3.3 MCD, methane $\delta^{13}\text{C}$ is -76.16‰, then increases to a maximum of -71.81‰ by 8.1 MCD, followed by a decrease downcore to -75.59‰ (Fig. 4.1c). Methane δD at 3.3 MCD is the most negative hydrogen isotope value throughout the core at -244.0‰ and downcore, δD in methane increases to -238.2‰ with a small reversal present between 10-12 MCD before the trend of increasing δD resumes (Fig 4.1d). $\Delta^{13}\text{CH}_3\text{D}$ and $\Delta^{12}\text{CH}_2\text{D}_2$ values increase monotonically downcore (Fig. 4.1a-b). At the shallowest measured depth of 3.5 MCD, values of 1.5‰ and 14.4‰ for $\Delta^{13}\text{CH}_3\text{D}$ and $\Delta^{12}\text{CH}_2\text{D}_2$, respectively, are lower than calculated equilibrium values of 6.3‰ and 22.3‰, respectively, for the average ambient core temperature of $7.8 \pm 0.6^\circ\text{C}$. Activity measurements imply that methanogenesis rates decrease and AOM rates increase with depth (Fig. S4.3, Table S4.1). Diagenetic porewater modeling shows a methane production peak at 2.7 MCD that decreases downcore and peak Fe-AOM consumption at 12 MCD [Fig 4.1h (Dijkstra et al., 2017)]. It is likely that the SMTZ at 19 MCD is an important additional methane sink, however we were unable to constrain SO_4 -AOM rates at this depth. Therefore, we consider the Fe-AOM rates derived from modeling as a lowest possible estimate for total AOM activity at these depths.

Comparing the measured $\Delta^{12}\text{CH}_2\text{D}_2$ values to the equilibrium $\Delta^{12}\text{CH}_2\text{D}_2$ values associated with measured $\Delta^{13}\text{CH}_3\text{D}$ values illustrates the degree of thermodynamic disequilibrium, a parameter we refer to as $\xi_{12\text{CH}_2\text{D}_2}$ by analogy with the well-known reaction progress variable (See materials and methods). $\xi_{12\text{CH}_2\text{D}_2}$ values near zero imply isotopic equilibration, while values above or below zero are signatures of disequilibrium. Values

for $\xi_{^{12}\text{CH}_2\text{D}_2}$ in the shallowest depths are as high as 7.5‰ are clear evidence for disequilibrium while zero (and thus thermodynamic equilibrium) is approached as depth increases (Fig S4.3). To determine how methanogenesis and methanotrophy influence this transition, we discuss evidence for reversibility in each metabolism.

Methane production in intra-species, thermodynamic equilibrium requires reversibility at the final step of methanogenesis via enzymatic back reaction. If methanogenesis is reversible at this terminal step, then the directionality of methanogenesis should be influenced by the concentration of products and reactants. For example, in the reaction $\text{CO}_2 + 4\text{H}_2 \rightarrow \text{CH}_4 + 2\text{H}_2\text{O}$, H_2 concentrations would control the rate of CH_4 oxidation via the reverse reaction. Trace methane oxidation (TMO) does occur during methanogenesis, but altering the concentration of H_2 or terminal electron acceptors necessary for oxidizing methane does not increase TMO (Moran et al., 2005). For a variety of substrates and concentrations, TMO has never been shown to consume greater than 0.5% of the CH_4 produced. Although some of the first steps of methanogenesis may be reversible (Valentine et al., 2004), the final transfer of the methyl group to coenzyme M and the subsequent final hydrogen addition are believed to be irreversible (Gärtner et al., 1994). Moreover, with one exception, all clumped-isotope measurements of methane produced by axenic lab cultures have shown methane in intra-species isotopic disequilibrium (Stolper et al., 2015; Wang et al., 2015; Young et al., 2017), indicating at least some degree of irreversibility in this metabolism. The one axenic culture experiment of a thermophilic methanogen grown on an H_2/CO_2 substrate that produced a clumped isotope

temperature consistent with its growth conditions (Stolper et al., 2014b) has never been reproduced.

On the other hand, AOM has been shown to have a substantial enzymatic back reaction that suggests the first step of anaerobic methanotrophy is partially reversible, providing a potential mechanism for equilibrating methane isotopologues with environmental temperatures. This back reaction is sensitive to concentrations of the terminal electron acceptor SO_4^{2-} (Holler et al., 2011; Yoshinaga et al., 2014). At high concentrations of SO_4^{2-} , the back reaction produces 3-7% of the CH_4 consumed by AOM, and at low concentrations of SO_4^{2-} (below 0.5 mM), back reaction can produce as much as 78% of the CH_4 consumed by AOM (Timmers et al., 2017). If methanotrophs actively concentrate methane in their cells and expose it to *mcr* where it is equilibrated, but then much of this methane diffuses back out of the cell, a reservoir of methane could gradually move towards thermodynamic equilibrium. Using estimates of AOM rates from above, we calculate the timescale of this equilibration (see Materials and Methods) to be on the order of 10^3 - 10^4 years, appropriate for the estimated age of methane at 20 MCD of ~8000 years [Fig. S4.1-2, (Dijkstra et al., 2017)].

Here, both Fe-AOM and SO_4 -AOM are potential methane consumption pathways. Evidence for enzymatic back-flux during AOM with iron as the terminal electron acceptor has yet to be shown, but it has been suggested that the Gibbs free energies of reaction at standard conditions ($\Delta G^\circ = -16.3 \text{ kJ mol}^{-1}$ for SO_4 -AOM and $\Delta G^\circ = -571.2 \text{ kJ mol}^{-1}$ for Fe-AOM) imply that Fe-AOM would be less reversible than SO_4 -AOM, and

therefore a weaker mechanism for equilibrating methane (Timmers et al., 2017). However, we calculate the Gibbs free energies of reaction ($\Delta G = \Delta G^\circ + RT \ln Q$ where Q is the activity quotient for the reaction) for in situ concentrations in the equilibrated methane zone (20 MCD) in Bornholm Basin and obtain values of $-33.8 \text{ kJ mol}^{-1}$ for SO_4 -AOM and $-93.4 \text{ kJ mol}^{-1}$ for Fe-AOM (Table S4.2). These values suggest that both metabolisms are energetically favorable. Furthermore, it has been previously suggested that actual free energy dissipation during such reactions is less negative than that suggested by calculations based on in situ concentrations due to coupling to energy conservation (Holler et al., 2011), implying that enzymatic back flux may be possible in both Fe-AOM and SO_4 -AOM even at these Gibbs free energies.

Finally, experiments suggest that AOM back-flux is capable of reversing the canonical stable isotope trend expected during methanotrophy (Yoshinaga et al., 2014); the methane residue is progressively depleted in heavy isotopes of carbon rather than enriched during lab incubations where sulfate is limited. Such a reversal is present in the $\delta^{13}\text{C}_{\text{CH}_4}$ profile of the downward diffusing methane of Bornholm Basin, but interpreting such signals can be difficult where methane produced in modern-late Holocene brackish-marine sediments is transported into glacial-lacustrine sediments with each sedimentary package having unique carbon and hydrogen reservoirs (Egger et al., 2017). Our findings suggest that when terminal electron acceptors are limiting, equilibrium bond ordering may be used to identify AOM activity even when the bulk isotopic composition of reservoir material is changing.

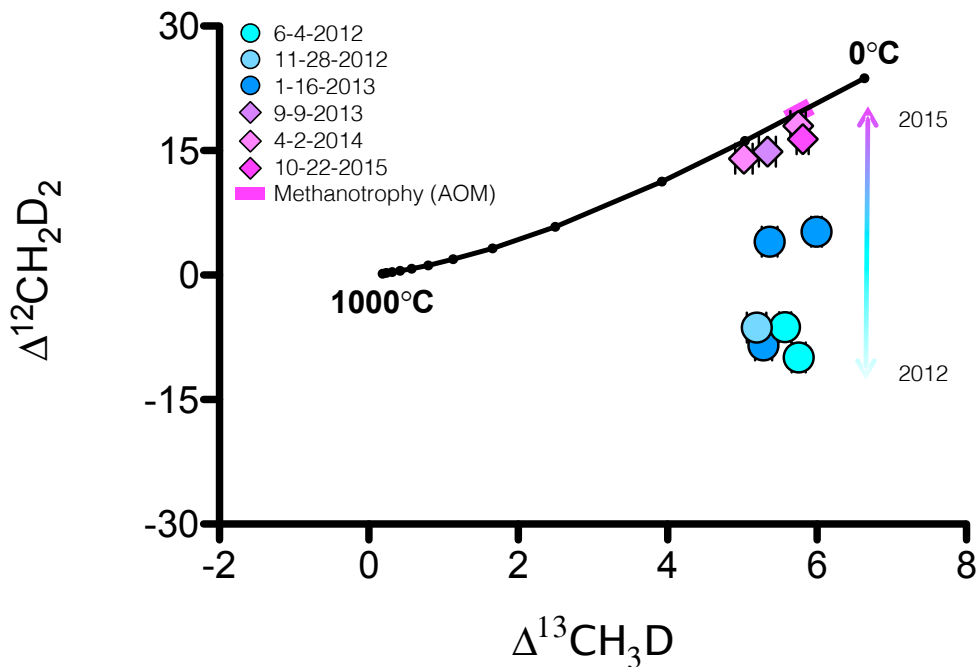


Figure 4.2: $^{13}\text{CH}_3\text{D}$ and $^{12}\text{CH}_2\text{D}_2$ isotopologue relative abundances in methane collected from Kidd Creek Mine are shown compared to the theoretical thermodynamic equilibrium abundances (black line with dots representing 100°C increments from 0-1000°C). Circles represent those samples taken from 9800 feet depth and diamonds represent those taken from a depth of 7850 feet and the dates shown in the legend reference the time of gas sampling.

AOM is a critical element of the carbon cycle that cannot be ignored when examining methane from anoxic environments. Earlier studies of isotopologues of environmental methane interpreted low-temperature, equilibrium $\Delta^{13}\text{CH}_3\text{D}$ signals as methane produced by methanogens under slow growth-rate (i.e. hydrogen limited) conditions (Stolper et al., 2015; Wang et al., 2015). However, these samples came from environments like the Santa Barbara Basin (Harrison et al., 2009) and the Gulf of Mexico (Lloyd et al., 2006) where AOM is a well-documented process that may have been underappreciated during these initial studies. Kidd Creek mine methane is similar to Bornholm Basin in that it shows methane with isotopologue distributions that transition from non-equilibrium

signals to those in thermodynamic equilibrium. In this case, the source methane in the two billion year old reservoir of water is likely abiotic methane produced through Fischer-Tropsch-type reactions that is depleted in $\Delta^{12}\text{CH}_2\text{D}_2$ due to hydrogen tunneling (Young et al., 2017) but near equilibrium in $\Delta^{13}\text{CH}_3\text{D}$. We suggest that drilling exposed this abiotic methane to anaerobic methanotrophs, because within years of exposure, Kidd Creek methane also approaches thermodynamic equilibrium (Fig 4.2). The difference in equilibration timescale between Kidd Creek and Bornholm Basin may be due to the difference in environmental parameters that govern the rates in each system.

Methane driven to equilibrium by AOM has a distinct end member composition when plotted as $\Delta^{13}\text{CH}_3\text{D}$ versus $\Delta^{12}\text{CH}_2\text{D}_2$ from methane produced through other known mechanisms (thermogenesis, microbial methanogenesis and abiotic methanogenesis) [Fig. 4.3 (Young et al., 2017)]. AOM metabolisms have been shown to be active from -1°C - 70°C (Holler et al., 2011; Niemann et al., 2006), a range of temperatures that is unique and distinguishable from equilibrated thermogenic samples (100°C - 250°C). Abiotic methane may form at low temperatures where AOM is possible, yet although it is apparently equilibrated in $\Delta^{13}\text{CH}_3\text{D}$, it exhibits large depletions in $\Delta^{12}\text{CH}_2\text{D}_2$ that distinguish it from methane that has undergone exchange catalysis during AOM. We suggest therefore that the combination of $\Delta^{12}\text{CH}_2\text{D}_2$ and $\Delta^{13}\text{CH}_3\text{D}$ values is potentially useful in the search for life throughout the solar system in general and for AOM activity in particular.

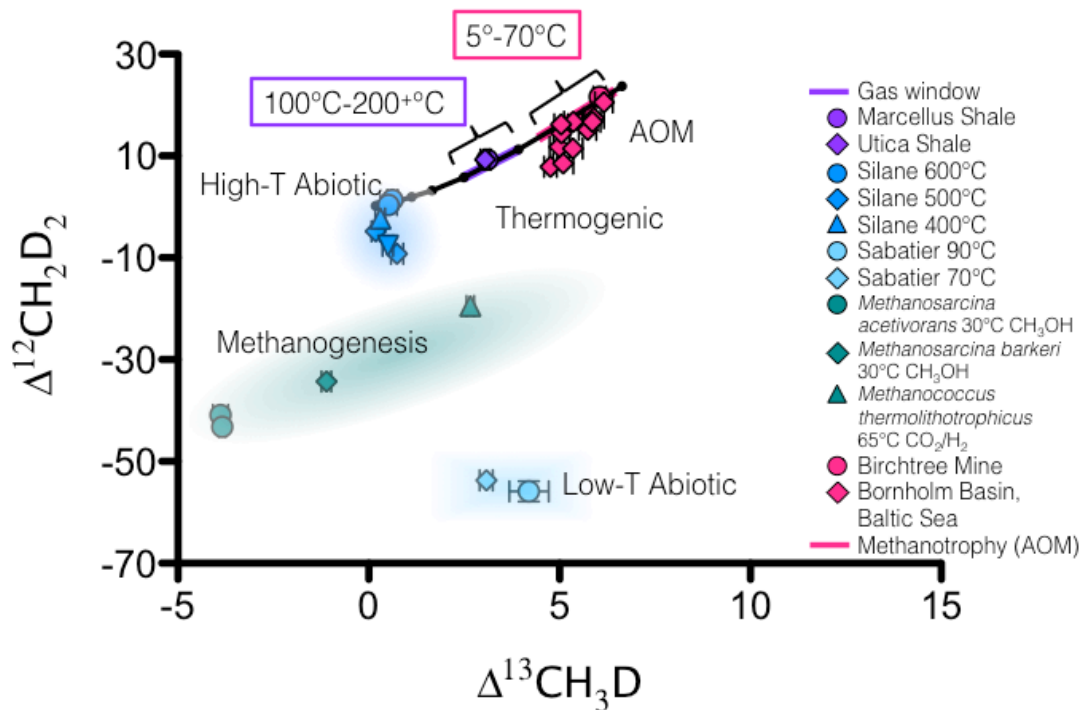


Figure 4.3: $\Delta^{12}\text{CH}_2\text{D}_2$ is plotted versus $\Delta^{13}\text{CH}_3\text{D}$. Solid black line and black dots are the same as in Figure 4.2. Methane produced by thermogenesis, high-temperature abiotic reactions, microbial methanogenesis and low-temperature abiotic reactions inhabit unique zones in double-isotopologue space (Young et al., 2017). AOM, equilibrating through exchange catalysis during enzymatic back reaction, also inhabits a unique zone: low-temperature intra-species thermodynamic equilibrium.

Materials and Methods

Stable and clumped isotope notation

Stable isotope data is reported in delta notation where delta refers to a difference in rare isotope ratio from a standard. The standards include Pee Dee Belemnite (PDB) for carbon and Standard Mean Ocean Water (SMOW) for hydrogen. For example,

$$\delta^{13}\text{C} = \left(\frac{{}^{13}\text{R}_{\text{sample}}}{{}^{13}\text{R}_{\text{standard}}} - 1 \right) \bullet 1000 , \quad (1)$$

where R refers to the ratio $^{13}\text{C}/^{12}\text{C}$ and the difference is in per mil (‰). Similarly, for D/H,

$$\delta\text{D} = \left(\frac{{}^2\text{R}_{\text{sample}}}{{}^2\text{R}_{\text{standard}}} - 1 \right) \bullet 1000 . \quad (2)$$

Abundances of rare isotopologues are reported relative to the stochastic distribution of isotopic bond pairings in which the relative abundances of rare isotopologues are those predicted by chance for a given bulk isotopic composition. For example, the fraction of carbon that is the rare isotope, ^{13}C , is

$$X(^{13}\text{C}) = \frac{{}^{13}\text{C}}{{}^{13}\text{C} + {}^{12}\text{C}} , \quad (3)$$

and the fraction of the hydrogen isotopes that is deuterium, D, is

$$X(\text{D}) = \frac{\text{D}}{\text{D} + \text{H}} . \quad (4)$$

In order to arrive at the stochastic distribution of isotopologues, the fractional abundances are equated with probabilities, yielding

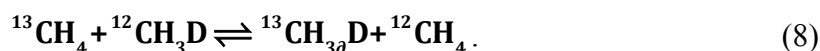
$$X(^{12}\text{CH}_4) = X(^{12}\text{C})(X(\text{H}))^4 \quad (5)$$

$$X(^{13}\text{CH}_4) = X(^{13}\text{C})(X(\text{H}))^4 \quad (6)$$

$$X(^{12}\text{CH}_3\text{D}) = 4X(^{12}\text{C})(X(\text{H}))^4(X(\text{D})) \quad (7)$$

where the coefficient “4” in Equation (7) accounts for the 4 equivalent isotopomers created by varying configurations of D within molecules. This stochastic distribution of isotopes applies for systems in thermodynamic equilibrium at high temperatures (> 1000K). At lower temperatures, thermodynamic equilibrium predicts excesses of the multiply-substituted species relative to stochastic.

As an example, consider the following intra-species isotope exchange reaction:



The equilibrium constant for this reaction is

$$K_{\text{Eq}} = \frac{[^{13}\text{CH}_3\text{D}][^{12}\text{CH}_4]}{[^{13}\text{CH}_4][^{12}\text{CH}_3\text{D}]} \quad (9)$$

where the brackets indicate concentrations by molecule. The equilibrium constant at infinite temperature is evaluated by substituting the fractional abundances from Equation (7) into Equation (9) for the concentrations such that

$$K_{\text{Eq}} = \frac{4X(^{13}\text{C})(X(\text{H}))^3 X(\text{D})X(^{12}\text{C})(X(\text{H}))^4}{4X(^{12}\text{C})(X(\text{H}))^3 X(\text{D})X(^{13}\text{C})(X(\text{H}))^4} = 1 \quad (10)$$

At lower temperatures, the equilibrium constant in Equation (10) is > 1. Values less than unity are indicative of kinetics, mixing, or some other process that shifts the abundances of isotopologues from their equilibrium values.

Per mil differences between the apparent intra-species equilibrium constant (concentration quotient) and the stochastic equilibrium constant are expressed using the capital delta notation such that

$$\Delta_{^{13}\text{CH}_3\text{D}} = 10^3 \ln \left(\frac{K_{\text{Eq}}}{K_{\text{Eq,Stochastic}}} \right) \sim 10^3 \left(\frac{X_{^{13}\text{CH}_3\text{D}}}{X_{^{13}\text{CH}_3\text{D,Stochastic}}} - 1 \right). \quad (11)$$

The equivalent expression for $^{12}\text{CH}_2\text{D}_2$ is

$$\Delta_{^{12}\text{CH}_2\text{D}_2} = 10^3 \ln \left(\frac{K_{\text{Eq}}}{K_{\text{Eq,Stochastic}}} \right) \sim 10^3 \left(\frac{X_{^{12}\text{CH}_2\text{D}_2}}{X_{^{12}\text{CH}_2\text{D}_2,\text{Stochastic}}} - 1 \right). \quad (12)$$

Sample Purification and Analysis

Gas samples were purified on a vacuum line with inline gas chromatography using methods described previously (Young et al., 2017). Mass spectrometric methods are similar to those previously described excepting the use of a small-volume cold finger during introduction to the bellows of the mass spectrometer inlet (Young et al., 2017; Young et al., 2016). In this modified method, samples are frozen onto a silica gel cold finger cooled by liquid nitrogen directly adjacent to the bellows housing for 5 minutes. The sample bellows and the cold finger are subsequently isolated from the rest of the dual inlet and warmed to room temperature. The variable volume bellows is cycled during warming to promote thorough mixing of gas. Between analyses, the cold finger is heated to 40°C and pumped at high vacuum prior to introduction of new samples.

Baltic Sea data for this study were analyzed in August of 2016 and January-March of 2017. Two tank methane gases (UCLA-1 and UCLA-2) are used as reference internal

standards. The compositions of these gases were determined by comparing to gases of known bulk isotopic compositions and to gases heated to $>800^{\circ}\text{C}$. Aliquots of $<60\ \mu\text{mol}$ of the reference gases were repeatedly analyzed during these two sessions to assess external precision during measurement of small Baltic Sea samples which were of comparable size. The average internal precision for $\delta^{13}\text{C}$, δD , $\Delta^{13}\text{CH}_3\text{D}$ and $\Delta^{12}\text{CH}_2\text{D}_2$ values are 0.004‰, 0.03‰, 0.31‰ and 0.84‰, respectively, during the August 2016 analytical session and 0.01‰, 0.03‰, 0.23‰ and 0.74‰ respectively for the January-March 2017 analytical session. External 1σ precision for $\delta^{13}\text{C}$, δD , $\Delta^{13}\text{CH}_3\text{D}$ and $\Delta^{12}\text{CH}_2\text{D}_2$ values are 0.01‰, 0.02‰, 0.14‰ and 0.14‰, respectively, for the August 2016 session and 0.02‰, 0.02‰, 0.12‰ and 0.42‰, respectively, for the January-March 2017 session as determined by replicate analyses of aliquots of reference gases comparable to the sample sizes.

Samples used in this study

Thermogenic methane

Gases previously measured from the Marcellus and Utica Shales in the Appalachian Basin of the eastern USA are used as representative thermogenic gases in this study (Young et al., 2017). The Marcellus formation consists of black, carbonaceous shale of Middle Devonian age, and the Utica formation (ranging from hundreds of meters to 2 km below the Marcellus) is an organic-rich, black calcareous shale of Middle Ordovician age. These samples originate from a well operated by Shell Oil Company in western Pennsylvania. Modern temperatures in the Marcellus and Utica Shales are 60°C and 90°C respectively (Rowan and Geological Survey (U.S.), 2006).

Methanogenesis cultures

Previously published clumped isotope data for axenic methanogen cultures are used as a reference in this study (Young et al., 2017). The cultures were grown in crimp-top serum bottles at the University of Southern California. *Methanosarcina barkeri* and *Methanosarcina acetivorans* were grown at 30°C with methanol *Methanothermococcus thermolithotrophicus* was grown at 60°C with CO₂ and H₂.

Baltic Sea

Baltic Sea methane samples analyzed here were collected in October 2013 as part of the Integrated Ocean Drilling Program Expedition 347 (Baltic Sea Paleoenvironment). Sediment cores were drilled in Bornholm Basin (55°28.034'N, 15°28.680'E). Sediment-associated methane was collected by plunging a cut-off, sterile syringe into a freshly exposed core end. Sediment samples of 5 cubic centimeters were extruded into 10 mL syringes pre-poisoned with 5mL 1M NaOH and crimp sealed under atmosphere. Samples were agitated to break up sediment and stored upside down at 4°C until analysis. Methane concentration and other key geochemical parameters were analyzed as described in detail in (Egger et al., 2017).

Abiotic methane synthesis

Methane samples produced through silane decomposition and the Sabatier reaction are representative of abiotically synthesized methane in this study. Details of these experiments are outlined in Young et al., 2017.

Kidd Creek Mine

Kidd Creek Mine extends to 3 km depth in the subsurface and the deepest waters sampled have billion-year residence times. Samples reported on herein originate from two locations with depths of 7850 and 9500 feet and were collected from 2013-2015. Temperatures range from 23°C-26°C at the 7850 site and 29°C-32°C at the 9500 site. Abiotic synthesis has been suggested to be the mechanism producing methane at a depth of 6800 feet (Lollar et al., 2002).

Modeling the timescale of equilibration

In order to assess the plausibility of equilibrating methane by methanotrophy in the Baltic Sea sediments, we determine the timescale necessary to equilibrate a hypothetical reservoir of methane with an initial clumped isotope composition identical to that produced by an axenic culture of *Methanosarcina acetivorans* grown on methanol at 30°C ($\Delta^{13}\text{CH}_3\text{D} = -3.88\text{‰}$ and $\Delta^{12}\text{CH}_2\text{D}_2 = -40.86\text{‰}$) (Young et al., 2017). We determine the rate of enzymatic back reaction during AOM from the expression

$$\mathbf{R}_{\text{-AOM}} = \mathbf{R}_{\text{net AOM}} \left(\frac{\mathbf{R}_{\cdot}}{\mathbf{R}_{+}} \right)_{\text{AOM}} \quad (13)$$

where \mathbf{R}_{AOM} is the enzymatic back reaction rate due to $\text{SO}_4\text{-AOM}$, $\mathbf{R}_{\text{net AOM}}$ is the rate of net methanotrophy and $(\mathbf{R}/\mathbf{R}_{+})_{\text{AOM}}$ is the ratio of enzymatic back reaction to net methanotrophy. For the value of $\mathbf{R}_{\text{net AOM}}$, we take the weighted average flux of the modeled rates present from 10.33 MCD to 24.24 MCD, yielding $0.84 \text{ pmols CH}_4 \text{ cm}^{-3} \text{ d}^{-1}$ (Dijkstra et al.). Values for $(\mathbf{R}/\mathbf{R}_{+})_{\text{AOM}}$ from the literature range from 0.032 to 0.78 with an average value of 0.26 (Holler et al., 2011; Orcutt et al., 2005; Seifert et al., 2006;

Treude et al., 2007; Yoshinaga et al., 2014). These inputs suggest that a reasonable estimate for R_{AOM} for Bornholm Basin is $0.22 \text{ pmols cm}^{-3} \text{ d}^{-1}$. The timescale (τ) of equilibration is determined from this rate estimate from the volumetric mixing ratio of methane:

$$\tau = \frac{[\text{CH}_4]}{R_{\text{AOM}}} \quad (14)$$

From Equation (14), the average timescale of equilibration for 5.36 mM CH_4 (i.e. the methane concentration at 21.48 MCD) is $\sim 6.7 \times 10^4$ years. For comparison, diagenetic porewater modeling suggests that the methane in equilibrium at a depth of 22 MCD should $< \sim 8 \times 10^3$ years. The difference between our estimate for equilibration time and the estimated age of the methane can be reconciled if:

- 1) $(R/R_+)_{\text{AOM}}$ for Fe-AOM in the Bornholm Basin is closer to (or greater than) the maximum measured value of 0.78 than the average value of 0.26 measured for SO_4 -AOM,

or

- 2) The model $R_{\text{net AOM}}$ rates are underestimated.

Disentangling the contributions of the two potential sources of error to the calculated timescale is not possible *a priori*. However, modeled rates (i.e. net rates) are known to underestimate the actual turnover rates based on isotopic incubation studies (i.e. gross rates). Tripling $R_{\text{net AOM}}$ and using the higher value of 0.78 for $(R/R_+)_{\text{AOM}}$ decreases the calculated timescale of equilibration to 7.4×10^3 years, near to the estimated maximum age of the methane gas.

In keeping with the implied uncertainties, we utilize a τ value of 10^4 years in the rate model used here for illustration purposes. The rate constant for enzymatic back reaction (K_{-AOM}) is obtained by treating the timescale of equilibration as an e-fold time:

$$K_{-AOM} = \frac{e}{\tau} . \quad (15)$$

We utilize this K_{-AOM} in a simple model that describes the equilibration from a disequilibrium methanogenic end member to thermodynamic equilibrium at the average temperature of 7.75°C estimated from shipboard core temperature measurements. We describe the rate of equilibration system using

$$\frac{d\Delta}{dt} = K_{-AOM} (\Delta_{Eq} - \Delta_t) , \quad (16)$$

where Δ_{Eq} is the clumped isotope composition at equilibrium and Δ_t is the clumped isotope composition at a given time step. In essence, this formulation treats the rate of reaction as one driven by the reaction affinity (e.g. (De Donder, 1927; Prigogine et al., 1954)).

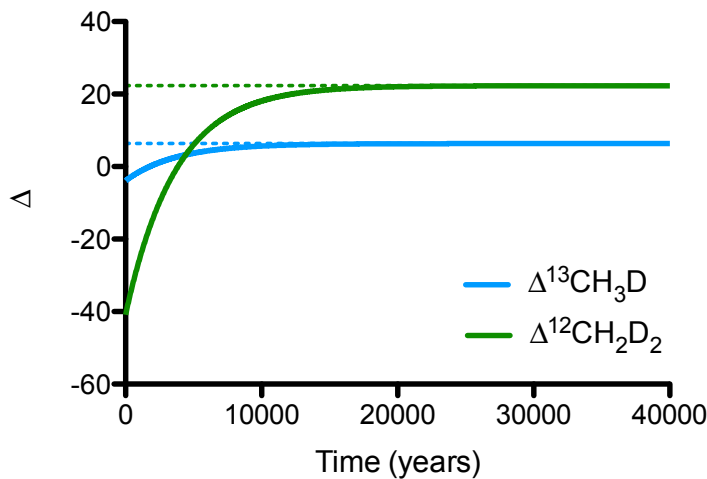


Figure S4.1: $\Delta^{13}\text{CH}_3\text{D}$ and $\Delta^{12}\text{CH}_2\text{D}_2$ equilibrate within ~ 10000 years. Equilibrium values for both species are shown as dashed lines.

The methanogenesis endmember defines $\Delta_{t=0}$, and $\Delta_{t=\infty}$ is defined by thermodynamic equilibrium at 7.75°C. The curves in Figure S4.1 illustrate the timescales of equilibration for the two mass-18 isotopologues of methane. Figure S4.2 shows the evolution of microbial methane progressively equilibrated over this timescale to the low-temperature AOM endmember in double isotopologue space under two treatments. The first assumes that K_{AOM} is equal for both the $^{13}\text{CH}_3\text{D}$ and $^{12}\text{CH}_2\text{D}_2$ isotopologues, and the trajectory is a straight line between the two endmembers. The second assumes that K_{AOM} for $^{12}\text{CH}_2\text{D}_2$ is half of that for $^{13}\text{CH}_3\text{D}$ to account for the higher energy barrier of bonding two deuteriums within a methane molecule.

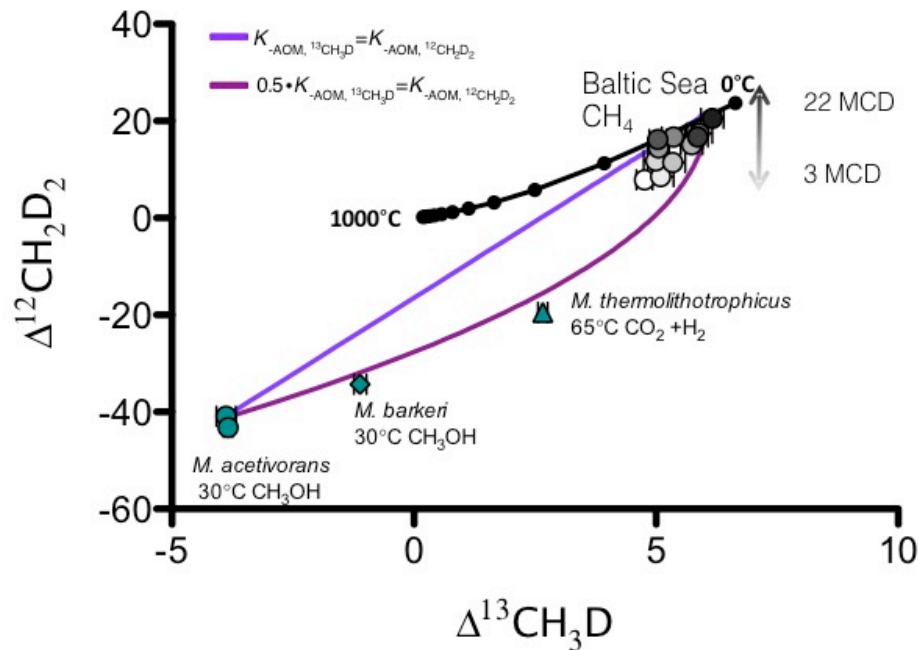


Figure S4.2: $\Delta^{12}\text{CH}_2\text{D}_2$ is plotted versus $\Delta^{13}\text{CH}_3\text{D}$. Solid black line represents theoretical thermodynamic equilibrium in 100°C increments marked by black circles. Baltic Sea methane data are shown as open circles shaded from white (shallowest sample) to black (deepest sample). Green symbols represent axenic cultures of methanogens as labeled. Purple lines represent equilibration pathways under two treatments as described in the text.

Rate measurements

Samples for prokaryotic activity measurements were taken from the center of WRCs with sterile 5 ml syringes (luer end removed) under anaerobic and aseptic handling conditions (Parkes et al., 1995) and sealed with Suba-Seals (Sigma). All syringe mini-core samples were then equilibrated under anoxic conditions (under nitrogen in sealed gas-tight aluminum bags) at 10°C for approximately 12 h prior to further processing. Microbial activity was measured by injecting the syringe mini-core samples, along the central line of the syringe, individually with ^{14}C -acetate (7.5 μl , 81.3 kBq), ^{14}C -bicarbonate (7.5 μl , 106.2 kBq), ^{14}C -dimethylamine (7.5 μl , 30.5 kBq) or ^{14}C -methane (10 μl , 21.7 kBq) for estimating acetoclastic-, hydrogenotrophic-, and methylotrophic methanogenesis, plus anaerobic oxidation of methane, respectively. The ^{14}C -methane was injected as a gas, all other isotopes were in aqueous solution. Injected samples were then incubated at 10°C under anoxic conditions for a further 3, 7 and 16 h (^{14}C -acetate, -dimethylamine, -methane) or 7, 16 and 24 h (^{14}C -bicarbonate). Ten syringe mini-cores were used at each depth for each isotope with one frozen immediately after injection as a control. Incubations were terminated by individually transferring the syringe contents into 30 ml glass vials containing 7 ml of 2 M NaOH, sealed, mixed thoroughly and stored inverted until processing. Radio-labeled methane was determined by purging the headspace (35 ml min^{-1} for 20 minutes) with a mixture of nitrogen and oxygen (95:5) as a carrier gas through a CO_2 absorber and then over copper oxide in a furnace (Carbolite, UK) at 900°C. Oxidized ^{14}C -methane to ^{14}C - CO_2 was collected in three scintillation vials placed in series containing 10 ml of scintillation fluid, with 7% (v/v) beta-phenethylamine to absorb the ^{14}C - CO_2 , and activity was measured in a scintillation counter.

Potential rates of methanogenesis for each substrate were determined by applying the label turnover rates to the pool size of total acetate, (DIONEX 2 x 50 mm guard column AG15 and 2 x 250 mm analytical column AS15 using KOH as eluent at a flow rate of 0.35 ml/min for 53 minutes with a conductivity detector and AERS-2 mm suppressor), dimethylamine (DIONEX 3 x 50 mm guard column CG16 and 3 x 250 mm analytical column CS16 using methanesulfonic acid as eluent at a flow rate of 0.36 ml/min for 80 minutes with a conductivity detector and CERS-2 mm suppressor), and CO₂ [calculated from IODP Expedition 347 pH and alkalinity data; (Andr n et al., 2015)].

Sources of error for these measurements are principally that activity measurements were made *in vitro* after a period of sample storage, during which time super-saturated concentrations of methane in the core samples would have dissipated. Additionally, incubations were carried out at 10 C under 1 atm pressure rather than *in situ* conditions. The use of ¹⁴C-methane in gas form to maximize the concentration of methane in the syringe mini-core sample likely also increases variability as there is no control over where the injected isotope moves within the syringe mini-core during incubation. Measurements such as these are referred to as potential activity rates, and values are listed in Table S4.2.

Due to these issues, we present rate measurements as δ -values where

$$\delta_{\text{AOM}} = \text{AOM}_0 - \text{AOM}_{\text{MCD}} \quad (17)$$

and

$$\delta_{\text{MG}} = \text{MG}_0 - \text{MG}_{\text{MCD}} \quad (18)$$

where **AOM** and **MG** are total anaerobic methanotrophy rates and total methanogenesis rates respectively at 3.3 MCD (**subscript 0**) and at depth (**subscript MCD**). Presenting the rates as δ -values preserves the overall trends for each process while acknowledging that the absolute values of the rate measurements themselves may be inaccurate (Fig. S4.3).

Table S4.1 Potential activity measurements

Depth (MCD)	AOM activity (nmol cm ⁻³ d ⁻¹)	Acetoclastic methanogenesis activity (pmol cm ⁻³ d ⁻¹)	Hydrogenotrophic methanogenesis activity (pmol cm ⁻³ d ⁻¹)	Methylotrophic methanogenesis activity (pmol cm ⁻³ d ⁻¹)	Total methanogenesis activity (pmol cm ⁻³ d ⁻¹)
3.88	6.7209	-	-	-	-
3.93	-	1.3098	0.325	1.3275	2.6697
13.68	9.2717	-	-	-	-
13.73	-	0.00	0.0023	1.1216	1.1240
29.53	15.8719	-	-	-	-
29.58	-	0.00	0.0054	0.0619	0.0672
35.83	0.0000	-	-	-	-
35.88	-	1.9952	0.00	0.3827	2.3779

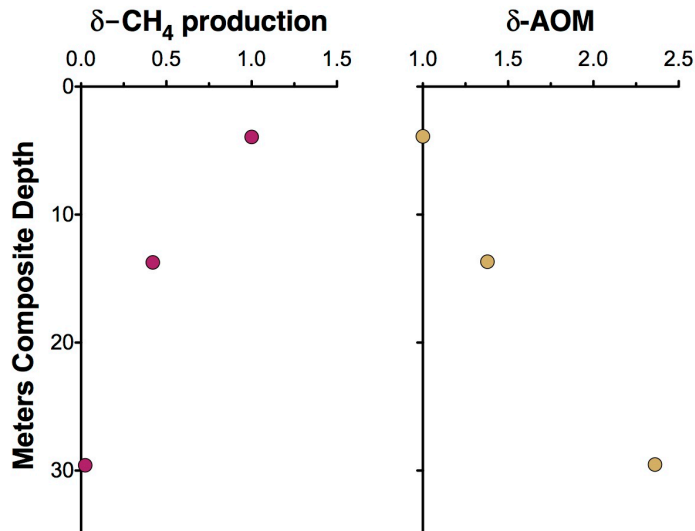


Figure S4.3: Rates of total methanogenesis (left) and AOM (right) presented as δ -values show that methanogenesis activity decreases with depth while AOM activity increases with depth.

Calculating $\xi_{^{12}\text{CH}_2\text{D}_2}$

The parameter $\xi_{^{12}\text{CH}_2\text{D}_2}$ quantifies the difference between $\Delta^{12}\text{CH}_2\text{D}_2_{\text{measured}}$ and $\Delta^{12}\text{CH}_2\text{D}_2_{\text{equilibrium}}$. $\Delta^{12}\text{CH}_2\text{D}_2_{\text{equilibrium}}$ is calculated by assuming that for each datum, $\Delta^{13}\text{CH}_3\text{D}_{\text{measured}}$ is in equilibrium and that all methane isotopologues are in intra-species thermodynamic equilibrium. A $\xi_{^{12}\text{CH}_2\text{D}_2}$ value of zero implies that $\Delta^{12}\text{CH}_2\text{D}_2_{\text{measured}}$ is in intra-species thermodynamic equilibrium with all methane isotopologues, and a positive or negative $\xi_{^{12}\text{CH}_2\text{D}_2}$ value implies that $\Delta^{12}\text{CH}_2\text{D}_2_{\text{measured}}$ is not in intra-species thermodynamic equilibrium with the corresponding $\Delta^{13}\text{CH}_3\text{D}_{\text{measured}}$. In Bornholm Basin, the shallowest samples display the most positive values of $\xi_{^{12}\text{CH}_2\text{D}_2}$, and the deepest samples approach zero (Fig. S4.4).

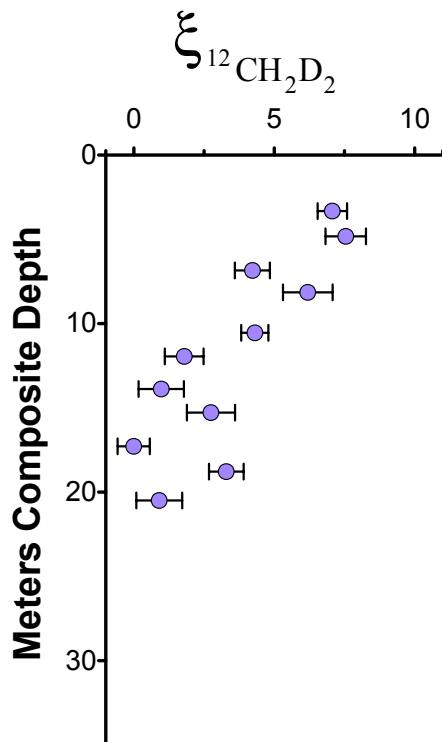


Figure S4.4: $\xi_{^{12}\text{CH}_2\text{D}_2}$ values are the greatest at shallow MCD, indicating the greatest departure from equilibrium and approach zero with increasing MCD, indicating an approach towards intra-species thermodynamic equilibrium.

Table S4.2 Species concentrations for ΔG calculations

Species	Concentration	Source
$\text{CH}_4 + \text{SO}_4^{2-} \rightarrow \text{HCO}_3^- + \text{HS}^- + \text{H}_2\text{O}_{(l)}$		
SO_4^{2-}	0.16 mM	(Andrén et al., 2015)
HS^-	0.001 mM*	(Egger et al., 2017)
HCO_3^-	4.7mM [§]	(Egger et al., 2017)
CH_4	5.36 mM	(Andrén et al., 2015)
$\text{CH}_4 + 8\text{Fe}(\text{OH})_{3(s)} + 16\text{H}^+ \rightarrow \text{CO}_2 + 8\text{Fe}^{2+} + 22\text{H}_2\text{O}_{(l)}$		
Fe^{2+}	277.2 μM	(Andrén et al., 2015)
CH_4	5.36 mM	(Andrén et al., 2015)
H^+	$10^{-7.41} \text{ M}^{\text{y}}$	(Andrén et al., 2015)
CO_2	0.293 mM [§]	(Egger et al., 2017)

*Below detection

[§]Calculated from DIC concentration^yCalculated from shipboard pH measurements**Table S4.3: Methane geochemistry of Bornholm Basin, Baltic Sea**

Meters Composite Depth	$\delta^{13}\text{C} \text{ ‰}$ $\pm 1 \text{ SD}$	$\delta\text{D} \text{ ‰}$ $\pm 1 \text{ SD}$	$\Delta^{13}\text{CH}_3\text{D}$ $\pm 1 \text{ SD}$	$\Delta^{12}\text{CH}_2\text{D}_2 \text{ ‰}$ $\pm 1 \text{ SD}$
3.32	-76.16 ± 0.003	-244.03 ± 0.023	4.76 ± 0.16	7.88 ± 0.52
4.82	-74.06 ± 0.006	-242.45 ± 0.024	5.10 ± 0.27	8.52 ± 0.72
6.85	-72.54 ± 0.005	-239.91 ± 0.024	4.10 ± 0.25	11.76 ± 0.63
8.15	-71.81 ± 0.005	-238.60 ± 0.034	5.35 ± 0.26	11.42 ± 0.89
10.55	-71.87 ± 0.005	-239.34 ± 0.020	5.73 ± 0.23	15.13 ± 0.49
11.95	-72.11 ± 0.006	-239.95 ± 0.029	5.05 ± 0.22	14.48 ± 0.69
13.88	-72.33 ± 0.005	-239.21 ± 0.032	5.36 ± 0.24	16.70 ± 0.81
15.28	-72.89 ± 0.005	-238.92 ± 0.033	5.90 ± 0.26	17.43 ± 0.86
17.28	-74.03 ± 0.004	-238.37 ± 0.025	5.04 ± 0.18	16.21 ± 0.57
18.78	-74.63 ± 0.006	-238.28 ± 0.030	5.86 ± 0.21	16.72 ± 0.62
20.50	-75.59 ± 0.005	-238.20 ± 0.038	6.17 ± 0.23	20.54 ± 0.82

References

Andr n, T., Jorgensen, B., Cotterill, C., Green, S., Andr n, E., Ash, J., Bauersachs, T., Cragg, B., Fanget, A. and Fehr, A. (2015) Expedition 347 Summary, Proceedings of the Integrated Ocean Drilling Program, pp. 1-66.

Beal, E.J., House, C.H. and Orphan, V.J. (2009) Manganese- and iron-dependent marine methane oxidation. *Science* 325, 184-187.

Boetius, A., Ravensschlag, K., Schubert, C.J., Rickert, D., Widdel, F., Gieseke, A., Amann, R., J rgensen, B.B., Witte, U. and Pfannkuche, O. (2000) A marine microbial consortium apparently mediating anaerobic oxidation of methane. *Nature* 407, 623-626.

De Donder, T. (1927) *L'affinit *.

Dijkstra, N., Hagens, M., Egger, M. and Slomp, C.P. (2017) Post-depositional vivianite formation alters sediment phosphorus records. *Biogeosciences Discussions* in review.

Douglas, P., Stolper, D., Smith, D., Anthony, K.W., Paull, C., Dallimore, S., Wik, M., Crill, P.M., Winterdahl, M. and Eiler, J. (2016) Diverse origins of Arctic and Subarctic methane point source emissions identified with multiply-substituted isotopologues. *Geochim Cosmochim Acta* 188, 163-188.

Edwards, K.J., Becker, K. and Colwell, F. (2012) The deep, dark energy biosphere: intraterrestrial life on earth. *Annual Review of Earth and Planetary Sciences* 40, 551-568.

Egger, M., Hagens, M., Sapart, C.J., Dijkstra, N., van Helmond, N.A., Mogoll n, J.M., Risgaard-Petersen, N., van der Veen, C., Kasten, S. and Riedinger, N. (2017) Iron oxide reduction in methane-rich deep Baltic Sea sediments. *Geochim Cosmochim Acta* 207, 256-276.

Etioppe, G. and Sherwood Lollar, B. (2013) Abiotic Methane on Earth. *Reviews of Geophysics* 51, 276-299.

G rtner, P., Weiss, D.S., Harms, U. and Thauer, R.K. (1994) N⁵ - Methyltetrahydromethanopterin: Coenzyme M Methyltransferase from *Methanobacterium thermoautotrophicum*. *The FEBS Journal* 226, 465-472.

Harrison, B.K., Zhang, H., Berelson, W. and Orphan, V.J. (2009) Variations in archaeal and bacterial diversity associated with the sulfate-methane transition zone in continental margin sediments (Santa Barbara Basin, California). *Appl Environ Microb* 75, 1487-1499.

Holler, T., Wegener, G., Niemann, H., Deusner, C., Ferdelman, T.G., Boetius, A., Brunner, B. and Widdel, F. (2011) Carbon and sulfur back flux during anaerobic microbial oxidation of methane and coupled sulfate reduction. *Proceedings of the National Academy of Sciences* 108, E1484-E1490.

Inagaki, F., Hinrichs, K.-U., Kubo, Y., Bowles, M.W., Heuer, V.B., Hong, W.-L., Hoshino, T., Ijiri, A., Imachi, H. and Ito, M. (2015) Exploring deep microbial life in coal-bearing sediment down to ~ 2.5 km below the ocean floor. *Science* 349, 420-424.

Knittel, K. and Boetius, A. (2009) Anaerobic oxidation of methane: progress with an unknown process. *Annual review of microbiology* 63, 311-334.

Krüger, M., Meyerdierks, A., Glöckner, F.O., Amann, R., Widdel, F., Kube, M., Reinhardt, R., Kahnt, J., Böcher, R. and Thauer, R.K. (2003) A conspicuous nickel protein in microbial mats that oxidize methane anaerobically. *Nature* 426, 878-881.

Lloyd, K.G., Alperin, M.J. and Teske, A. (2011) Environmental evidence for net methane production and oxidation in putative ANaerobic MEthanotrophic (ANME) archaea. *Environmental microbiology* 13, 2548-2564.

Lloyd, K.G., Lapham, L. and Teske, A. (2006) An anaerobic methane-oxidizing community of ANME-1b archaea in hypersaline Gulf of Mexico sediments. *Appl Environ Microb* 72, 7218-7230.

Lollar, B.S., Westgate, T., Ward, J., Slater, G. and Lacrampe-Couloume, G. (2002) Abiogenic formation of alkanes in the Earth's crust as a minor source for global hydrocarbon reservoirs. *Nature* 416, 522-524.

Marshall, I.P., Karst, S.M., Nielsen, P.H. and Jørgensen, B.B. (2017) Metagenomes from deep Baltic Sea sediments reveal how past and present environmental conditions determine microbial community composition. *Marine genomics*.

Martini, A.M., Budai, J.M., Walter, L.M. and Schoell, M. (1996) Microbial generation of economic accumulations of methane within a shallow organic-rich shale. *Nature* 383, 155-158.

McCollom, T.M. and Seewald, J.S. (2006) Carbon isotope composition of organic compounds produced by abiotic synthesis under hydrothermal conditions. *Earth and Planetary Science Letters* 243, 74-84.

McCollom, T.M. and Seewald, J.S. (2007) Abiotic synthesis of organic compounds in deep-sea hydrothermal environments. *Chem Rev* 107, 382-401.

Milucka, J., Ferdelman, T.G., Polerecky, L., Franzke, D., Wegener, G., Schmid, M., Lieberwirth, I., Wagner, M., Widdel, F. and Kuypers, M.M. (2012) Zero-valent sulphur is a key intermediate in marine methane oxidation. *Nature* 491, 541-546.

Moran, J.J., House, C.H., Freeman, K.H. and Ferry, J.G. (2005) Trace methane oxidation studied in several Euryarchaeota under diverse conditions. *Archaea* 1, 303-309.

Niemann, H., Lösekann, T., De Beer, D., Elvert, M., Nadalig, T., Knittel, K., Amann, R., Sauter, E.J., Schlüter, M. and Klages, M. (2006) Novel microbial communities of the Haakon Mosby mud volcano and their role as a methane sink. *Nature* 443, 854-858.

Orcutt, B., Boetius, A., Elvert, M., Samarkin, V. and Joye, S. (2005) Molecular biogeochemistry of sulfate reduction, methanogenesis and the anaerobic oxidation of methane at Gulf of Mexico cold seeps. *Geochim. Cosmochim. Acta* 69, 5633-5633.

Parkes, R.J., Cragg, B.A., Bale, S., Goodman, K. and Fry, J.C. (1995) A combined ecological and physiological approach to studying sulphate reduction within deep marine sediment layers. *Journal of Microbiological Methods* 23, 235-249.

Pine, M.J. and Barker, H. (1956) STUDIES ON THE METHANE FERMENTATION XII.: The Pathway of Hydrogen in the Acetate Fermentation¹. *Journal of bacteriology* 71, 644.

Pohlman, J., Kaneko, M., Heuer, V., Coffin, R. and Whiticar, M. (2009) Methane sources and production in the northern Cascadia margin gas hydrate system. *Earth and Planetary Science Letters* 287, 504-512.

Prigogine, I., Defay, R. and Everett, D. (1954) *Chemical thermodynamics*. Longmans, Green London.

Rowan, E.L. and Geological Survey (U.S.) (2006) Burial and thermal history of the central Appalachian Basin, based on three 2-D models of Ohio, Pennsylvania, and West Virginia, U S Geological Survey open-file report 2006-1019. U.S. Dept. of the Interior, U.S. Geological Survey,, Reston, Va., p. 35 p.

Scheller, S., Goenrich, M., Boecher, R., Thauer, R.K. and Jaun, B. (2010) The key nickel enzyme of methanogenesis catalyses the anaerobic oxidation of methane. *Nature* 465, 606.

Scheller, S., Yu, H., Chadwick, G.L., McGlynn, S.E. and Orphan, V.J. (2016) Artificial electron acceptors decouple archaeal methane oxidation from sulfate reduction. *Science* 351, 703-707.

Seifert, R., Nauhaus, K., Blumenberg, M., Krüger, M. and Michaelis, W. (2006) Methane dynamics in a microbial community of the Black Sea traced by stable carbon isotopes in vitro. *Organic Geochemistry* 37, 1411-1419.

Sivan, O., Adler, M., Pearson, A., Gelman, F., Bar-Or, I., John, S.G. and Eckert, W. (2011) Geochemical evidence for iron - mediated anaerobic oxidation of methane. *Limnol Oceanogr* 56, 1536-1544.

Stolper, D.A., Lawson, M., Davis, C.L., Ferreira, A.A., Neto, E.V.S., Ellis, G.S., Lewan, M.D., Martini, A.M., Tang, Y., Schoell, M., Sessions, A.L. and Eiler, J.M. (2014a) Formation temperatures of thermogenic and biogenic methane. *Science* 344, 1500-1503.

Stolper, D.A., Martini, A.M., Clog, M., Douglas, P.M., Shusta, S.S., Valentine, D.L., Sessions, A.L. and Eiler, J.M. (2015) Distinguishing and understanding thermogenic and biogenic sources of methane using multiply substituted isotopologues. *Geochim Cosmochim Acta* 161, 219-247.

- Stolper, D.A., Sessions, A.L., Ferreira, A.A., Neto, E.V.S., Schimmelmann, A., Shusta, S.S., Valentine, D.L. and Eiler, J.M. (2014b) Combined ^{13}C -D and D-D clumping in methane: Methods and preliminary results. *Geochim Cosmochim Acta* 126, 169-191.
- Timmers, P.H., Welte, C.U., Koehorst, J.J., Plugge, C.M., Jetten, M.S. and Stams, A.J. (2017) Reverse Methanogenesis and respiration in methanotrophic archaea. *Archaea* 2017.
- Treude, T., Orphan, V., Knittel, K., Gieseke, A., House, C.H. and Boetius, A. (2007) Consumption of methane and CO₂ by methanotrophic microbial mats from gas seeps of the anoxic Black Sea. *Appl Environ Microb* 73, 2271-2283.
- Valentine, D.L., Chidthaisong, A., Rice, A., Reeburgh, W.S. and Tyler, S.C. (2004) Carbon and hydrogen isotope fractionation by moderately thermophilic methanogens. *Geochim Cosmochim Acta* 68, 1571-1590.
- Waite, J.H., Glein, C.R., Perryman, R.S., Teolis, B.D., Magee, B.A., Miller, G., Grimes, J., Perry, M.E., Miller, K.E. and Bouquet, A. (2017) Cassini finds molecular hydrogen in the Enceladus plume: Evidence for hydrothermal processes. *Science* 356, 155-159.
- Waldron, S., Lansdown, J., Scott, E., Fallick, A. and Hall, A. (1999) The global influence of the hydrogen isotope composition of water on that of bacteriogenic methane from shallow freshwater environments. *Geochim Cosmochim Acta* 63, 2237-2245.
- Wang, D.T., Gruen, D.S., Lollar, B.S., Hinrichs, K.-U., Stewart, L.C., Holden, J.F., Hristov, A.N., Pohlman, J.W., Morrill, P.L. and Könneke, M. (2015) Nonequilibrium clumped isotope signals in microbial methane. *Science* 348, 428-431.
- Webster, C.R., Mahaffy, P.R., Atreya, S.K., Flesch, G.J., Mischna, M.A., Meslin, P.-Y., Farley, K.A., Conrad, P.G., Christensen, L.E. and Pavlov, A.A. (2015) Mars methane detection and variability at Gale crater. *Science* 347, 415-417.
- Whiticar, M.J. (1990) A geochemical perspective of natural gas and atmospheric methane. *Organic Geochemistry* 16, 531-547.
- Whiticar, M.J. (1999) Carbon and hydrogen isotope systematics of bacterial formation and oxidation of methane. *Chem Geol* 161, 291-314.
- Yoshinaga, M.Y., Holler, T., Goldhammer, T., Wegener, G., Pohlman, J.W., Brunner, B., Kuypers, M.M.M., Hinrichs, K.U. and Elvert, M. (2014) Carbon isotope equilibration during sulphate-limited anaerobic oxidation of methane. *Nat Geosci* 7, 190-194.
- Young, E., Kohl, I., Lollar, B.S., Etiope, G., Rumble, D., Li, S., Haghnegahdar, M., Schauble, E., McCain, K. and Foustoukos, D. (2017) The relative abundances of resolved $^{12}\text{CH}_2\text{D}_2$ and $^{13}\text{CH}_3\text{D}$ and mechanisms controlling isotopic bond ordering in abiotic and biotic methane gases. *Geochim Cosmochim Acta* 203, 235-264.

Young, E.D., Rumble, D., Freedman, P. and Mills, M. (2016) A large-radius high-mass-resolution multiple-collector isotope ratio mass spectrometer for analysis of rare isotopologues of O₂, N₂, CH₄ and other gases. *International Journal of Mass Spectrometry* 401, 1-10.

Appendix 1: Measurements of Landsort Deep Methane $^{13}\text{CH}_3\text{D}$ and $^{12}\text{CH}_2\text{D}_2$

Sediment cores were drilled in Landsort Deep, Baltic Sea ($58^\circ37.34'\text{N}$, $18^\circ15.25'\text{E}$) during the International Ocean Drilling Program Expedition 347. Methane was collected shipboard, purified and analyzed for stable and clumped isotope analysis following identical methods to those outlined in Chapter 4. Here, the results of these measurements are presented (Figure A1, Table A1).

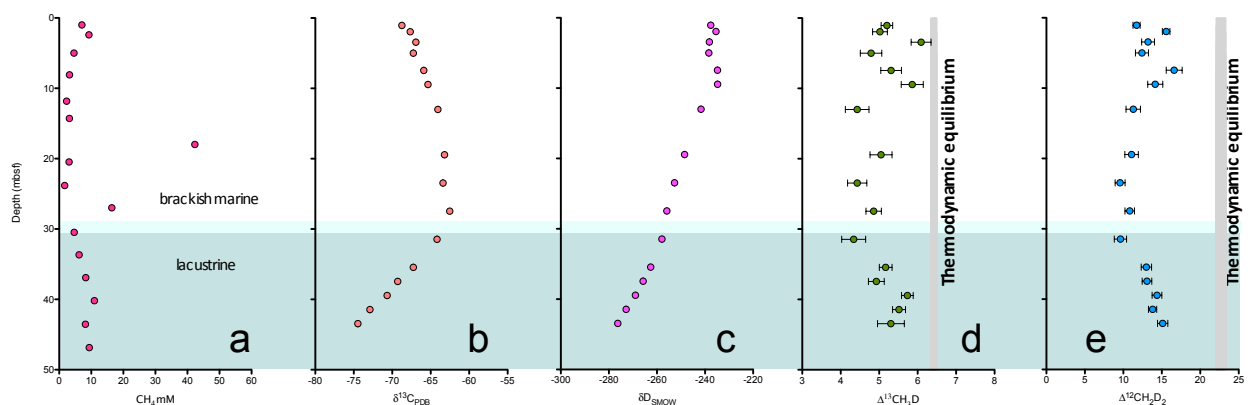


Figure A1: Methane geochemistry is shown varying with adjusted meters below seafloor (AMBSF). Brackish marine sediments overlay lacustrine sediments (noted by blue bar). Panel **a** shows shipboard measurements of CH_4 concentration in mM; the jagged nature of this profile is due to sediment degassing upon core retrieval (Andrén et al., 2015). Panels **b** and **c** are $\delta^{13}\text{C}$ and δD respectively. Error bars for these measurements are smaller than the symbols. Panels **d** and **e** are $\Delta^{13}\text{CH}_3\text{D}$ and $\Delta^{12}\text{CH}_2\text{D}_2$ respectively with the grey bars denoting the predicted equilibrium composition of $\Delta^{13}\text{CH}_3\text{D}$ and $\Delta^{12}\text{CH}_2\text{D}_2$ for average core temperature of $5.6 \pm 0.3^\circ\text{C}$.

Analysis of Landsort Deep methane ranged from 1.1 to 43.5 adjusted meters below seafloor (AMBSF). Average core temperature was $5.6 \pm 0.3^\circ\text{C}$. $\delta^{13}\text{C}$ increases downcore from -68.739‰ to -62.52‰ to an inflection point at 27.5 AMBSF. Values then decrease

to a minimum of -74.468‰. δD values vary secularly between -234.794‰ and 238.42‰ within the top 9.5 mcd, then decrease downcore to a minimum of -276.304‰. Trends in Landsort Deep $\Delta^{13}\text{CH}_3\text{D}$ and $\Delta^{12}\text{CH}_2\text{D}_2$ are similar to one another in that they vary from 4.8‰ to 6.1‰ and 11.7‰ to 16.6‰ respectively in the upper 7.5 AMBSF, then decrease to minimum values of 4.3‰ and 9.6‰ respectively at 31.5 AMBSF. $\Delta^{13}\text{CH}_3\text{D}$ and $\Delta^{12}\text{CH}_2\text{D}_2$ from 35.5 to 43.5 AMBSF increase to average values of 5.3‰ and 14.1‰ respectively.

Table A1: Methane geochemistry of Landsort Deep, Baltic Sea

Depth AMBSF	CH ₄ mM	Depth AMBSF	$\delta^{13}\text{C}$ ‰ ± 1 SD	δD ‰ ± 1 SD	$\Delta^{13}\text{CH}_3\text{D}$ ± 1 SD	$\Delta^{12}\text{CH}_2\text{D}_2$ ‰ ± 1 SD
0.99	7.09	1.05	-68.74 ± 0.004	-237.61 ± 0.019	5.20 ± 0.151	11.723 ± 0.468
2.40	9.29	1.95	-67.66 ± 0.004	-235.42 ± 0.019	5.02 ± 0.191	15.571 ± 0.498
4.99	4.61	3.44	-66.93 ± 0.006	-238.19 ± 0.037	6.09 ± 0.259	13.221 ± 0.834
8.08	3.20	5.00	-67.26 ± 0.007	-238.42 ± 0.035	4.79 ± 0.278	12.421 ± 0.843
11.83	2.33	7.45	-65.90 ± 0.021	-234.84 ± 0.068	5.31 ± 0.267	16.610 ± 1.029
14.28	3.19	9.45	-65.35 ± 0.023	-234.79 ± 0.071	5.86 ± 0.287	14.151 ± 0.982
17.98	42.32	13.00	-64.06 ± 0.009	-241.65 ± 0.045	4.43 ± 0.306	11.294 ± 0.939
20.47	3.08	19.44	-63.20 ± 0.007	-248.52 ± 0.041	5.05 ± 0.286	11.071 ± 0.876
23.82	1.70	23.45	-63.40 ± 0.021	-252.69 ± 0.028	4.43 ± 0.249	9.583 ± 0.646
26.98	16.43	27.45	-62.52 ± 0.006	-255.90 ± 0.029	4.86 ± 0.200	10.837 ± 0.618
30.47	4.67	31.45	-64.18 ± 0.013	-257.92 ± 0.036	4.34 ± 0.312	9.626 ± 0.797
33.67	6.23	35.45	-67.26 ± 0.008	-262.61 ± 0.029	5.17 ± 0.165	12.997 ± 0.671
36.91	8.29	37.45	-69.28 ± 0.007	-265.77 ± 0.036	4.93 ± 0.206	13.071 ± 0.624
40.18	10.99	39.45	-70.66 ± 0.006	-268.94 ± 0.032	5.73 ± 0.152	14.376 ± 0.630
43.53	8.19	41.45	-72.90 ± 0.011	-272.82 ± 0.031	5.52 ± 0.168	13.811 ± 0.534
46.85	9.40	43.45	-74.47 ± 0.026	-276.30 ± 0.036	5.31 ± 0.349	15.116 ± 0.671

References

Andrén, T., Jorgensen, B., Cotterill, C., Green, S., Andrén, E., Ash, J., Bauersachs, T., Cragg, B., Fanget, A. and Fehr, A. (2015) Expedition 347 Summary, Proceedings of the Integrated Ocean Drilling Program, pp. 1-66.